UNIVERSITY OF SOUTHAMPTON

Faculty of Engineering and Physical Sciences
School of Physics and Astronomy

Multi-Wavelength Studies of Accretion and Outflows in Compact Binaries

DOI: XXXXXXXX

Volume n of m

by

Noel Castro Segura

MSc in Astrophysics

ORCiD: 0000-0002-5870-0443

A thesis for the degree of
Doctor of Philosophy

June 2022

University of Southampton

Abstract

Faculty of Engineering and Physical Sciences
School of Physics and Astronomy

Doctor of Philosophy

Multi-Wavelength Studies of Accretion and Outflows in Compact Binaries

by Noel Castro Segura

The study of interacting compact binaries invokes a wide variety of astrophysical concepts, ranging from the physics of compact objects, accretion, stellar atmospheres and interiors, stellar and binary evolution. These systems host a stellar remnant, i.e. a white dwarf, neutron star or black hole – which produce a wide variety of exotic phenomena observable across the entire electromagnetic spectrum. Essentially all accreting systems exhibit evidence of mass-loss in the form of jets and disc winds, representing key mechanisms by which they interact with their environment.

In this thesis, multi-wavelength (MW) observations encompassing different techniques and a wide range of timescales are used to investigate the accretion flow, outflows and evolution of two accreting compact binaries. In Chapter 2, the first comprehensive study on *V341 Ara* is presented, a 10^{th} magnitude star recently identified as a cataclysmic variable star. The analysis of long-term and high resolution light curves allows the identification of both, the negative super-humps, and the super-orbital modulation of a tilted accretion disc that ultimately causes them. A recently developed disc instability model acting in a tilted disc is proposed as the underlying mechanism responsible of the eventual fading episodes observed in this source. The system's mass ratio is obtained from time-resolved spectroscopy and the wind mass loss rate is constrained using spatially resolved [OIII] emission produced by a bow-shock.

In Chapter 3, an overview of a major MW campaign is presented. One of the key ingredients of this campaign is the coordination of many of the major Earth- and space-based observatories from X-ray to radio, including near-infrared optical and ultraviolet time resolved spectroscopy and photometry of an extremely flaring low-mass X-ray binary. Chapter 4 is focused on the detection and implications of accretion disc winds in the ultraviolet spectrum we obtained during the campaign. In this research time-tagged far-ultraviolet spectroscopy is used to demonstrate that the absorption troughs are associated with a non-variable component of the spectrum, showing that flares and outflows are driven by different mechanisms; it also illustrates how wind signatures can be masked by flaring emission, even if the outflow is present all the time. This is crucial for the correct interpretation of all wind signatures. In Chapter 5, archival and new data is analysed to determine the properties of the companion star and line-of-sight absorption, to discuss the intrinsic luminosity and evolutionary stage of *Swift J1858*. All this is summarised in Chapter 6 along with future lines of research in these topics.

Contents

List of Figures

List of Tables

Declaration of Authorship

I, Noel Castro Segura, declare that this thesis entitled *Multi-Wavelength Studies of Accretion and Outflows in Compact Binaries*. and the work presented in it is my own and has been generated by me as the result of my own original research.

I confirm that:

- This work was done wholly or mainly while in candidature for a research degree at this University;
- Where any part of this thesis has previously been submitted for a degree or any other qualification at this University or any other institution, this has been clearly stated;
- Where I have consulted the published work of others, this is always clearly attributed;
- Where I have quoted from the work of others, the source is always given. With the exception of such quotations, this thesis is entirely my own work;
- I have acknowledged all main sources of help;
- Where the thesis is based on work done by myself jointly with others, I have made clear exactly what was done by others and what I have contributed myself;
- Most of the work presented in Chapter 2 has been published as:
  - Castro Segura, N.; Knigge, C.; Acosta-Pulido, J. A.; et al. *Bow shocks, nova shells, disc winds and tilted discs: the nova-like V341 Ara has it all*, 2021 **MNRAS**, 501, 195C.
- Most of the work presented in Chapter 4 has been published as:
  - Castro Segura, N.; Knigge, C.; Long, K. S.; et al. *A persistent ultraviolet outflow from an accreting neutron star transient*, 2022 **Nature**, 603, 7899, p.52-57.
- A publication based on Chapter 5 is in preparation.

Signed:..... Date:.....

Acknowledgements

The last years have been a fantastic period in my life. I have grown, both as a person and astronomer, I travelled around the world and meet amazing people that helped me to walk through this unique and very personal experience that took me to where I stand now.

I would like to thank most of the people that were involved during my PhD. Starting from the people that served as inspiration and helped me during my time in Tenerife, the ones that helped me to have a soft landing when I first moved to Southampton. All the friends I made in Southampton which make the winter less cold. The very friendly vibe from in the astro department that makes it a comfortable place to work. To all my office mates during these years. Thank to everyone, including Fran, Georgios, Regis, Miika, Viky, Tomás, Angelis, Kevin, Jakub, Ale, Peter, Mayukh, Triana, Federico, Claudia, Matt...

I would like to acknowledge all the academic friends who always supported and gave feedback on my research. Thanks to José, Pablo, Knox, Tony, Diego, Simone, Nathalie, Matthew, Omer and Jorge for your support.

Special thanks to Juan, Tom, James, Federico, Jakob, Phil, Santiago, Rob, Jorge, Teo, David and everyone who got on board and helped with the crazy multi-wavelength campaign. It was a really satisfactory and amazing experience that could not happen without the support of all of you.

To my supervisor Christian Knigge for his unconditional support and patience. For the countless insightful conversations that helped me to understand every aspect of my research and gain an edge in science. For his contagious enthusiasm and motivation, thank you.

To my family. Your support has been crucial during this stage of my life. To Loreto and Javier who became my family during this time. For sharing all the joys and struggles during these last years, thanks for being there.

Definitions and Abbreviations

AGN	Active galactic nuclei
AMI-LA	Arcminute Microkelvin Imager – Large Array
AML	Angular momentum loss
ASAS-SN	All-Sky Automated Survey for Supernovae
AWD	Accreting white dwarf
BH	Black hole
BL	Boundary layer
COS	Cosmic Origins Spectrograph
CTIO	Cerro Tololo Interamerican Observatory
CV	Cataclysmic variable
DN	Dwarf nova
FUV	Far-ultraviolet
GTC	Gran Telescopio de Canarias
GWR	Gravitational wave radiation
HST	Hubble Space Telescope
ISM	Interstellar medium
KELT	Kilo-degree Extremely Little Telescope
LDI	Line-driven instabiilty
LIGO	Laser Interferometer Gravitational-Wave Observatory
LMXB	Low-mass X-ray binary
LT	Liverpool Telescope
LTE	Local thermodynamic equilibrium
MAST	Mikulski Archive for Space Telescopes
MCMC	Markov Chain Monte-Carlo
MRI	Magnetorotational instability
NICER	Neutron Star Interior Composition Explorer
NIR	Near infrared
NL	Nova-like
NS	Neutron star
NuSTAR	Nuclear Spectro-scopic Telescope Array
NUV	Near-ultraviolet
PN	Planetary nebula

QPO	Quasi periodic oscilations
QSO	Quasar
RGS	Reflection Grating Spectrometer
SED	Spectral energy distribution
SPOC	Science Processing Operations Center
STIS	Space Telescope Imaging Spectrograph
TED	Tidal disruption event
TESS	Transiting Exoplanet Survey Satellite
TTSMT	Thermal-time-scale mass transfer
UFO	Ultra-fast outflow
UV	Ultraviolet
VLA	Very Large Array
VLT	Very Large Telescope
WD	white dwarf
XRB	X-ray binaries

Chapter 1

Introduction

Accretion is the process by which objects in the universe grow in mass. It shapes many of the astronomical objects we observe, ranging from galaxies down to the formation of planetary systems around young stars. Taking place at all scales in the universe, it plays a fundamental role in many areas of astrophysics, from star formation to galaxy evolution.

The gravitational energy that is released as matter falls into a central object is usually released as radiation. This makes accretion the most efficient mechanism for extracting radiative energy from matter, surpassing by far thermonuclear reactions. To illustrate this, we can get an order-of-magnitude estimate by considering a body of radius R with mass M. The gravitational potential energy released by the accretion of a particle with mass m from infinity onto its surface is

$$\Delta E_{acc} = GMm/R, \tag{1.1}$$

where G is the gravitational constant. On the other hand, hydrogen being the most abundant element in the universe, we can consider the "burning" process of hydrogen into helium via nuclear fusion . Here, the energy release would be

$$\Delta E_{nuc} = 0.007mc^2, \tag{1.2}$$

where c is the speed of light.

It is worth noting here that, while the energy released in the nuclear fusion only depends on the burned mass, the energy released by accretion is proportional to the ratio of mass to radius of the object, $\Delta E_{acc} \propto M/R$. Hence, for a typical compact object, such as a neutron star with 1 $M_\odot$ and 10 km radius, the total energy released by 1 gram of matter by the time it reach the surface of the object is 20 times greater than transforming that same amount of matter into energy via fusion, $\Delta E_{acc}/\Delta E_{nuc} \sim 20$ (Frank et al., 2002).

We can also use equation 1.1 to estimate the luminosity generated by steady accretion, i.e. the accretion of mass onto an object at some fixed *rate*. Taking the time derivative of equation 1.1, we obtain

$$L_{acc} = \dot{E}_{acc} = \frac{GM\dot{m}}{R} \tag{1.3}$$

where the dot represent the derivative with respect to time. Thus $\dot{m}$ represents the mass accretion rate.

In most astrophysical settings, the accreting material carries too much angular momentum to fall directly onto the central object. This leads to the formation of *accretion discs*, in which material slowly spirals inwards as a result of viscous processes that transport angular momentum outwards and dissipate gravitational potential energy (which is then released as radiation). Accretion discs are thought to be the central engines in a wide range of important astrophysical settings, including AGNs, young stellar objects, tidal disruption events (TDEs) and accreting compact binaries.

Accretion being a natural process driven by gravity suggests that, broadly speaking, the physics governing this process should be similar regardless of the mass and nature of the accretor. This idea has been supported by several findings over the past decade, establishing the universality of accretion discs. Examples of common phenomenology include the broken-power law shape of the power spectrum associated with accretion-induced variability (McHardy et al., 2006; Scaringi et al., 2015), the rms-flux relationship (Uttley & McHardy, 2001), quasi periodic oscillations (QPOs, e.g. Belloni et al., 2002; Alston et al., 2014), as well as the presence of conspicuous outflows.

Essentially all disc-accreting systems exhibit evidence of mass loss. These outflows come in two different flavours: disc winds and jets. Collimated radio jets are often seen emerging from the centres of active galaxies (Hazard et al., 1963; Ledden et al., 1976; Raiteri et al., 2017), X-ray binaries (Spencer, 1979; Mirabel & Rodríguez, 1999; Miller-Jones et al., 2019), more recently radio emission from jets is also detected in CVs (Körding et al., 2008; Coppejans & Knigge, 2020; Hewitt et al., 2020, and references therein). Accretion disc winds, on the other hand, can extract significant amounts of mass from the disc in the form of much less collimated, bipolar outflows.

The primary signature of these disc winds are blue-shifted absorption and *P-Cygni* profiles associated with certain spectral lines. These features are observed, for example, in the ultraviolet resonance lines of CVs in a high state (Heap et al., 1978; Cordova & Mason, 1982; Prinja et al., 2000) and in $\simeq$ 10% - 20% of QSOs (e.g. Knigge et al., 2008b). In some cases they are also seen in the optical spectra of CVs (Patterson et al., 1996; Kafka & Honeycutt, 2004) and X-ray binary stars (XRBs Muñoz-Darias et al., 2016, although the primary feature are blue-shifted absorption in the X-ray region). In the latter systems, disc winds appear to be able to remove matter from the disc faster than it can be supplied and transported inwards (Casares et al., 2019), which suggests that these outflows might be able to disrupt episodes of enhanced accretion (Muñoz-Darias

et al., 2016). More generally, disc winds represent a key mechanism by which accreting systems interact with their environments.

Accreting compact binaries play an important role in our understanding of accretion discs and related outflows. Essentially, they represent the some of the best available laboratories for studying accretion physics. This is particularly true for eclipsing systems, which can be used to resolve accretion discs spatially (e.g. Horne, 1985; Wood et al., 1986, but also see Marsh & Horne (1988)). These objects will be the subject of study in this thesis. In this chapter, I will provide an overview of our current knowledge of accreting binaries and their outflows to lay the groundwork for the studies presented in the following chapters.

1.1 Interacting Binary Stars

The majority of the stars in our Galaxy are part of double or multiple systems (Duquennoy & Mayor, 1991; El-Badry et al., 2018, 2021). The actual fraction varies from $\simeq$ 60% for solar Solar-type stars up to $\simeq$ 80% for the most massive stars (Raghavan et al., 2010; Fuhrmann et al., 2017). Around 40% of these systems have an orbital period ($P_{\rm orb}$) short enough to cause mass transfer between two of their components at some point in their evolution (González Martínez-País et al., 2014). A high fraction of the interacting population contains a compact stellar remnant. Interacting binaries are associated with some of the most exotic astronomical objects known, such as contact systems (e.g. Eta Carinae Damineli, 1996) and blue stragglers (Sandage, 1953; Leonard, 1989; Knigge et al., 2008a) among others. A good understanding of the behaviour and evolution of these binaries is essential to our understanding of fundamental physics, fluid dynamics, stellar and galaxy evolution.

The phenomenology observed in binary stars varies greatly. As is common in astronomy, the initial classification of these objects was based on their observational properties, with classes typically named after their proto-type. As a first approach this method is useful, since it clusters objects exhibiting similar behaviour. This can facilitate the search for the origin of their shared phenomenology. However, purely observational taxonomy can also quickly lead to a plethora of confusing categories that are not mutually exclusive. It is therefore useful to (also) use a more physical approach to classify these objects, e.g. by their accretion geometry, donor star and nature of the compact object. I will mainly follow the latter approach in this thesis.

As can be seen from equation 1.3, the compactness of the accretor (M/R) is a critical factor in determining the accretion luminosity. Hence, a natural way to classify accreting compact binaries is by the different classes of stellar remnants. In order of increasing mass and density of the compact object, these are white dwarfs (WDs), neutron stars (NSs) and black holes (BHs). However, interacting binaries containing both NS and BH

accretors are commonly referred to as X-ray binaries (XRBs), since both types of accretors are compact enough for the accretion luminosity to emerge primarily as X-rays.

The abundance of different types of stellar remnants is anti-correlated with their mass. This is a direct consequence of the initial mass function (IMF) of the stars in the galaxy (Kroupa, 2001). In short, the production of denser remnants requires a higher progenitor mass, and the probability of stars being born with a given mass decreases with mass. As a result, interacting WD binaries are the most common type of accreting systems in the Galaxy.

The donor star also plays an important role in determining the characteristics of a given system. Usually, the donor is a main-sequence star, but it can also be a compact object itself, allowing for interacting binaries with extremely short orbital periods and small binary separations. For example, *AM CVn* stars(named after their proto-type) are accreting WD binaries in which the donor is another degenerate object (typically a He WD) or a semi-degenerate object (e.g. He star Marsh et al., 2004). The orbital periods of AM CVns range from $\simeq$5 min to $\simeq$65 min. If the accretor is a NS or BH instead, such systems are referred to as ultra-compact XRBs (Homer et al., 2002).

The nature of the donor star also plays an important role in determining the accretion geometry. For example, if the donor drives a strong stellar wind, the compact object can accrete just by intercepting part of this outflow. This is the case in most *symbiotic stars* (Sokoloski, 2003; Mikołajewska, 2007), where the donor is a red giant and the accretor is (usually) a WD. Wind accretion also powers some XRBs, but here the mass-losing donor is usually a massive ($M \gtrsim 10 M_{\odot}$) O/B star. Such systems are known as wind-fed high-mass X-ray binaries (HMXRBs).

However, the most common configuration is when the donor is a low-mass, Roche-lobe-filling, main-sequence star ($M \lesssim 1 M_{\odot}$; also see Section. 1.1.1). XRBs in this configuration are called low-mass X-ray Binaries (LMXRBs), while accreting WDs with such donors are called *cataclysmic variables* (CVs). In most cases, this geometry leads to the formation of an accretion disc. However, whether this happens depends on whether the accretor has a *dynamically important* magnetic field. Magnetic forces become dynamically important if they approach or exceed the ram pressure of the accreting material. In this regime, magnetic torques can gain control of the accretion dynamics and channel plasma along the field lines towards the magnetic poles of the central object. If the field is strong enough, it may even prevent the formation of a disc entirely. For slightly weaker, but still dynamically relevant fields, the inner disc will be truncated at the magnetospheric radius. This roughly at the point where the ram pressure equals the magnetic pressure.

In spherical symmetry and assuming a dipolar magnetic field, simple theory predicts the ram pressure ($P_{ram} = \rho v^2$) to be balanced by the magnetic field pressure ($P_m = B^2/8\pi$) of the ionised material at the so-called Afvén radius r_A,

$$r_A = \left(\frac{\mu^4}{2GM\dot{m}^2} \right)^{1/7}, \tag{1.4}$$

where μ is the magnetic dipole moment ($\mu = BR^3$), G is the gravitational constant, $\dot{m}$ is the accretion rate and M, R, and B are the star mass, radius and dipolar magnetic field, respectively (Pringle & Rees, 1972; Frank et al., 2002). In the presence of an accretion disc, the dependence on the parameters remains the same, but the magnetospheric radius is $r_m = \xi r_A$, where the normalization (fudge) factor $\xi \sim 0.1 - 1$; typically $\xi \sim 0.5$ is a good approximation, e.g. Ghosh & Lamb (1979); Wang (1987); Kluźniak & Rappaport (2007).

As noted above, a dynamically important magnetic field can either truncate an accretion disc at the magnetospheric radius or prevent disc formation entirely. The parameter separating these regimes is the ratio of the magnetospheric radius to the circularisation radius of the disc, r_{circ} (see Section 1.4.1). Disc formation is prevented if $r_m \gtrsim r_{circ}$. In accreting WD systems – i.e. CVs – these two regimes are associated with distinct sub-classes. In the so-called *polars*, the magnetic field is so strong that an accretion disc cannot be formed. The accretion flow is entirely controlled by magnetic forces, which synchronize the orbital period with the spin period of the primary. By contrast, the *intermediate polars (IPs)* represent the case where a disc *can* form, but is truncated by the magnetosphere of the central star. One key observational characteristic of IPs is the presence of *two* periods in their light curves, since we typically detect modulations on both the orbital and WD spin periods. Many IPs also display variability on the beat period between these two signals.

Magnetic fields can play an important role in CVs and the formation of accretion discs in general, but it is relatively rare for WDs to possess fields strong enough to be dynamically relevant. Thus only ∼30% of CVs are polars or IPs (Pala et al., 2020). In the rest of this thesis, I will focus primarily on Roche-lobe-filling systems, in which the accretion disc surrounding the compact object extends all the way down to its surface.

1.1.1 Roche Geometry

While the gravitational potential of a single body is nearly spherical, in any semi-detached binary system, the two components are in a rotating frame of reference under the presence of centrifugal forces. These forces modify the gravitational field, resulting in an effective potential that can be approximated by the so-called *Roche potential* (Kopal, 1978). This is obtained by considering the force on a test-particle under the influence of two stars, approximated as point sources, with masses M_1 and M_2 at positions $\vec{r}_1$ and $\vec{r}_2$. The Roche potential, Φ_R, then has the form

$$\Phi_R = -\frac{GM_1}{|\vec{r}-\vec{r}_1|} - \frac{GM_2}{|\vec{r}-\vec{r}_2|} - \frac{1}{2}(\vec{\omega}\times\vec{r})^2, \tag{1.5}$$

where $\vec{\omega}$ is the angular velocity of the binary and is a vector normal to the orbital plane related to the orbital period as $|\vec{\omega}| = \Omega_{\rm orb} = 2\pi/P_{\rm orb}$.

The cross-section of the Roche potential in the mid-plane ($z = 0$) is shown in Figure 1.1. The equipotential surfaces are nearly spherical close to each of the two bodies, since here the gravitational potential is dominated by just one point source. However, as we move farther away from the centre of each star, the influence of the binary becomes more relevant, and the equipotential surfaces acquire a more ellipsoidal shape.

The contact point of the equipotential surfaces of the two stars is called the inner Lagrangian point (L_1); it is one of the 5 critical points where $\nabla\Phi_R = 0$, i.e. the net force acting on the test particle is zero. Thus, at L_1 the gravitational pulls from the two stars cancel each other. The equipotential surfaces that includes this point are called the *Roche lobes*. Therefore, if a particle dominated by the influence of one of the stars crosses this point of unstable equilibrium (L_1), it will be gravitationally bound to the other component of the system.

A complementary relation in the context of compact binaries is Kepler's third law, since it relates implicit parameters from (1.5) such as the orbital period, $P_{\rm orb}$, with the binary separation, a, and the mass of the system

$$\frac{P_{\rm orb}^2}{a^3} = \frac{4\pi^2}{GM}, \tag{1.6}$$

where $M = M_1 + M_2$ is the total mass of the system.

1.1.2 Mass transfer via Roche lobe overflow (RLOF)

In an isolated, non-rotating star in hydrostatic equilibrium, the inward gravitational forces are balanced by outward radiation pressure. Both of these forces are pure radial, so the star is always spherical. However, if the radius of a star in a binary system comes close to its Roche lobe, its surface must trace the non-spherical equipotential surfaces. In the limit that the star actually fills its Roche lobe, matter will stream through the inner Lagrangian point (see Figure 1.2), giving rise to mass transfer between the two systems. This mechanism for mass-transfer is referred to as Roche-lobe overflow (RLOF) and is responsible for driving the accretion process in CVs and LMXBs. Binaries in which one component fills its Roche lobe are also called *semi-detached* systems.

The shape of the Roche lobe is fully determined by the mass ratio of the system, $q = M_2/M_1$, where M_2 is the mass of the secondary (the donor). The 3-dimensional geometry of the Roche lobe resembles a tear-drop, but it is often useful to approximate it

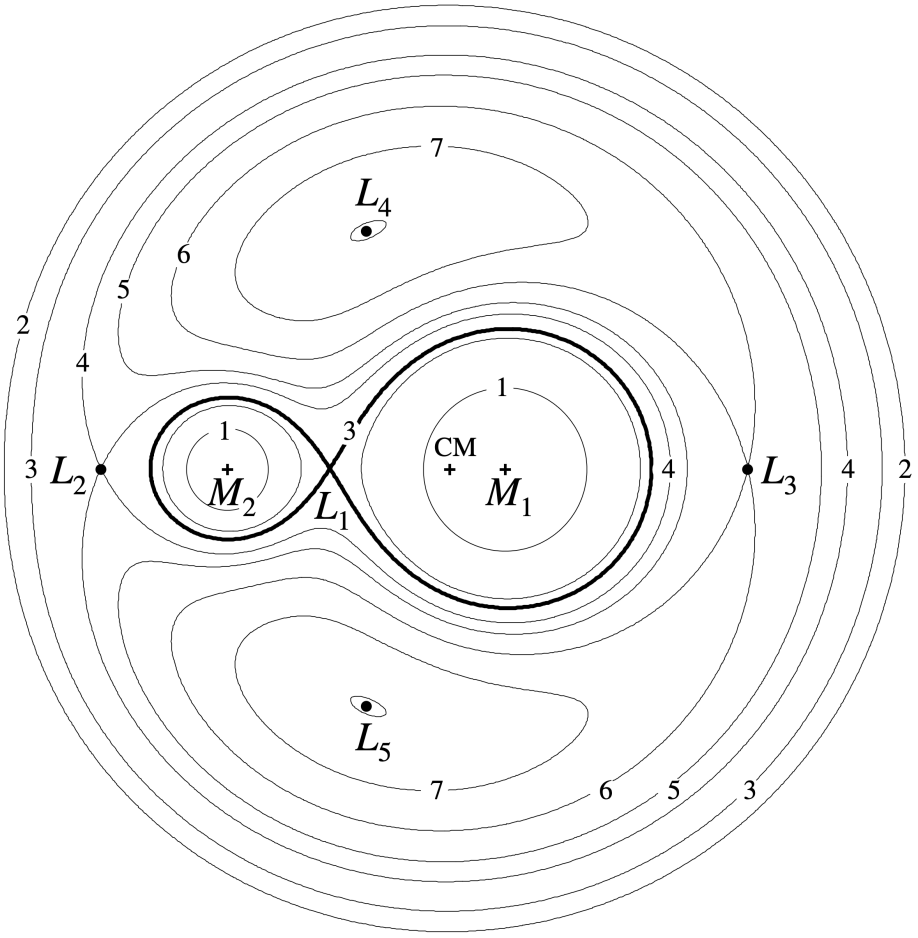

FIGURE 1.1: Mid plane cross-section of the Roche equipotential surfaces of a binary star with $q = M_2/M_1 = 0.25$. The centre of mass of the system is labelled as CM along with the centre of mass of each component (M_1 and M_2) are marked with crosses. Roche lobes (black thick line) touch each other in the inner Lagrange point (L_1), remaining equilibrium points ($L_{2,..,5}$) are indicated with circles. Credit: Frank et al. (2002).

by a sphere with the same volume. A good analytical approximation for this volume-averaged radius of the secondary is given by Eggleton (1983)

$$\frac{R_L}{a} = \frac{0.49\, q^{2/3}}{0.6\, q^{2/3} + \ln\left(1 + q^{1/3}\right)}, \tag{1.7}$$

which is accurate to better than 1%. However, it is often convenient to consider a simpler analytical fit to the numerical solution for $0.1 \lesssim q \lesssim 0.8$, given by Paczyński (1971):

$$\frac{R_L}{a} = 0.462 \left(\frac{q}{1+q}\right)^{1/3}. \tag{1.8}$$

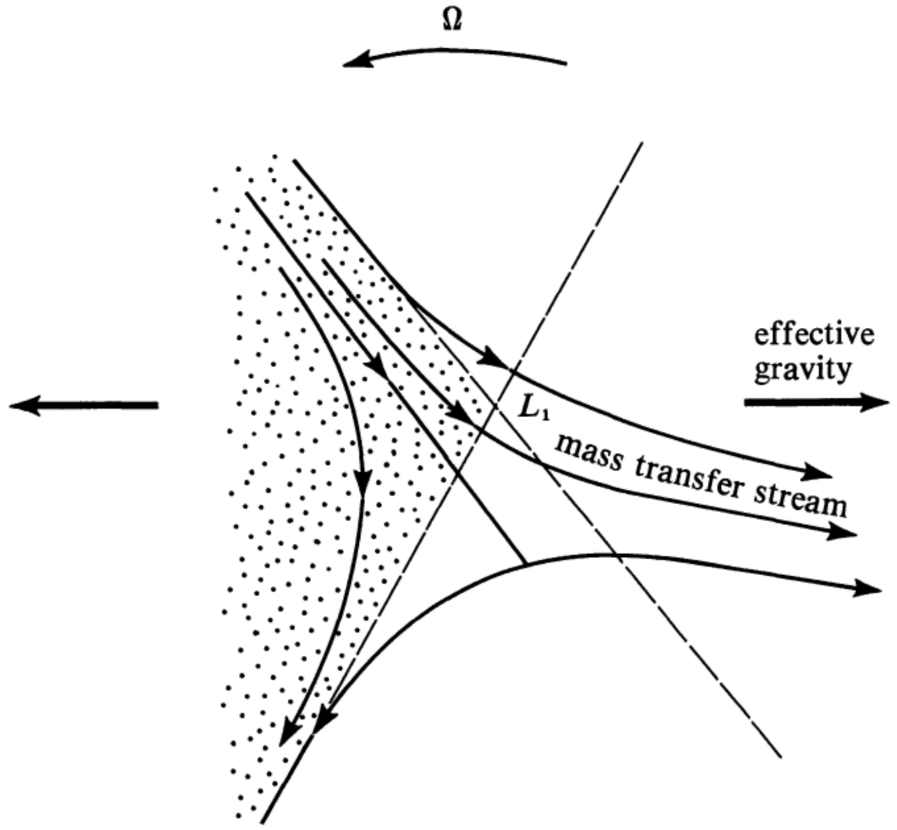

FIGURE 1.2: Illustration of Roche lobe overflow. The binary rotates with angular velocity Ω. Roche lobes (dashed lines) make contact in the inner Lagrange point (L_1), gravitational force caused by each component is indicated with thick arrows. When one of the stars gets in touch with its Roche lobe the gravitational pull is counterbalanced and the photosphere continues expanding due to the radiation pressure. The mass transferred through L_1 is now attracted by the gravitational potential of the other component, giving rise to the mass transfer stream. Credit: Shu (1982).

In terms of its volume-averaged radius, the average density of a Roche-lobe filling donor star, $\langle\rho_2\rangle$, is then simply

$$\langle\rho_2\rangle = \frac{M_2}{\frac{4}{3}\pi R_L^3}. \tag{1.9}$$

Equations 1.7 and 1.8 show that, regardless of the mechanism that brings the secondary into contact with the inner Lagrange point, the size of the Roche lobe depends only on the mass ratio, q, and the orbital separation, a. An interesting implication of this is that the mean density of a Roche-filling star is fully determined by the binary period. For a system with mass ratio $q \lesssim 0.8$, by combining eq. (1.8) with Kepler's law (eq. 1.6), we can recast the average density of the companion (eq. 1.9) as

$$\langle\rho_2\rangle \simeq 110 P_{\rm orb,hr}^{-2}\ {\rm g\ cm^{-3}}, \tag{1.10}$$

where $P_{\rm orb,hr}$ is the orbital period in hours.

Equation 1.10 can be used to infer important information about Roche-lobe filling systems, purely based on their orbital period and basic assumptions about their structure. For example, for a low-mass main-sequence stars ($M \lesssim 1 M_\odot$) we can adopt $M_2/M_\odot \simeq R_2/R_\odot$, which is a reasonable approximation to the mass-radius relationship for such stars. Combining this with Equation 1.10, we obtain the *period-mass* relation $M_2/M_\odot \simeq 0.1 P_{\rm orb,hr}$ (e.g. Knigge et al., 2011). This relation shows that low-mass main sequence stars have the densities required to fill their Roche-lobes in binary systems with orbital periods $\lesssim 10$ hrs. Roche-lobe filling donors in systems with orbital periods longer than suggested by the period-mass relation must be at least somewhat evolved in order to fill their Roche lobes.

1.1.2.1 Semi-detached binary evolution

In the previous section, we obtained the mass-period relation under the assumption that the structure of the secondary is that of a main-sequence star. While, this is an insightful exercise to gain intuition, in interacting binaries, the mass transferred from the donor can drive it out of thermal equilibrium (Knigge et al., 2011). In addition to this, the mass-transfer process redistributes angular momentum in the system and changes its mass ratio. These changes, in turn, will alter the binary separation and thus the orbital period. In order for mass transfer to be stable, the donor star has to remain in contact with the Roche lobe during these changes (Frank et al., 2002).

To see how this works, we start by considering the angular momentum of the system, J,

$$J = M_1 M_2 \left(\frac{Ga}{M}\right)^{1/2}, \tag{1.11}$$

Logarithmic differentiation of this equation with respect to time yields a key relationship governing the evolution of a system subject to mass transfer:

$$\frac{\dot{a}}{a} = \frac{2\dot{J}}{J} - \frac{2\dot{M}_1}{M_1} - \frac{2\dot{M}_2}{M2} + \frac{\dot{M}}{M}. \tag{1.12}$$

As we will discuss in 1.6.2, essentially all accreting systems display evidences of mass loss, these can be in form of disc winds, jets or thermonuclear runaway explosions. However, as a first approximation, let us assume that mass-transfer is *conservative*, i.e. that all the mass lost by the donor is accreted by the compact object. In this case $\dot{M} = \dot{M}_1 + \dot{M}_2 = 0$ and Equation (1.12) becomes (King, 1988):

$$\frac{\dot{a}}{a} = \frac{2\dot{J}}{J} - \frac{2\dot{M}_2}{M_2}(1-q), \tag{1.13}$$

where I have also replaced $M_1 = M_2/q$. If the total angular momentum is also conserved, i.e. the mass-transfer process is fully conservative, $\dot{J} = 0$, and Equation 1.13 becomes

$$\frac{\dot{a}}{a} = \frac{2\dot{M}_2}{M_2}(1-q). \tag{1.14}$$

Since $\dot{M}_2 < 0$ by definition, we can now distinguish two well defined cases. In the first case, mass is transferred from the less massive to the more massive component ($q < 1$), the accumulation of mass closer to the centre of mass will force an expansion of the orbit in order to conserve angular momentum, i.e. $\dot{a} > 0$. In the opposite case, $q > 1$, the binary separation will shrink as mass transfer moves matter away from the centre of mass.

As we have seen, the size of the Roche lobe depends only on q and a, so, in a semi-detached system, we can connect the evolution of the binary parameters to the evolution of the Roche lobe radius. Differentiating (1.8) logarithmically and substituting in from Equation 1.13 yields

$$\frac{\dot{R}_L}{R_L} = \frac{2\dot{J}}{J} - \frac{2\dot{M}_2}{M2}\left(\frac{5}{6} - q\right). \tag{1.15}$$

Here again, two different cases can be clearly identified (Ritter, 1976):

- For systems with $\mathbf{q > 5/6}$, the size of the Roche lobe will shrink in response to mass transfer from the secondary to the primary ($\dot{M}_2 < 0$), even if angular momentum is conserved ($\dot{J} = 0$). This will accelerate the mass-transfer, so this situation is unstable. Systems in this state may be expected to undergo a violent episode of rapid RLOF until the system reaches a mass ratio $q \lesssim 5/6$. This can be prevented, however, if the secondary is able to contract sufficiently rapidly in response to mass loss.
- In systems with $\mathbf{q \lesssim 5/6}$, the secondary might be expected to lose contact with its Roche lobe entirely, so accretion would be halted. However, two scenarios can prevent this loss of contact, (i) the secondary may expand due to nuclear evolution or, (ii) angular momentum loses may take place in the system, i.e. $\dot{J} < 0$ (Section 1.1.3).

As already alluded to above, an important factor in the stability of mass transfer is the response of the secondary to the mass loss. This depends largely on the time-scale(s) on which the donor is able to respond to the mass loss it experiences. The time scale on which it loses mass is simply (Knigge et al., 2011),

$$\tau_{\dot{M}_2} = \frac{M_2}{\dot{M}_2}. \tag{1.16}$$

In CVs and LMXBs, M_2 is typically about $0.1M_\odot - 0.5M_\odot$ and mass accretion rate between $10^{-9}M_\odot$ yr^{-1} to $10^{-10}M_\odot$ yr^{-1}, so the mass transfer timescale is of the order of $\sim 10^{10}$yr. This is much longer than the dynamical time scale of the secondary, so the donor always remains in hydrostatic equilibrium. However, in order for the donor to remain in *thermal* equilibrium, $\tau_{\dot{M}_2}$ needs to be longer than the thermal time scale, $\tau_{kh} \sim GM_2^2/L_2R_2$. If the mass-loss timescale is much longer than its thermal timescale, $\tau_{\dot{M}_2} >> \tau_{kh}$, the secondary will have time to readjust its radius to the new mass configuration and essentially remain a normal main sequence star. On the other hand, when the mass loss is faster than the thermal timescale, $\tau_{\dot{M}_2} << \tau_{kh}$, the donor will be driven out of the thermal equilibrium since it won't have enough time to adjust to the new configuration. Its radius response then depends on its structure. The low-mass donors in CVs and LMXBs have significant convective envelopes, and such stars respond to fast ("adiabatic") mass loss by expanding. This thermally unstable regime can therefore drive rapid mass transfer on the thermal time-scale, and can, for example, give rise to a common envelope phase (e.g. Paczynski, 1976).

In practice, it turns out that "normal" CVs and LMXBs are in the intermediate regime, where the two time scales are comparable to each other, i.e. $\tau_{\dot{M}_2} \simeq \tau_{kh}$. This means that their donors are almost, but not quite, in thermal equilibrium.

1.1.3 Angular momentum loss mechanisms

As we saw in the previous section (Sec. 1.1.2.1), angular momentum losses (AML) are necessary in order to sustain stable mass transfer in systems with mass ratios $q < 5/6$. This is clear from Eq. 1.15, where $\dot{J} < 0$ is required to avoid the donor losing contact with its Roche lobe. Here, I am going to provide a brief overview of the two AML mechanisms that are thought to play a crucial role in compact binary evolution: magnetic braking and gravitational radiation. Note, however, that additional AML mechanisms such as magnetically driven winds (Section 1.6.2.1), have also been proposed over the years in order to explain discrepancies between theory and observations (Schreiber et al., 2016).

1.1.3.1 Magnetic braking

Magnetic braking is an AML mechanisms that is associated with a stellar wind from the donor star. If the wind is ionized, and the star has a dynamically important magnetic field, wind material will initially be funneled along the magnetic field. Since the

magnetic field co-rotates with the star, the particles in the wind carry away angular momentum from the star (Kraft, 1967; Iben, 1991). In semi-detached binaries, tidal forces sustain the synchronisation of the donor spin and the orbital period of the system. The magnetic torque exerted by the wind therefore ultimately removes angular momentum from the binary system.

Even though the nature of the mechanism that generates the magnetic field is uncertain (Wright & Drake, 2016), it is thought to arise from a dynamo effect in the region between the radiative core and the convective envelope of the star (the tachocline, e.g. Parker, 1955). When a low-mass companion reaches masses around $M_2 \simeq 0.2 - 0.3 M_\odot$ it becomes fully convective. The loss of the tachocline then triggers a change in the topology of magnetic field, causing field lines to close near the stellar surface. Dynamo action may still be possible (Patterson, 1998), but it will likely switch to a turbulent configuration. This causes a significant drop in the strength of the magnetic field and consequently in the magnetic braking efficiency. In the secular evolution of CVs, this mechanism is thought to trigger the gap observed in the period distribution of such systems (Knigge et al., 2011). Magnetic braking remains rather poorly understood, so binary evolution calculations tend to rely in empirically-motivated prescriptions (e.g. Verbunt & Zwaan, 1981; Rappaport et al., 1983).

1.1.3.2 Gravitational radiation

Albert Einstein predicted the existence of gravitational waves in 1916, based on his theory of general relativity. The existence of these space-time perturbations has recently been confirmed by the Laser Interferometer Gravitational-Wave Observatory (LIGO) and Virgo experiments, via the detection of neutron star (e.g. Abbott et al., 2017) and black hole mergers (e.g. Abbott et al., 2016). Fundamentally, gravitational waves are produced by masses undergoing acceleration and can carry away energy, linear momentum and angular momentum from such systems.

In binaries, gravitational waves carry away angular momentum from the system at a rate given by (GWR, Landau & Lifshitz, ????),

$$\dot{J}_{GWR} = -\frac{32}{5}\frac{G^{7/2}}{c^5}\frac{M_1^2 M_2^2 M^{1/2}}{a^{7/2}}. \tag{1.17}$$

Even though this AML mechanism is present throughout the full evolution of binary systems, it is only efficient at small orbital separations.

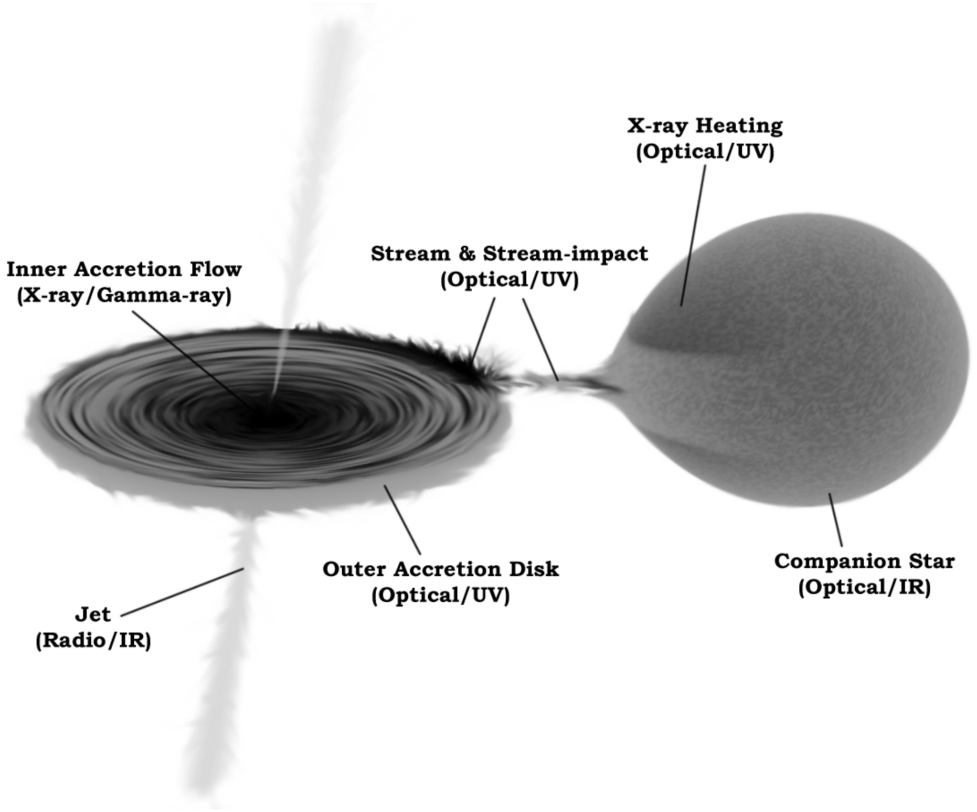

FIGURE 1.3: Geometry of a Roche lobe overflow low-mass X-ray binary. The colour scale is inverted with the brightest areas appearing darkest. Credit: Hynes (2010).

1.1.4 System components

Most semi-detached binaries share a common geometry that gives rise to similar observational characteristics. Several components contribute to the total light of a semi-detached binary, each with its own characteristic spectral energy distribution (SED), including emission lines and/or absorption lines. The typical configuration for a LMXRB is shown in Figure 1.3; in CVs, the configuration still valid, however, given the smaller mass of the accretor the process is significantly less energetic. In eclipsing systems, in particular, it is sometimes possible to isolate the signatures of the different components. A good example of this is the light-curve (LC) analysis performed by Wood et al. (1986) of the eclipsing CV *Z Cha*, shown in Figure 1.4.

1.1.4.1 Accretor

The nature of the stellar remnant is the main factor in setting the inner radius of the accretion disc and hence its luminosity. As discussed in section 1.1, the initial mass function, which describes the initial distribution of masses for a population of stars, favours the formation of low-mass stars, i.e. $M \lesssim 1 M_{\odot}$ (e.g. Chabrier, 2003). This

implies that close binaries with a WD as the primary star dominate the compact binary population we observe.

Accreting WDs in CVs are heated by the energy released by the infalling material (Sion, 1995; Townsley & Bildsten, 2004), making them relatively hot objects compared with isolated systems ($T_{eff} \geq 10\,000$ K Sion, 1999). Their SEDs thus peak in the ultraviolet (UV) region. Their spectrum is characterised by pressure broadened hydrogen absorption lines polluted by sharp absorption lines associated with metals accreted from its donor's atmosphere.

Their relative "simplicity", spatial density, proximity and variety make CVs the perfect laboratories for studying poorly understood aspects of accretion physics (Pala et al., 2020). Accreting white dwarfs (AWDs) are also of great astrophysical interest for other reasons, e.g. as prime examples of systems having evolved through the poorly understood common envelope phase (Ivanova et al., 2013) and as likely progenitors of Type Ia supernovae (Wang & Han, 2012).

The typical radius of a WD is about the size of Earth ($\simeq 10^9$ cm). On the other hand, black holes and neutron stars in LMXBs have typical radii of $\simeq 10$ km, making them much more difficult to observe directly. They therefore allow us to probe physics under extreme conditions that cannot be reproduced in Earth such as the high densities found in neutron star atmospheres (Wijnands et al., 2017) and the strong relativistic effects near the event horizons of black holes.

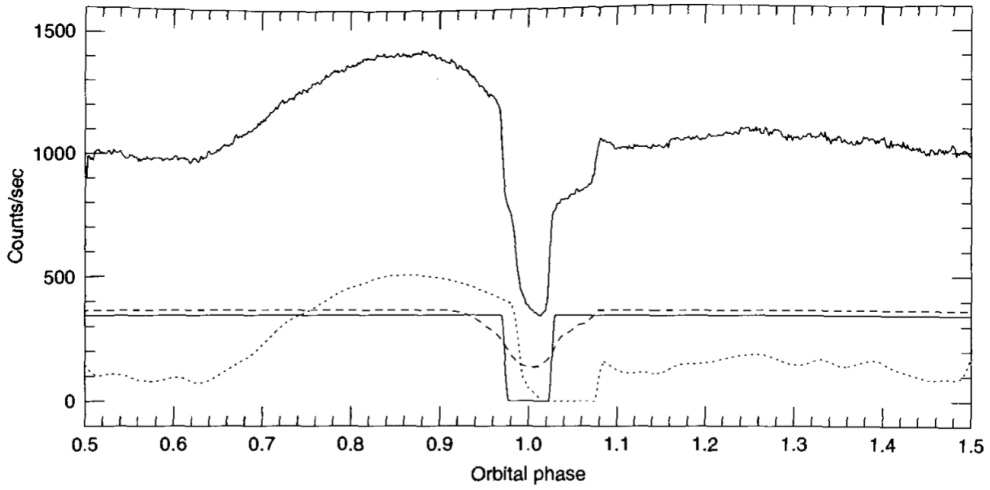

FIGURE 1.4: Light-curve of the eclipsing CV *Z Cha* with a decomposition of the spectral components in the light-curve namely, accretion disc (dashed line), bright spot (dotted) and white dwarf (solid line). Adapted from Hellier (2001), original analysis by Wood et al. (1986).

1.1.4.2 Donor star

The secondary stars in CVs and LMXBs are cool objects by comparison to the other components of these systems. Their SEDs peak in the NIR ($T_{eff} \lesssim 3\,000$ K, e.g. Knigge et al., 2011) and sometimes display molecular lines. The distorted tear-drop shape of Roche-lobe-filling donors produces so-called ellipsoidal modulations that are strongest in high-inclination systems. As they lose mass, they evolve down the main sequence, and possibly up to and beyond the point where hydrogen burning stops (Hernández Santisteban et al., 2016).

In most systems, and especially during outbursts (Section 1.4.5.1), the donor SED is easily outshone by the accretion discs (see below). In this situation, the X-ray irradiation of its atmosphere by the hotter components of the system often produces narrow emission lines (section 1.2.4, Casares et al., 2006).

1.1.4.3 Accretion disc

As a consequence of the angular momentum it carries, the accreting material tends to organise in the form of a thin disc. Here, gas is slowly being transported inward, while viscous forces dissipate the gravitational potential energy and transport the angular momentum outwards. Optically thick and geometrically thin accretion discs release energy roughly as a continuous series of blackbodies whose temperatures increase with decreasing distance from the accreting object. Each annulus within the disc thus emits at its specific characteristic temperature. The accretion disc therefore tends to produce a broad SED, with significant emission from optical wavelength up to the far-ultraviolet and even X-rays band (depending, mainly, on the compactness and mass of the accretor). Since accretion discs and their radiation are central to this thesis, they are discussed in more detail in Section 1.4.

1.1.4.4 Bright spot

Material flowing through the inner Lagrangian point initially follows a ballistic trajectory (Frank et al., 2002). In the presence of a disc, this gas stream will violently hit the outer rim of the disc. The resulting energy dissipation heats up this region, allowing the excess energy to be radiated away. The stream-impact location is therefore typically brighter than its surroundings and thus referred to as the *bright spot*. Its SED can contribute significantly to the overall system luminosity at UV and optical wavelengths, and it can be well studied in eclipsing systems, as shown in Figure 1.4.

1.1.4.5 Boundary layer and Corona

While the accretion disc radiates up to half of the gravitational potential energy of the accreting material, the remaining half is associated with the rotational kinetic energy of material at the inner disc edge. If the accretor is a non-magnetic object with a solid surface, this energy will be released in an interface region between the accretion disc and the accretor's surface. This region is called the *boundary layer* (BL) and is relatively narrow (a few percent of the radius of the object). In the BL, material orbiting at the Keplerian angular velocity of the inner disc edge ($\Omega_K(r) = \sqrt{GM_1/r^3}$) is transported to the surface of the compact object, which normally spins at a much slower angular velocity.

Material in the BL is spun down via a series of oblique shocks before landing on the surface of the accreting object (Pringle & Rees, 1972; Hertfelder et al., 2013). In CVs, at low accretion rates, the spectrum of this component is dominated by hot, optically thin emission ($k_BT \sim 10$keV) accompanied by emission lines associated with highly ionised species (e.g. Mukai & Patterson, 2004; Mukai, 2017). At higher accretion rates, a relatively cool, optically thick black-body spectrum ($k_BT \sim 10$eV) peaking in the extreme-ultraviolet/soft X-ray region is typically observed (Mauche, 2004b). However, these two regimes may not be mutually exclusive, and both might be present in some or all accretion states (see Figure 1.5, Mauche, 2004a; Hertfelder et al., 2013).

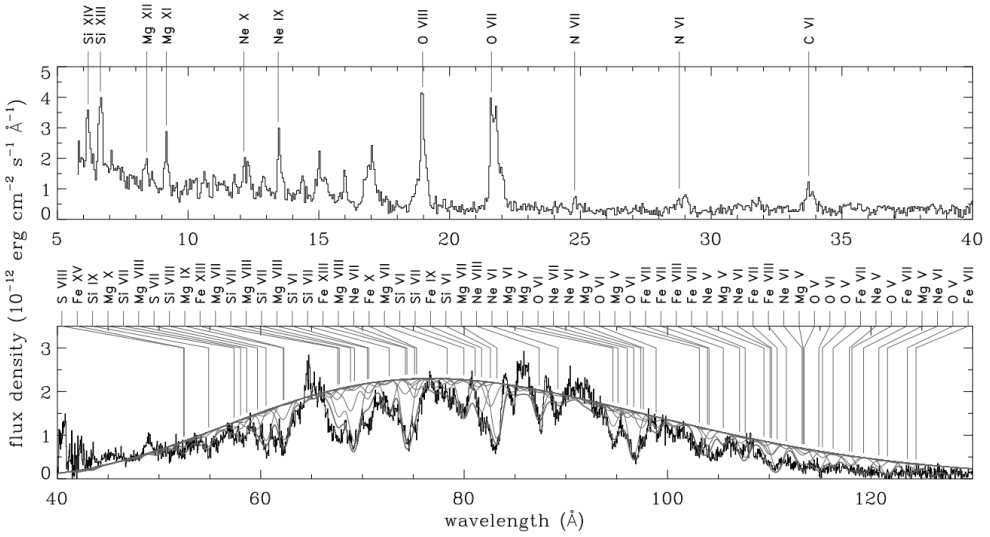

FIGURE 1.5: Chandra/LETG extreme-UV (EUV) spectrum of SS Cyg during outburst shows an absorbed blackbody spectrum (tick gray curve) with individual ion spectra (thin gray curves) with the strongest lines labelled on top. Adapted from Mauche (2004c).

In LMXBs there is also an optically thin geometrically thick inner region, normally referred as coronal emission. The X-ray irradiation of the inner accretion flow causes it to expand forming an extended atmosphere gravitationally bound to the central object

(Begelman et al., 1983; Done et al., 2018a). During early and final stages of an outburst, the X-ray high energy spectrum of LMXBs is dominated by this component, composed by a non-thermal emission arising from the electrons in the hot plasma. This emission may be the analogue of the optically thin BL observed in CVs, however, this is not certain since BHs have no solid surface.

1.1.4.6 Jet

Whenever the X-ray spectra of a LMXRBs are dominated by coronal emission, they normally also exhibit strong radio emission from a compact radio jet. During transitions to disc-dominated states, relativistic plasma ejections are also often detected at radio wavelengths (e.g. Mirabel & Rodríguez, 1999). In some cases, jet emission can be traced even into the near-infrared (NIR) band. Intraband lags can then be used to estimate the characteristic size of the jet base, which turns out to be $\simeq 0.1$ light seconds Gandhi et al. (2017). Recently, radio emission from jets has also been seen in some CVs (e.g. Coppejans & Knigge, 2020; Hewitt et al., 2020,). I will discuss the relation of the spectral states and system components in Section 1.6.1.

1.1.4.7 Disc wind

The material in the atmosphere of an accretion disc can be ejected by thermal pressure, radiation pressure or magnetic forces. In CVs, their signatures are most commonly observed in the strong UV resonance lines: Lyman α 1216 Å, N V 1240 Å, Si IV 1400 Å, C IV 1550 Å, Mg II 2800 Å). UV continuum photons encountering these ions in the outflow can be efficiently scattered out of our line of sight, thus producing blue-shifted absorption or P-Cygni profiles in these transitions (e.g. Howarth & Prinja, 1989; Prinja et al., 2000). However, in some systems such features are also detected in optical recombination lines and/or hot/highly ionised X-ray lines (Kafka & Honeycutt, 2004; Díaz Trigo & Boirin, 2016).

Accretion disc winds are another central theme of this thesis, so they are discussed in more detail in Section 1.6.2.

1.2 Observational signatures: emission and absorption lines

Astronomy is an observational science, i.e. we cannot set up the experiments, in the sense that we cannot control the phenomena we observe. However, we can design observations to test specific hypotheses. This requires an understanding of the observational signature we have access to.

In general, astronomy is based on the study of the light we receive from celestial objects. From this, we can attempt to infer the underlying physical processes that control the behaviour of the systems under study. In this section, we are going to give a very brief overview on the basis of radiative transfer, to refresh some concepts that will help us gain intuition for the upcoming chapters. For a more extended discussion, the reader is referred to, for example, Boehm-Vitense (1989) and Mihalas (1978).

1.2.1 The equation of radiative transfer

Our goal is to describe a beam of radiation that traverses through a volume of gas. We consider a light beam crossing a surface dA in a plane parallel approximation. The amount of monochromatic energy, E_λ, per second crossing a area dA in the $\hat{z}$ direction with a opening solid angle $d\omega$ is given by

$$E_\lambda = I_\lambda \, d\lambda \, d\omega \, dA \tag{1.18}$$

where the *specific intensity*, I_λ, is the energy per unit time, unit area, unit wavelength and unit solid angle.

As the beam travels through an path element ds, a fraction κ_λ of the incident energy will be absorbed by the gas along ds, so the energy is E_λ is reduced by

$$dE_\lambda = -\kappa_\lambda \, E_\lambda \, ds. \tag{1.19}$$

At the same time there is also emission from the volume $dV = dA \, ds$, given by

$$dE_\lambda = \epsilon_\lambda \, d\lambda \, d\omega \, dA \, ds, \tag{1.20}$$

where ϵ_λ is the amount of energy emitted per second, volume, energy band and solid angle. Combining absorption and emission, and expressing dE_λ in terms of Eq. 1.18 we obtain

$$\frac{dI_\lambda}{ds} = -\kappa_\lambda I_\lambda + \epsilon_\lambda. \tag{1.21}$$

We now define two new quantities. First, we define the *optical depth* ($d\tau_\lambda$) as the attenuation per optical path element, $d\tau_\lambda = \kappa_\lambda \, ds$. Second, we define the *source function* as the ratio between the emitted and absorbed energy per unit volume $S_\lambda = \epsilon_\lambda / \kappa_\lambda$. Using these definitions in Equation 1.21 then yields the standard form of the *equation of radiative transfer* (1.22),

$$\frac{dI_\lambda}{d\tau_\lambda} = -I_\lambda + S_\lambda. \tag{1.22}$$

1.2.2 The formal solution

Let us consider a volume of gas in perfect thermodynamic equilibrium, not changing with time. A beam of light passing through such a volume will not change either, hence it must satisfy

$$\frac{dI_\lambda}{ds} = 0 = \kappa_\lambda (S_\lambda - I_\lambda), \tag{1.23}$$

i.e. $I_\lambda = S_\lambda$. If the gas is also optically thick, it must radiate as a blackbody, i.e. $\boldsymbol{I}_\lambda = S_\lambda = B_\lambda$. Consequently, the emissivity is then $\epsilon_\lambda = \kappa_\lambda B_\lambda$, which is known as *Kirchoff's law*.

The emissivity given by Kirchoff's law is also a good approximation for material located deep in the optically thick regions of stellar/disc atmospheres or interiors. This material is not in strict, global thermodynamic equilibrium, since the temperature here changes with position. However, these changes are slow – they occur on scales that are much larger than the scale on which energy is absorbed and reemitted – so such regions are said to be in *local thermodynamic equilibrium* (LTE).

Kirchoff's law gives us a clear interpretation of the physical meaning of the source function S_λ. However, in order to interpret astrophysical spectral lines, we need to understand the solution of the radiative transfer equation. By solving the differential equation (1.22), it can be shown that the intensity, I_λ, emerging after crossing though a gas with optical depth τ_λ is

$$I_\lambda = I_{\lambda,0}\, e^{-\tau_\lambda} + S_\lambda (1 - e^{-\tau_\lambda}), \tag{1.24}$$

where $I_{\lambda,0}$ is the incident beam of light. So the first term in the right-hand side describes the amount of the *incident* radiation that emerges from the other side of the gas, while the second term accounts for the contribution of the gas itself to the emergent radiation.

1.2.3 Spectral lines

In the absence of a background source of light, i.e. $I_{\lambda,0} = 0$, the radiation emitted by a parcel of gas is just $I_\lambda = S_\lambda (1 - e^{-\tau_\lambda})$. We can now distinguish two extreme cases:

- *The optically thin limit* ($\tau_\lambda << 1$): In this extreme case we can expand the exponential in a Taylor series to obtain $I_\lambda = \tau_\lambda S_\lambda$. The optical depth τ_λ is large at wavelengths where the opacity κ_λ is large, i.e. at the wavelengths corresponding to transitions between allowed energy levels in the atomic species found in our

gas parcel. Thus, in an optically thin gas, we expect to see emission lines, because high opacity is associated with high intensity in this regime.

- *The optically thick limit ($\tau_\lambda >> 1$)*: At very large optical depth, the exponential term tends to 0. In this case, the observed spectrum is the source function, $I_\lambda = S_\lambda$. In (L)TE, $S_\lambda = B_\lambda$, i.e. we would see a blackbody spectrum with no spectral lines of any kind.

1.2.4 Absorption lines and emission lines in the presence of a background source

Let us now assume that there is a background source, such as the photosphere of a star, i.e. $I_{\lambda,0} \neq 0$. If the optical depth through our parcel is high everywhere, $\tau_\lambda >> 1$ for all wavelengths, the emergent spectrum is again just the source function of the gas, S_λ. However, if the foreground parcel is optically thin, the emergent spectrum can be written as

$$I_\lambda = I_{\lambda,0} + \tau_\lambda(S_\lambda - I_{\lambda,0}). \tag{1.25}$$

This equation shows that, if $I_{\lambda,0} > S_\lambda$, the emergent intensity is dominated by the background spectrum, minus a factor that is proportional to the optical depth. Since transitions between atomic energy levels are associated with larger opacities, they will produce more attenuation, resulting in an absorption line spectrum.

It is instructive to consider the special case where the background source is a blackbody, $I_{\lambda,0} = B_{\lambda,bg}$, and the foreground parcel is in LTE, so that $S_\lambda = B_{\lambda,fg}$. In this case, Equation 1.25 becomes

$$I_\lambda = B_{\lambda,bg} + \tau_\lambda(B_{\lambda,fg} - B_{\lambda,bg}). \tag{1.26}$$

This provides a useful way to understand the formation of absorption lines in stellar atmospheres. Here, temperatures increase inwards (towards the stellar core), so, in every layer of the atmosphere, $B_{\lambda,bg} > B_{\lambda,fg}$. As a result, the emergent spectrum displays absorption lines. Thus the absorption lines we see in the spectra of stars are a direct consequence of the temperature gradient in the stellar photosphere.

By contrast, $S_\lambda > I_{\lambda,0}$ is required for the formation of emission lines. In the context of LTE, this corresponds to $B_{\lambda,fg} > B_{\lambda,bg}$, and hence $T_{eff,fg} > T_{eff,bg}$. Thus emission lines will be produced if there is a *temperature inversion*, i.e. if the temperature of the foreground material exceeds that of the background source.

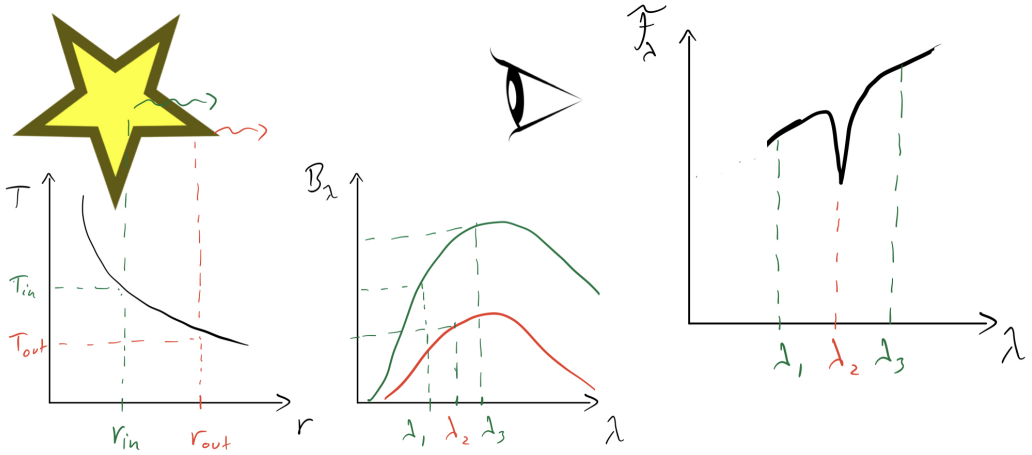

FIGURE 1.6: Schematic of spectral line formations. The light emitted by the different layers of the star are characterised by different temperatures. At resonant wavelengths the opacity increases dramatically (λ_2). Hence the emergent light will correspond to outer and cooler layers with lower intensity, this is reflected in the observed spectrum (F_λ) as an absorption line.

Most interacting binaries display strong emission lines. These are commonly seen in accretion discs where the dissipation profile in the disc might increase toward the surface (hence the temperature, Section 1.4.8). Due to the tidal lock in the system the companion is always exposing the same side of the star to the strong x-ray heating of the inner accretion flow. This significantly heats the surface of the companion producing the temperature inversion. In this case the source function of the irradiated optically thin atmosphere increases outwards producing prominent lines, for example the optical lines in He II ($\lambda = 4686$ Å), and the Bowen blend composed by the N III and C III complex at $\lambda \sim 4640$ Å(e.g. Casares et al., 2006).

1.3 The Eddington luminosity

Radiation pressure can provide an outward force that balances the inward pull of gravity. This is how stars retain hydrostatic equilibrium, for example. However, this also implies that there must be a maximum luminosity for any radiating object held together by self-gravity, since otherwise it will be blown apart by radiation pressure. This limit is known as the *Eddington luminosity*.

Consider a spherical, radiating object whose luminosity L is generated at $r = 0$ and which is composed of ionized hydrogen. The dominant process by which photons interact with matter is then electron scattering, and the outward force exerted by radiation pressure at some radius r in the object can be written as

$$F_{rad} = \frac{\sigma_T L}{4\pi r^2 c} \tag{1.27}$$

where $\sigma_T = 6.65 \times 10^{-25}\text{cm}^2$ is the Thomson cross-section. This force acts against the gravitational force, which, for a hydrogen gas, is

$$F_{Grav} \simeq GMm_p/r^2, \tag{1.28}$$

where m_p is the proton mass. Hence, radiation pressure will overcome if the luminosity exceeds so-called the Eddington limit, given by

$$L_{\text{Edd}} = \frac{4\pi GMm_p c}{\sigma_T} \simeq 1.3 \times 10^{38} \frac{M}{M_\odot} \text{ erg s}^{-1} \tag{1.29}$$

In accreting systems, where L is dominated by accretion luminosity, the Eddington limit sets an (approximate) upper limit on the accretion rates that can be supported by a given system. This limit can be obtained by setting $L_{Edd} = L_{acc}$ (cf Equation 1.3).

Given the all assumptions made to derive this quantity, it is not going to hold in detail in every astrophysical situation. For example, in binary stars, accretion is likely to happen via the formation of an accretion disc rather than via spherical accretion. However, the standard Eddington limit always provides an order-of-magnitude estimate that is useful for characterising different accretion regimes.

1.4 Accretion and accretion discs

1.4.1 Disc formation

The material transferred via Roche lobe overflow carries an excess of specific angular momentum that prevents it from accreting directly onto the compact object. After it passes through the L_1 point, it follows a ballistic trajectory that traces an elliptical orbit around the compact object. Tidal forces from the secondary cause this orbit to precess, but, in any case, the stream will clearly end up intercepting itself (Lubow & Shu, 1975). The gas then dissipates its internal energy via internal shocks, but the angular momentum of the colliding particles must be conserved, thus the gas relaxes to the minimum energy state for its angular momentum, i.e. a circular Keplerian orbit at the radius that matches the angular momentum it had when it left the L_1 point (Flannery, 1975). This radius is known as the *circularisation radius* (Frank et al., 2002), R_{circ},

$$\frac{R_{circ}}{a} = \left(\frac{R_L}{a}\right)^2 (1+q), \tag{1.30}$$

and also provides a useful lower upper limit for the outer radius of an accretion disc.

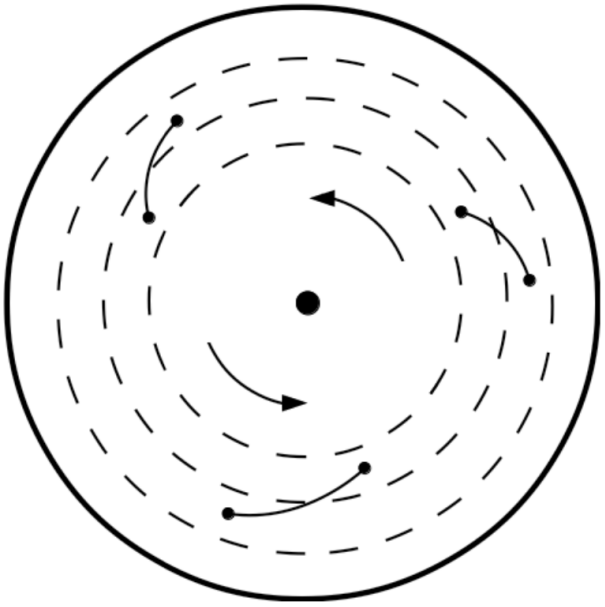

FIGURE 1.7: Face-on schematic of an accretion disc illustrating the magneto rotational instability proposed by Balbus & Hawley (1991). Magnetic field lines connect parcels of gas at different radii. The differential rotation in the disc stretch the magnetic lines resulting in the exchange of angular momentum in the radial direction. Credit Hellier (2001).

Once a ring has formed near R_{circ}, dissipative processes (such as shocks and viscous dissipation) will take place, transforming the orbital energy into internal gas energy. Some of this energy will be radiated away, while the internal torques allow the redistribution of angular momentum. Most of the material therefore slowly spirals inwards, while the outer edge of the ring spreads outwards to conserve angular momentum. This gives rise to the formation of an accretion disc.

1.4.2 Viscosity, angular momentum transport and the α prescription

From the above picture it is clear that the transport of angular momentum by and through the disc is a crucial ingredient for accretion. However, the mechanism by which this happens is still not fully understood. Molecular viscosity is dynamically unimportant in accretion flows (Pringle, 1981), and this led to alternative mechanisms being proposed over the years. The most widely accepted is the magnetorotational instability (MRI; Balbus & Hawley, 1991). This requires the gas in the accretion disc to be ionised, so that magnetic field lines can allow communication between "blobs" of gas at different radii. At each annulus, gas will rotate at its Keplerian velocity, so a gas parcel at a larger radius will move slower than one at a smaller radius. Thus the field line connecting them is stretched, and magnetic forces will tend to pull on the inner blob causing it to lose energy and thus move to a lower orbit. By contrast, the outer gas parcel will gain energy and angular momentum from the inner blob, causing it to move

to a higher orbit. The net result is an outward flux of angular momentum that allows most of the material in the disc to move inwards towards the central object (Figure 1.7).

However, other angular momentum transport (or loss) mechanisms have been proposed as well, e.g. spiral shock waves (Ju et al., 2016; Arzamasskiy & Rafikov, 2018) or magneto-hydrodynamic outflows (Blandford & Payne, 1982). Note, however, that an accretion disc driven entirely by an MHD wind would actually be dark, since there would be no viscous dissipation in this case (e.g. Spruit, 1996; Knigge, 1999).

Given that the angular momentum transport mechanism in accretion discs is still not fully understood (and may differ in different types of systems), it is convenient and useful to parameterise our uncertainty via an *effective viscosity*. This approach was developed by Shakura & Sunyaev (1973), who introduced the so-called *α-prescription*. Here, the viscosity is pictured as being driven by turbulent eddies that move with a characteristic speed. The velocity and size of these eddies are naturally constrained by the scale height of the disc, H, and the sound speed of the medium, c_s. Hence, the viscosity, ν, can be written as

$$\nu = \alpha c_s H, \tag{1.31}$$

where α is then expected to be $\lesssim 1$.

In short, the α parameter encapsulates the unknown details about the mechanisms responsible for viscosity and angular momentum transport. Observational values for AWDs in outburst tend to fall in the range $\alpha \sim 0.1 - 0.2$ (Hirose et al., 2014; Coleman et al., 2016; Scepi et al., 2017), but values up to $\alpha \sim 1$ have been claimed in the case of LMXBs (Tetarenko et al., 2018c).

1.4.3 The effective temperature distribution of a steady-state disc

By considering the equations of mass and angular momentum conservation for each annulus in the disc, it is possible to derive the rate at which energy is dissipated by viscosity as a function of radius. If we take the disc to be geometrically thin and optically thick, with a constant accretion rate, this dissipated energy will be released locally in the form of blackbody emission with a characteristic temperature. It can be shown that the resulting temperature profile of the disc, $T_{eff}(R)$, is independent of α (Pringle, 1981) and given by

$$T_{eff}(r) = \left\{ \frac{3GM_1\dot{M}}{8\pi\sigma r^3} \left[1 - \left(\frac{R_1}{r} \right)^{1/2} \right] \right\}^{1/4}, \tag{1.32}$$

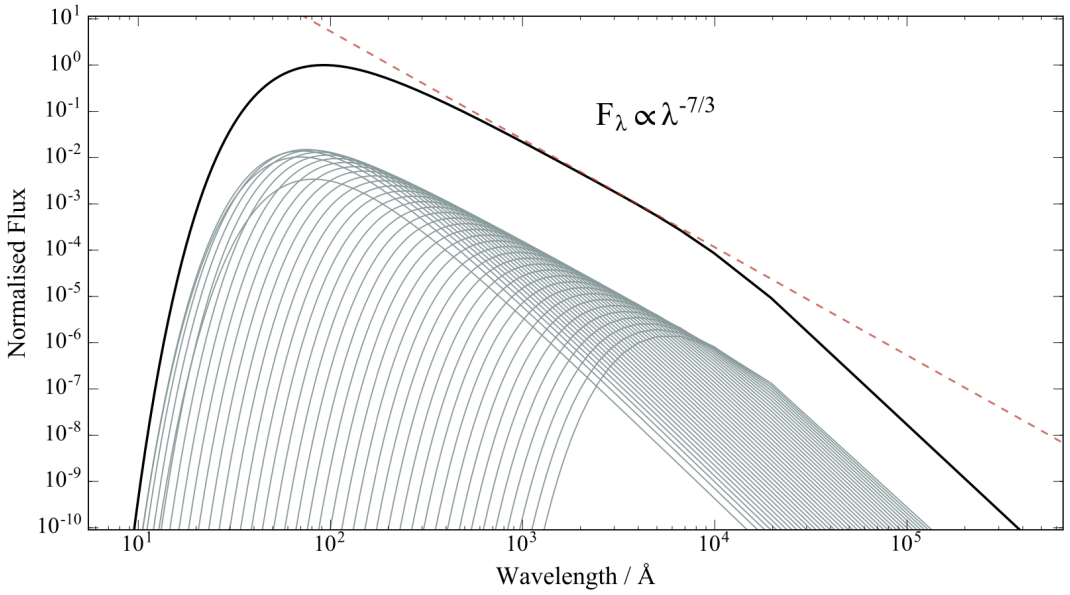

FIGURE 1.8: Spectrum of the Shakura & Sunyaev (1973) accretion disc model for $R_{out} = 100\ R_{in}$. The overall spectrum (thick line) is composed by the contribution of the emission from each annulus of the disc (thin gray lines). The dashed line with spectral index $-7/3$ is represented to guide the eye. Adapted from Hernandez Santisteban (2016).

where σ is the Stefan-Boltzmann constant. We can integrate Equation (1.32) to obtain the total luminosity of the disc, L_{disc},

$$L_{disc} = 2\int_{R_{in}}^{\infty} T_{eff}(r)\, 2\pi r\, dr = \frac{GM\dot{M}}{2R_{in}} = \frac{1}{2}L_{acc}\,. \tag{1.33}$$

Hence, half of the accretion energy (Eq. 1.1) is radiated by the disc, while the remaining is stored in the form of rotational kinetic energy and ultimately liberated in the BL (for solid accretors, Section 1.1.4.5) or advected into the event horizon (for BHs).

If each annulus in the disc emits as a blackbody, we can determine the emergent spectrum. The overall spectral energy distribution (SED) of the disc is the superposition from all the concentric rings at different radii, each with an effective temperature given by Equation 1.32. The observed monochromatic flux of the disc, F_ν, is then given by

$$F_\nu = \frac{2\pi\cos i}{d^2}\int_{R_{in}}^{R_{out}} I_\nu\, r\, dr, \tag{1.34}$$

where I_ν is the specific intensity of the annulus, R_{in} and R_{out} are the inner and outer radius of the disc, respectively, and $2\pi r\ dr \cos i/d^2$ is the solid angle of a ring with thickness dr as seen from a distance d at inclination i. For a disc made up of blackbodies, I_ν follows Planck's law, i.e. $I_\nu = B_\nu[T(r)]$, so

$$F_\nu = \frac{4\pi h\nu^3 \cos i}{c^2 d^2} \int_{R_{in}}^{R_{out}} \frac{r\, dr}{e^{h\nu/k_B T_{eff}(r)} - 1}, \tag{1.35}$$

where h is Planck's constant. When the disc is sufficiently large ($R_{out}/R_{in} \gtrsim 100$), the central part of the emergent spectrum has a characteristic power-law shape, $F_\nu \propto \nu^{1/3}$ (or $F_\lambda \propto \lambda^{-7/3}$ in wavelength space, see Figure 1.8).

1.4.4 Steady discs

The standard Shakura & Sunyaev (1973) disc model considers a fully ionised, steady-state accretion disc, in which the mass transfer rate is constant, and relativistic effects are negligible. Perhaps the closest match to these idealised conditions in nature are the discs of nova-like variables (NLs). NLs are a sub-class of CVs in which the mass-supply rate from the secondary star is high enough for the the accretion disc to remain in a steady, fully ionised state (Lasota, 2016). However, real discs are not blackbodies – they must have an atmosphere. Indeed, this is clear from the spectra of NLs (see Figure 1.9), which show many of the features familiar from stellar atmospheres, such as absorption edges and lines.

Attempts to model these spectra in detail have been carried out, typically by summing over stellar atmospheres instead of blackbodies, while retaining the effective temperature distribution predicted by α-disc theory. But these models generally over-predict the depth of the Balmer jump and the slope of the spectrum in the ultraviolet (e.g. Hubeny & Long, 2021). Recent modelling of the spectrum of the NL *IX Vel* by Hubeny & Long (2021) suggests these deviations from stellar atmosphere SEDs may be due to a flatter distribution of the vertical temperature profile in the atmosphere of the disc. Such a profile can arise if a significant fraction of the energy dissipation takes place in the outer layers of the disc atmosphere.

1.4.5 Unstable discs

Many accreting systems exhibit dramatic episodes, where their brightness can quickly increase by several orders of magnitude. In most cases, these episodes last for relatively short periods of time (i.e. shorter than the interval between eruptions). The plausible cause for these outbursts is thought to be the release of gravitational energy in the accretion disc, due to a temporary large increase in the rate of mass transfer through it. These transient systems are important, partly because most accreting compact binaries fall into this category, and partly because the change in the physical conditions of the plasma allows us to probe fundamental properties of accretion discs (Hameury, 2020).

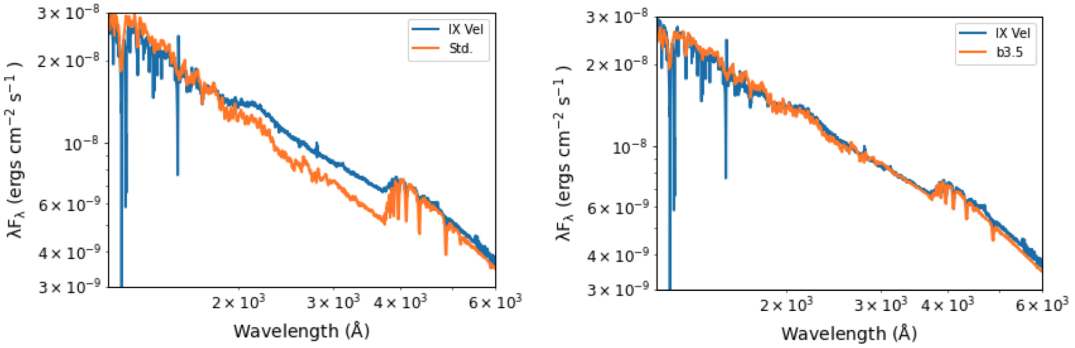

FIGURE 1.9: HST spectrum of the steady-state accretion disc of *IX Vel* in blue, accretion disc models are shown in orange. **Left:** standard approach where the accretion disc is modelled as a standard stellar atmosphere with all the energy released in the mid plane of the disc. The Balmer jump and the UV slope are clearly overpredicted by the model. **Right:** Best model from Hubeny & Long (2021) with a parametrised dissipation law, that implies significant fraction of the energy is deposited in the surface layers of the disc. Adapted from Hubeny & Long (2021).

1.4.5.1 The disc instability model (DIM)

Arguably the best interpretation for the observed transient of these systems is the disc instability model (DIM, Smak, 1971; Osaki, 1971; Lasota, 2001; Hameury, 2020). In this model, the increase in mass accretion rate through the disc is driven by a thermal-viscous disc instability that is associated with the strong temperature dependence of the opacity in a partially ionised hydrogen plasma (Frank et al., 2002).

In such a plasma, which is typically found at temperatures T$\sim$7000 K, some of the free electrons combine with hydrogen atoms creating H^- ions. These are particularly efficient at absorbing photons, so that the opacity of partially ionised hydrogen scales as $\kappa \propto \rho^{1/3} T^{10}$, where ρ and T are the density and temperature of the gas, respectively. If one tries to heat the gas further, instead of heating it, the energy mainly goes into creating more ions (Hellier, 2001). As a result, the thermal equilibrium curve of such a plasma – e.g. in the effective temperature (T_{eff}) vs surface density Σ plane – will exhibit an S-shape (see Figure 1.10). To the right of the curve, heating exceeds cooling; to the left, cooling exceeds heating. Disc annuli finding themselves on the upper or lower branch of this curve are in a stable equilibrium. For example, a small upward fluctuation in surface density moves them into the regime where heating takes place. Their temperature then increases and they rejoin the equilibrium curve on the same branch. However, the middle branch is unstable. Here, the same fluctuation will cause the annulus to heat up until it reaches the upper stable branch. The temperature and viscosity are much higher on this branch, so the accretion rate is also higher. The instability can therefore spreads to the whole disc via a cascade effect. During the outburst, the mass-transfer rate is higher than the mass supply rate from the donor, so the disc is drained until its annuli again reach the unstable branch (now from above) and drop back onto

the lower branch, which corresponds to quiescence. For a more detailed review see Lasota (2001), Osaki (2005).

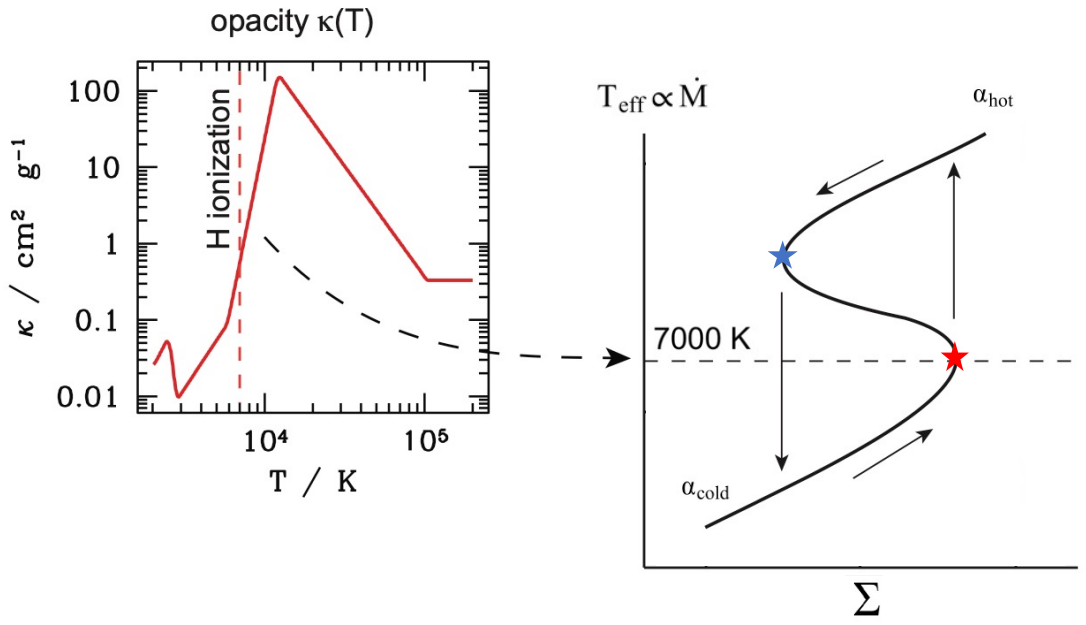

FIGURE 1.10: Schematic of a disc outburst as envisaged by the disc instability model. **Left:** the dependency of the opacity with temperature, where extreme increase in the former is clear until the hydrogen is fully ionised. **Right:** the so-called stability curve of accretion discs, it relates the temperature with surface density. The arrows indicate the direction of variations in the local conditions in the disc over the course of an outburst. The solid line correspond to heating equals cooling of in a ring of gas, to the right of the curve, heating exceeds cooling; to the left, cooling exceeds heating. Stars are at the critical surface densities at which a ring of the disc where transitions from the two stable branches can occur (hot and cold branch). The middle branch is unstable, so any small perturbation will end up in the stable branches (see text for details). Adapted from Armitage (2011).

Among AWDs, systems exhibiting these outbursts are referred to as dwarf novae (DNe); among LMXBs, they are referred to as X-ray novae. The recurrence times of these outburst can range from $\sim$ 10 days to tens of years or longer.

One of the key predictions of the DIM is the existence of a critical mass transfer rate ($\dot{M}_{crit}$), above which systems will remain permanently on the hot, stable branch, whereas systems below it will have unstable accretion discs exhibiting outburst cycles. Dubus et al. (2018) successfully tested this prediction of the DIM using a sample of about 130 AWDs with accurately determined distances by *GAIA* mission. They estimated the time-averaged mass transfer rate from optical light-curves and showed that DNe are characterised by rates below $\dot{M}_{crit}$, while the rates in NLs lie above this limit. They also confirmed the hypothesis that the mass accretion rates of *Z Cam Stars* (a third sub-class of AWDs, which most of the time exhibit the properties of NLs with some periods of "quiescence") are clustered around $\dot{M}_{crit}$.

However, the standard DIM cannot reproduce the long recurrence timescales of XRBs, and the predicted critical accretion rate does not cleanly separate steady and transient systems. Part of the solution to these problems is probably the truncation of the inner disc by either magnetic pressure (e.g in NS systems) and/or evaporation (Meyer & Meyer-Hofmeister, 1994) and/or the formation of a hot, optically thin, radiatively inefficient flow and/or the launching of a jet (e.g. Lasota et al., 1996; Narayan & McClintock, 2008). However, perhaps even more importantly, the outer regions of discs in LMXBs strongly irradiated by X-rays from the inner regions (van Paradijs & McClintock, 1994; van Paradijs, 1996; King & Ritter, 1998). This not only changes their observed spectrum, but also their effective temperature and hence their stability curves. By accounting for irradiation in the DIM, Coriat et al. (2012) showed that the resulting $\dot{M}_{\rm crit}$ successfully separates transient and steady X-ray binaries. Despite this, simulations show that the X-ray flux from the inner accretion flow can be easily screened by the disc itself (Dubus et al., 1999). This suggests the existence of a hot, vertically extended corona (probably the base of the jet) and/or the importance of scattering of the inner X-rays by outflowing material, (likely a thermal wind, Dubus et al., 2019).

1.4.6 Elliptical discs

The outer disc of a system is more influenced by the gravitational pull of the secondary star, causing radial pull in some of the gas in the disc. When the orbital frequency of the gas around the disc is commensurate with the angular frequency of the binary system, the particles will be "pushed" in the same direction in each cycle. Hence, this material can enter into a resonance that sustains the elliptical shape of the outer disc. This scenario produces a prograde precession of the elliptical component of the disc which will cross the inner annulus at smaller radii with circular orbits (Whitehurst & King, 1991). In this region, the ballistic orbits intersect each other enhancing the energy dissipation.This extra contribution to energy released by the disc is often referred in the literature as (positive) *superhumps* (SHs, Patterson et al., 2005). The observational signature of sumperhumps is a periodic modulation of the light curve at the beat period of the precession frequency and the orbital period. This beat period is slightly longer than the orbital period, and the corresponding "period excess" is defined as $\epsilon_+ = (P_{SH+} - P_{orb})/P_{orb}$.

Some DNe undergo 'superoutbursts' (van Paradijs, 1983), these are longer than regular outbursts, they are believed to be triggered by the disc exceeding the critical radius entering into the 3:1 resonance. Systems exhibiting these superoutbursts are called SU UMa stars after the prototype of these systems *SU Ursae Majoris*. Extreme mass ratios ($q \lesssim 0.3$ for CVs) favour the formation of superhumps since $R_{disc}(q)$ decreases faster with q than the resonance radius, making systems with more extreme mass ratios having the 3:1 resonance inside the primary Roche Lobe (Whitehurst, 1988; Whitehurst &

King, 1991). The relation of the mass ratio with the presence of superhumps and the Roche lobe geometry allow the estimation of the mass ratio of systems from their photometric periodicity. This was well studied by Patterson et al. (2005) in the case of CVs. LMXBs and in particular black hole systems typically possess very low mass ratios, favouring the formation of eccentric discs and associated SHs. However, here the period differential between the orbital and superhump period is very small, making them harder to detect. Despite this, several detections have been published in the literature (e.g. O'Donoghue & Charles, 1996; Casares & Jonker, 2014; Kosenkov & Veledina, 2018).

1.4.7 Tilted discs

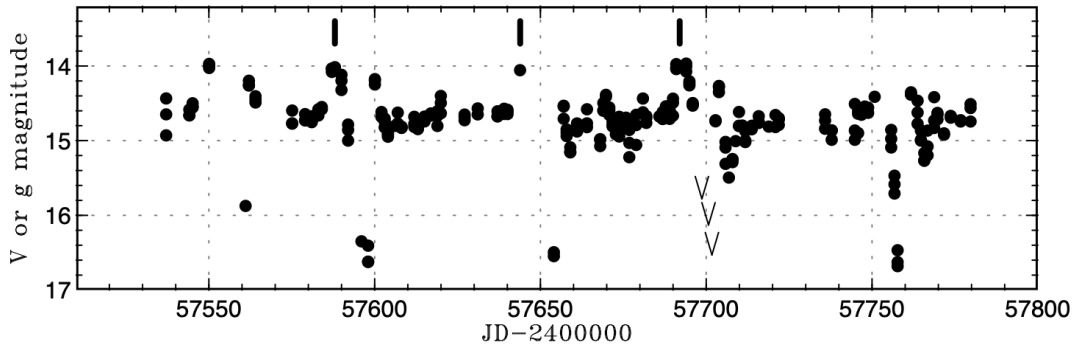

FIGURE 1.11: Light curve of IW And from ASAS-SN data (Kochanek et al., 2017). Vertical ticks indicate the brightening terminating stand-stills with an eclipse-like event. Adapted from Kato (2019).

A tilted accretion disk, due the mis-alignment of the accretion disk with the orbital plane, will slowly precess in the inertial frame (Wood & Burke, 2007). This nodal precession is retrograde, the time required for the tilted disc to return to a given configuration relative to the binary system is slightly shorter than the binary period. The corresponding observable signal is therefore again a light curve modulation at the beat period between the orbital period and the precession period of the tilted disc, the so-called *negative superhumps*. The corresponding period deficit is $\epsilon_- = (P_{SH-} - P_{orb})/P_{orb}$.

Barrett et al. (1988) first suggested the origin of the negative superhump as the transit of the accretion stream impact spot across the face of the tilted disc. This picture was confirmed with smoothed particle hydrodynamic simulations by Wood & Burke (2007); Wood et al. (2009). In addition, they found that the accretion disc is slightly elongated, making it larger than the disc in a non-tilted system. However, the origin of the disc tilt remains controversial; Montgomery (2009) proposed that a lift force may be the origin.

Based on this idea, Kimura et al. (2020) developed a modified DIM model in which the accretion disc is tilted with respect to the orbital plane. This model was proposed in order to explain the so-called *IW And* stars, named after their proto-type. These are a

sub set of Z Cam stars (Section 1.4.5.1) that exhibit slow ($\sim$ 2 days), large-amplitude, damped quasi-periodic oscillations in their stand still-phase (see Figure 1.11, Simonsen, 2011; Szkody et al., 2013; Kato, 2019). Given that most (if not all) the IW And stars also exhibit negative superhumps, Kato (2019) suggested that these slow signals are the result of the tilted disc. More specifically, the idea is that, due to the tilt, the mass stream can flow over the rim of the disc, landing in the inner regions and keeping them in a hot stable state. By contrast, the outer regions of the disc are subject to the thermal-viscous instability that underlies the DIM. The development of the tilted-disc DIM described by Kimura et al. (2020) successfully reproduces the strong eventual dips observed in IW And stars. However, it struggles in reproducing the low-amplitude oscillations, so further research is needed.

1.4.8 Disc-formed lines

The temperature distribution of discs vary from thousands in the outer disc to tens of thousands as we move closer to the central object. This led to a wide range of ionisation states in their spectral lines arising from different regions in the disc (Warner, 1995). For instance low ionisation states are seen in the optical, such as H I, He I, He II, Fe II, Ca II and O I, while in the UV moderately ionised species are seen (Lα, He II, C II, C IV, N II, N V and O III). In LMXBs the disc can go further inwards reaching much higher temperatures producing lines in the X-ray region of the spectrum.

As discussed in Section 1.2.3, an optically thick emitting region may produce either absorption or emission lines, depending on the temperature gradient through the region. Absorption lines are seen if the temperature increases with (optical) depth, as is the case in "normal" stellar atmospheres and interiors. By contrast, the formation of emission lines requires a temperature inversion, i.e. the line-emitting layer must be at a higher temperature than deeper-lying background layers. Both situations can be encountered in accretion discs.

Emission lines are most commonly observed, most likely because the upper layers of the disc tend to be irradiated by the compact object itself, by the inner disc regions, by the BL and/or by the corona in LMXBs. This irradiation tends to heat these layers, resulting in a temperature inversion and the production of emission lines.

1.4.8.1 Double-peaked emission lines

Owing to their particular geometry and kinematics, the emission lines produced by accretion discs have a very characteristic shape. Given the high rotational velocity of the gas spiralling around the compact object (up to thousands of kilometres per second), the emission lines are highly Doppler-broadened. These disc lines are generally

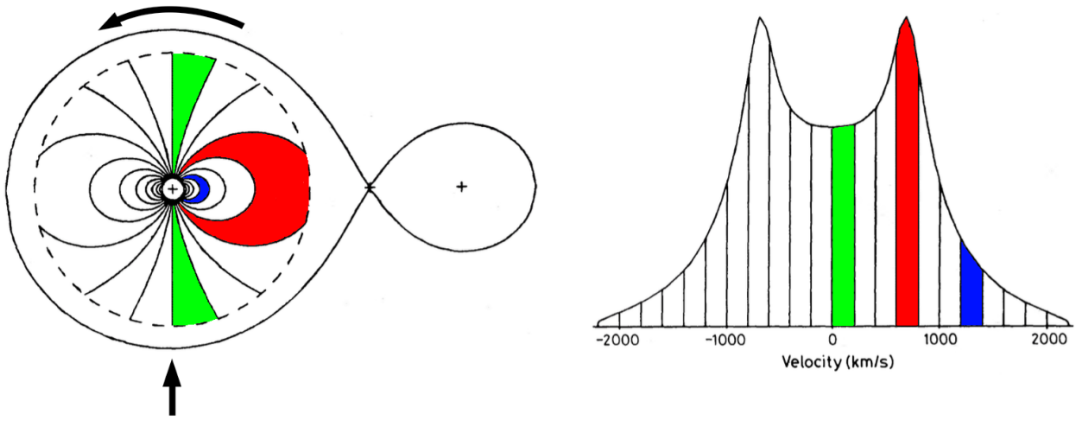

FIGURE 1.12: Schematic of double peaked emission line formation in accretion discs. **Left:** Roche lobe of a system with $q = 0.15$, edge on view of the accretion disc is indicated with the vertical arrow. Different colours highlight regions of constant Kepplerian velocity forming a dipole pattern in the disc surface. **Right:** double peaked profile owing to the line-of-sight projected velocity of the disc, colours in velocity space match the area of the disc where they are originated. Adapted from Horne & Marsh (1986).

characterised by a double-peaked profile, arising from the projection of the Keplerian velocities onto the line-of-sight (Figure 1.12). The faster spinning innermost regions create the broad wings in the line profile. The line flux decreases with increasing velocity here, due to the smaller area of these regions (shaded blue in Figure 1.12). On the other hand, orbiting material lying along the line-of-sight toward the compact object will have no radial velocity component at all, forming the central core of the line (shaded green in Figure 1.12). The radial velocity associated with the largest area corresponds to the projected velocity of the outer disk, which produces the horns at each side of the core (shaded red in Figure 1.12).

The case illustrated above describes the emission associated with an optically thin emitting layer on or in the disc. Here, every parcel emits isotropically, so the emissivity is directly proportional to the area associated with a given radial velocity, producing a smooth "U-shaped" central region in the line profile (e.g. Smak, 1981). However, if the line-forming region is optically thick in the line, the optical depth along the line-of-sight also depends on the velocity gradient. This still results in a double-peaked line, but now the centre of the line has a more accentuated central dip, leading to a "V-Shaped" core (see Figure 1.13 Horne & Marsh, 1986). The dependence of the optical depth on the velocity field in the optically thick limit can also lead to single-peaked lines if the velocity gradient in the line-forming region is dominated outflow kinematics (e.g. due to a disc wind being driven from the surface) (see Section 1.6.2; Murray & Chiang, 1996).

However, accretion discs can also produce absorption lines. For example, as noted in Section 1.4.4, luminous accretion discs at sufficiently high accretion rates are optically thick, with atmospheres resembling those seen of stars with comparable (T_{eff} and $\log g$,

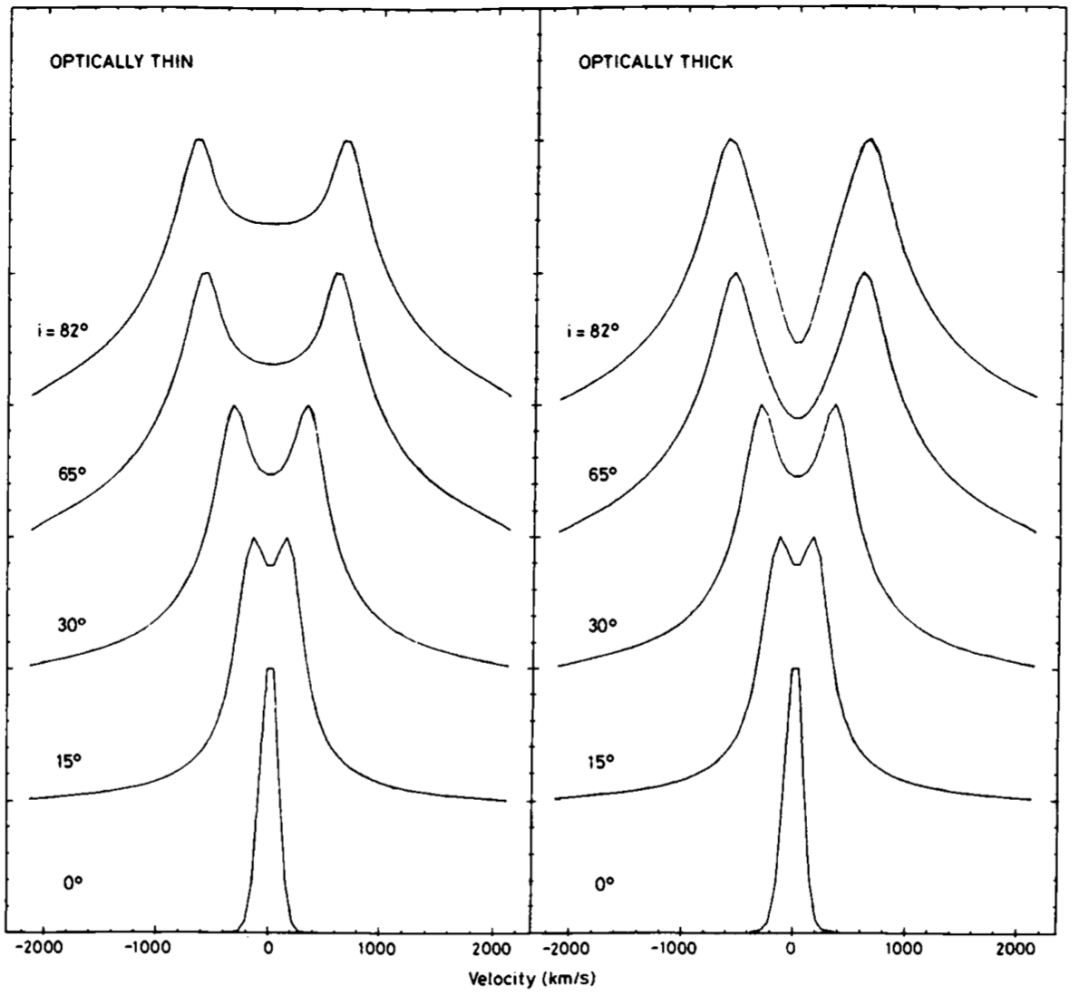

FIGURE 1.13: Double peaked accretion disc-formed lines. **Left:** the optically thin line forming region where gas emits isotropically lead to a "U-shaped" core. **Right:** optically thick line forming region leads to a "V-Shaped" core due to the velocity gradient in the line-of-sight. Adapted from Horne & Marsh (1986).

Wade & Hubeny, 1998). If most of the accretion energy is dissipated near the mid-plane, and irradiation from the inner regions is not relevant, the temperature in such disc will decrease with height, leading to the formation of absorption lines. This is the case, for example, in some NLs.

Their lines will still have a "double dip" structure due to the disc kinematics of the line-forming region, as in the case of emission lines. However, in these sources, the absorption lines are often filled with an emission core, likely formed in the irradiated face of the companion or the hotspot (Beuermann & Thomas, 1990; Beuermann et al., 1992).

1.5 Thermonuclear runaways

Accretion deposits material onto the surface of a compact object. In AWD systems, if the accretion rate is high enough, it can sustain stable H-burning on the surface of the WD. Such binaries are known as *super-soft X-ray sources, SSS* (Kahabka & van den Heuvel, 1997). Usually, however, the accreting material is not immediately burnt. In this case, as the layer of unburnt material grows, the pressure (and temperature) at its base increases. This continues until a critical pressure is reached, at which point a thermonuclear runaway is triggered in the base of the envelope. At this point, the accreted material is burnt explosively.

1.5.1 White Dwarfs: Novae

In accreting WDs, this thermonuclear explosion causes a sudden increase in brightness with amplitudes of 8-15 magnitudes at optical wavelengths. These events are referred as *classical novae* or *nova eruptions*.

Once compressional heating triggers the thermonuclear runaway in the base of the envelope, and the source erupts as a nova, the material in the envelope expands, ejecting $10^{-3} - 10^{-7} M_{\odot}$ of enriched, CNO-processed material into the interstellar medium. The radiative luminosity during the eruption is $10^{36} - 10^{38}$erg s^{-1}, close to the Eddington limit, and the process is so powerful that it is expected to tear apart the accretion disc (Figueira et al., 2018; Kato et al., 2017; José et al., 2020).

The expelled material has typical velocities of hundreds or thousands of kilometres per second. It will expand freely until it has swept up roughly its own mass from the surrounding circum- or interstellar medium. At this point, it enters a deceleration phase. The ejected material is sometimes detectable via its diffuse nebular emission, and its size and velocity can be used to estimate the time since the nova eruption (e.g. Shara et al., 2007; Sahman et al., 2015; Darnley et al., 2019).

1.5.2 Neutron stars: Type-I X-ray bursts

Thermonuclear explosions on the surface of neutron stars are known as *Type-I X-ray bursts*. They manifest as sudden and very rapid (1-10 seconds) luminosity increases, which are followed by an exponential decay that lasts between a few seconds and several minutes. The rapid rise in the light curve is associated with the propagation of the heating front after ignition takes place in the equatorial plane. The ensuing decay is due to the cooling of the burnt ashes (e.g. Grindlay et al., 1976; Hoffman et al., 1978; Lewin et al., 1993).

The detailed behaviour of Type-I bursts depends on the accretion rate (Narayan & Heyl, 2003). At low rates, the explosive material in the bursts is mainly hydrogen. If the accretion rate is high enough, however, the hydrogen is burnt into Helium when reaching the surface leading to He-rich bursts. When the accretion rate exceeds the H-burning rate the remaining H is detonated along with the He in the X-ray burst. There is also a critical accretion rate above which both H and He can burn stably at the surface. Above this rate, there are no Type-I X-ray bursts, as the accreted material is processed at the same rate at which it is supplied. However, occasionally carbon-rich bursts can still take place, which are known as "superbursts" (Cornelisse et al., 2000; Cumming & Bildsten, 2001; Strohmayer & Brown, 2002).

Type-I X-ray bursts are useful partly because they are unique to NS. Broadly speaking, NS- and BH-LMXBs share similar phenomenology, which often makes it difficult to establish the nature of the compact object with confidence. Type-I X-ray bursts therefore provide an important means by which compact objects in newly discovered XRBs can be positively identified as NSs.

1.6 Accretion-induced outflows

Accretion disc winds and jets are ubiquitous among accreting systems on all scales, from active galactic nuclei down to young stellar objects. While the former can inject significant amount of mass into the ISM, the latter often carry large amounts of kinetic energy. These outflows thus represent a key mechanism by which accreting systems interact with their environment ("feedback"), and they may also be responsible for triggering the mysterious state changes observed in XRBs (Shields et al., 1986). In this section, I will provide a short overview of these outflows, their connection with different accretion states, and – for disc winds – the possible driving mechanisms.

1.6.1 Hysteresis and disc-jet coupling

One of the most intriguing features of transient XRBs is that they exhibit a characteristic and repeatable pattern during their eruptions.

Over the course of an outburst, transient XRBs exhibit two distinct spectral states. In quiescence and on the rise, the X-ray spectrum is dominated by a hard power law component. By contrast, near the peak of the eruption and during the early decline, most of the accretion luminosity emerges in a a soft, thermal component. These spectral states are thought to be consequence of different accretion geometries close to the central object. Specifically, the hard state is associated with a hot, optically thin, geometrically thick accretion flow, which is largely replaced by an optically thick, geometrically thin accretion disk in the soft state (e.g. Esin et al., 2000; Done et al., 2007; Belloni, 2010).

Interestingly, the behaviour of radio jets in XRBs appears to be intrinsically linked to these accretion states. During the initial hard state, the radio spectrum is consistent with a partially self-absorbed, compact jet (e.g. Corbel et al., 2000). In the soft state, the jet is quenched. However, during the hard-to-soft transition, discrete ejections – along with bright radio flares – are observed for a short period of time (e.g. Mirabel & Rodríguez, 1999; Fender et al., 2004a; Tetarenko et al., 2017; Bright et al., 2020).

At radio frequencies, the hard state is characterised by a flat or slightly inverted spectrum ($\alpha \gtrsim 0$, where $S_\nu \propto \nu^\alpha$ and S_ν is the radio flux, e.g. Fender, 2001). This spectrum extends toward shorter wavelengths, until frequencies are reached at which the jet is no longer self-absorbed. The SED then changes from an optically-thick synchrotron spectrum to a steep, optically-thin spectrum ($\alpha \sim -0.7$). The break between these regimes lies in the IR region. Its location is thought to be related to the distance between the central object and the location where the non-thermal particles are first accelerated in the jet. More specifically, higher frequencies correspond to emission originating closer to the central object (e.g. Markoff et al., 2005; Gandhi et al., 2017).

This dependence of the jet properties on the spectral state is sometimes referred to as disc-jet coupling. The jet only appears to be active in the hard state, at the right hand side of the hardness intensity diagram (HID), with the so-called "jet-line" separating the jet vs no-jet regimes. (Fender, 2001; Fender et al., 2004b).

Recently, radio jets – or, strictly speaking, radio emission attributed to jets – have been also observed in AWDs (e.g. Coppejans et al., 2015; Russell et al., 2016; Coppejans & Knigge, 2020; Hewitt et al., 2020). This development was triggered by the discovery of hysteresis and an associated jet flare in the DN *SS Cyg* (Figure 1.14 Körding et al., 2008, , but also see Hameury et al. (2017)). Furthermore, inspired by the universality of accretion, Fernández-Ontiveros & Muñoz-Darias (2021) attempted to use the same hysteresis cycle to account for the different classes of AGNs. However, despite lots of the observational and theoretical efforts, the relations between the accretion flow and collimated jets remains poorly understood.

1.6.2 Disc winds

Much of the research in this thesis is focused on accretion disc winds. In this section, I will therefore discuss the underlying physical mechanisms that can drive these outflows and the observational signatures we use to study them.

1.6.2.1 Driving mechanisms

The properties and behaviour of a parcel of ideal gas can be modelled by solving the three equations of magnetohydrodynamics, which describe the conservation of mass,

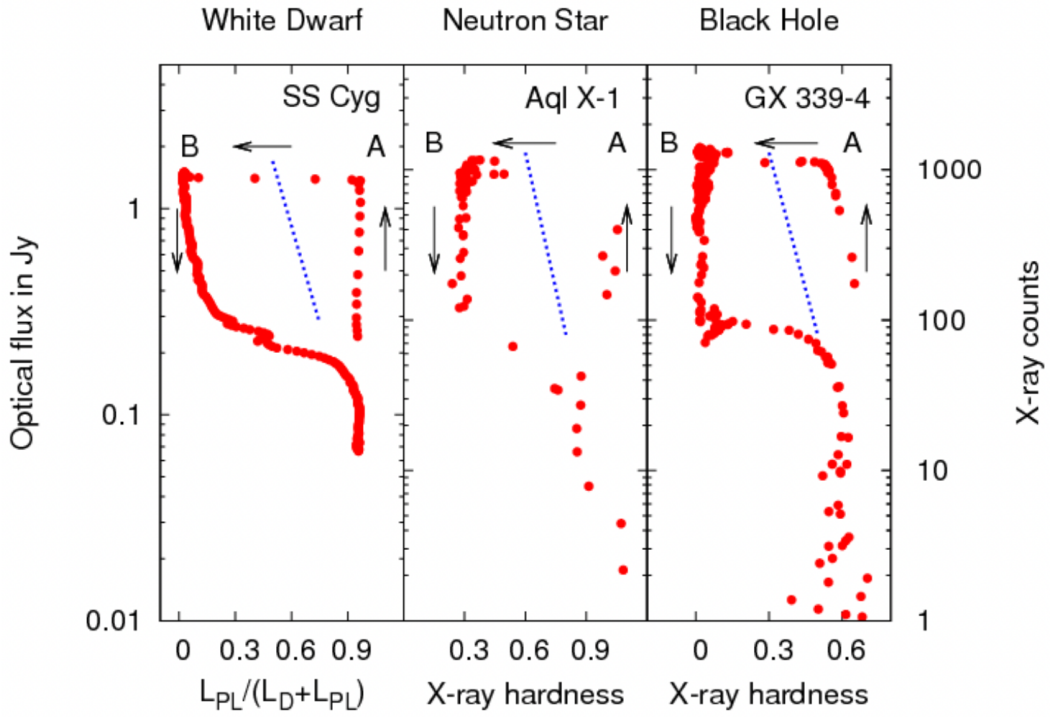

FIGURE 1.14: Hardness-intensity diagram for three types of accreting binaries. Arrows indicate the temporal evolution over an outburst cycle and the dotted line shows the "jet line". For *SS Cyg* the contribution of the disc and the non-thermal emission is derived from the X-ray power law (L_{PL}) compared to the total accretion luminosity of the system (disc and non thermal component, $L_{PL} + L_D$). Adapted from Körding et al. (2008).

energy and momentum (e.g. Frank et al., 2002). In order to illustrate the possible driving mechanism for disc winds, I will focus on the momentum conservation equation, i.e. the equation of motion. By grouping all the forces in the right hand side, this can be written as

$$\rho \frac{Dv}{Dt} = -\nabla P + \frac{1}{4\pi}(\nabla \times \vec{B}) \times \vec{B} + \rho \vec{g}_{rad} + \rho \vec{g}. \tag{1.36}$$

Here, ρ is the gas density, $\vec{v}$ is the gas velocity and D denotes a derivative in the comoving frame of the gas parcel. The quantity $\vec{B}$ is the local magnetic field, and $\vec{g}_{rad}$ is the radiation force per unit mass acting on the parcel.

The accretion process is dominated by the gravitational force $\rho\vec{g}$. Hence, for an outflow to be driven away, one or more of the other terms in the right hand side of (1.36) have to prevail over the gravitational pull. This leaves us with three potential driving mechanisms, namely

- Thermal Pressure: $-\nabla P$
- Magnetic Forces: $\frac{1}{4\pi}(\nabla \times \vec{B}) \times \vec{B}$

- Radiative Forces: $\rho\vec{g}_{rad}$

We are now going to briefly discuss the physical conditions under which each of these forces can drive material away from the gravitational field of the compact object.

Thermal driving

The gas in the disc will be in equilibrium when its thermal pressure is balanced by gravity. However, if the gas is heated up, its pressure can exceed the gravitational force, allowing it to escape the disc. This situation can occur far out in the disc, where the escape velocities are relatively low, and the disc atmosphere exceed temperatures of $\sim 10^7$ K (e.g. Done et al., 2018a). Given the intrinsic high temperatures and strong X-ray emission of accretion discs in XRBs, this mechanism offer a natural explanation for the disc winds observed in these systems (Begelman et al., 1983; Woods et al., 1996). In these systems, the disc is irradiated by the strong x-ray emitting central engine. This may launch a thermally driven wind far out in the disc, while the gravitationally bound irradiated gas closer in may explain the coronal emission observed in these objects. However, this mechanism is unlikely to be relevant in CVs, due to the much weaker irradiation in these systems.

Radiation driving

In Section 1.3, we discussed how radiation pressure acting on free electrons can halt accretion, i.e. $\rho\vec{g} = \rho\vec{g}_{rad}$. In spherical symmetry, this defines the Eddington Limit. It follows that, in accreting systems close to, or above such luminosity, ($L \gtrsim L_{edd}$), the radiation pressure on free electrons – which is communicated to the protons by Coulomb forces – will drive a wind. This mechanism may be at work in ultra-luminous X-ray sources (Walton et al., 2013) and may also be responsible for the ultra-fast outflows (UFOs) observed in some AGNs (e.g. Pounds et al., 2016).

Since the free electron scattering cross-section, σ_T, is relatively small, high luminosities are required to launch a continuum-driven wind. On the other hand, the cross-section for strong spectral lines, σ_L, is several orders of magnitude higher than σ_T near the rest wavelength of the line. Therefore, under the right ionisation conditions, spectral lines can dominate the radiation pressure and provide a significant acceleration mechanism in a partially ionised plasma with enough suitably bound electrons available (Castor et al., 1975). This mechanism is known as *line-driving*, and it is a strong candidate for driving disc winds in relatively low-luminosity, UV bright systems such as NLs and DNe in outburst (Pereyra et al., 1997; Proga et al., 1998; Matthews et al., 2015). It is also thought to be responsible for the strong mass loss observed in Wolf-Rayet and O-stars (e.g. Friend & Abbott, 1986).

In order to be efficient, line-driven winds require the presence of either strong resonant lines and/or lots of weaker lines. Its viability and properties therefore depend strongly

on the radiation field, the abundances and ionisation state of the gas. Accounting for all the transitions taking part in these interactions is rather complicated, and the most common way to deal with this is by expressing $\vec{g}_{rad}$ in terms of the Thompson cross section by introducing the *force multiplier* ($\mathcal{M}(t)$, Castor, 1974), so

$$\vec{g}_{rad} = \frac{\sigma_T \mathcal{F}}{\mu c m_p} \mathcal{M}(t), \tag{1.37}$$

where μ is the mean atomic mass, $\mathcal{F}$ is the flux and t is a so-called optical depth parameter.

The force multiplier $\mathcal{M}(t)$ can be calibrated via line-by-line calculations in O-star winds (Abbott, 1982). It depends on the physical conditions in the gas under considerations, including notably the dimensionless optical depth, t. This is proportional to the gas density, thermal speed and velocity gradient. Owocki et al. (1988); Gayley (1995) show that the maximum force multiplier is $\mathcal{M}_{max} \simeq 2 \times 10^3$, which, at low optical depths, occurs at temperatures $T \simeq 10^4 - 10^5$ K, i.e. under conditions of moderate ionisation. This is important since it give us intuition to the minimum required luminosity for line-driving to be relevant. Using (1.37), this can be written as $L/L_{edd} > \mathcal{M}_{max}^{-1} \simeq 1/2000$.

Another important consequence of the velocity-gradient dependence of line-driven flows is that they are subject to a strong instability (LDI; e.g. Lucy & Solomon, 1970; Lamers & Cassinelli, 1999). This happens because the radiation force and velocity field are coupled: a small perturbation in the flow will change the velocity gradient, which will in turn change the optical depth, and therefore the radiative force. This instability can produce a clumpy outflow, which may help to prevent over-ionisation of the wind by increasing the gas density (e.g. El Mellah et al., 2018).

Magneto-centrifugal driving

The interaction of centrifugal forces with a large-scale, ordered, strong magnetic field in the system can also drive ionised gas from the disc. This mechanism was first proposed by Blandford & Payne (1982), who also introduced a useful "bead on a wire" analogy. In this model, the magnetic field is dominated by a poloidal component emerging from both sides of the disc. If the field is inclined sufficiently with respect to the disc normal, fluid particles are forced to move outwards (by centrifugal forces) along the rotating magnetic lines. (If the geometry of the magnetic field is dominated by the toroidal component, magnetic pressure can also drive a dense outflow (Proga, 2003).)

As we discussed in Sections 1.1.3 and 1.4, large-scale magnetic fields may play an important role in binary evolution and in the transport of angular momentum in accretion discs. However, there is still a great uncertainty in the physics of these magnetic

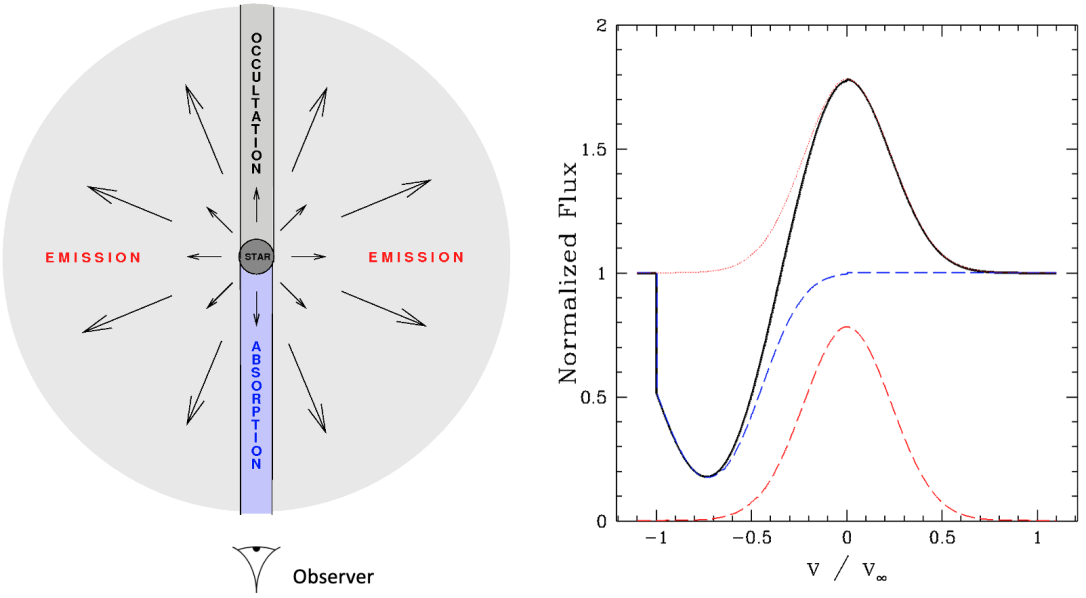

FIGURE 1.15: Geometry leading to formation of P-Cygni profiles in stars (left). The light scattered in the expanding outflow (light grey area) scatter the light of a given transition forming an emission profile (red dashed line in the right plot), while the component moving in the line of sight will form an absorption profile (blue dashed line in the right plot). The net spectral shape is a P-Cygni profile (black line). Adapted from Knigge (1995).

processes, and the existence of magnetically driven winds is difficult to probe. Nevertheless, numerical simulations have demonstrated that ordered magnetic fields can be responsible for jet production (e.g. Romanova et al., 1997), and this mechanism has been proposed as the origin of winds in AGNs and YSOs (e.g. Pelletier & Pudritz, 1992). These "magnetic winds" have also been proposed as the underlying mechanism behind the disc-jet coupling discussed in Section 1.6.1, the anticorrelation of X-ray wind signatures with the detection of the jet and the hysteresis loop observed in transient XRBs (Neilsen & Lee, 2009; Marcel et al., 2022).

1.6.3 Observables

The smoking gun evidence for outflows are blue shifted absorption troughs and/or P-Cygni profiles. However, under the right conditions, large scale signatures can also be detectable where the outflows interact with their environment. In the reminder of this introduction, I shall discuss both types outflow signatures.

1.6.3.1 Blue-shifted absorption & P-Cygni profiles

In stars, due to the spherical symmetry, an expanding, accelerating outflow with a sufficiently high optical depth in a given spectral line will present a P-Cygni profile (see

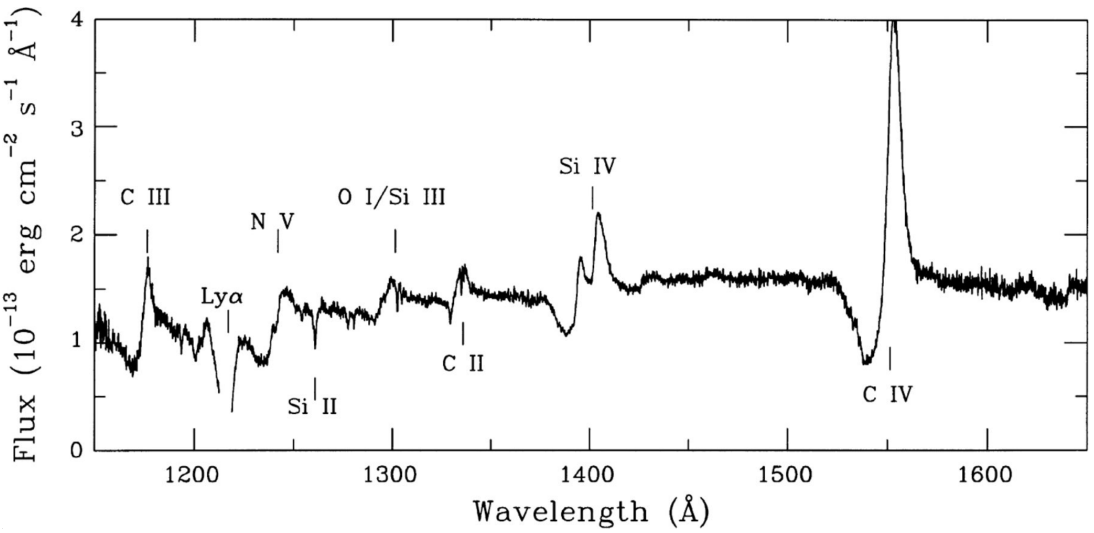

FIGURE 1.16: Ultraviolet spectrum NL variable *BZ Cam*. Strong P-cygni profiles in resonant transitions indicate the presence of a wind driven outflow. Adapted from Prinja et al. (2000).

Figure. 1.15). The expanding gas can scatter the light from all directions into the line of sight, forming an emission line centred at the rest wavelength of the transition. However, the component of the outflow in front of the star – all of which is moving towards the observer – will scatter part of this light out of the line of sight, producing a blue-shifted absorption component. The net effect is what we call a classic P-Cygni line profile. Some non-eclipsing NLs and outbursting DNe exhibit such profiles in their UV resonance lines (e.g. Heap et al., 1978; Greenstein & Oke, 1982; Cordova & Mason, 1982, see also Figure 1.16).

However, in disc-accreting systems, the spectral line profiles formed in the wind will exhibit a strong inclination dependence, even if the wind itself has spherical geometry, provided the disc is the main continuum source (e.g. Drew, 1987; Mauche & Raymond, 1987; Knigge et al., 1995; Matthews et al., 2015). In this situation, the emission component will be suppressed in face-on systems, while the contrary is true for extreme edge-on inclinations (see Figure 1.17; Mauche & Raymond, 1987). The basic picture emerging from modeling these signatures in CVs is that of a moderately bipolar outflow that carries away about 10% of the accreted material (e.g. Long & Knigge, 2002).

The most commonly observed wind-formed lines in CVs are the usual UV resonance lines (Section 1.4.8). However, similar features have also been seen in other wavebands, such as the extreme UV (Mauche, 2004a). Disc winds may also account for the single-peaked emission lines typically observed in the optical spectra of high-state CVs (e.g. Murray & Chiang, 1996). Indeed, in high-inclination systems, these single-peaked lines tend to be at most weakly eclipsed, suggesting that they are formed in a volume larger than the secondary star (Baptista et al., 2000). In a handful of cases, P-Cygni profiles have also been observed in the optical spectra of CVs (Patterson et al., 1996; Ringwald

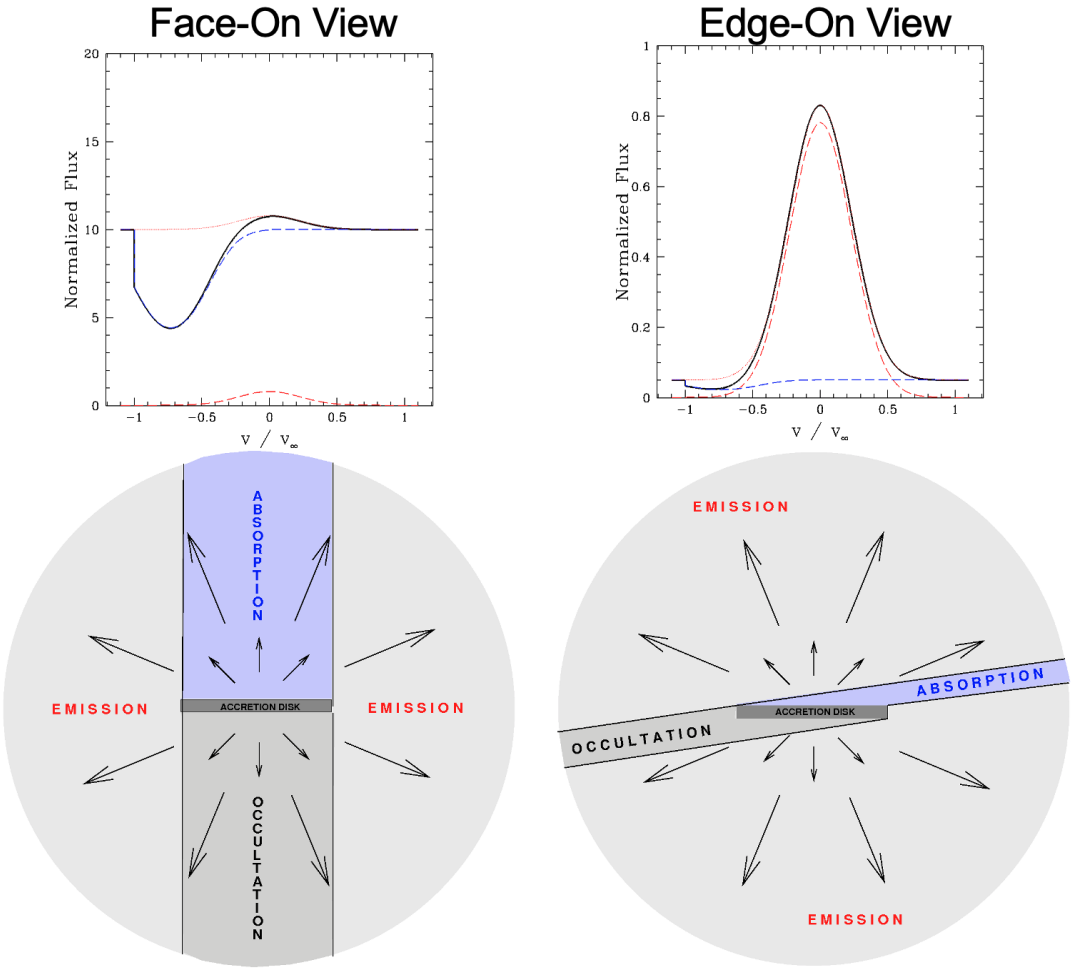

FIGURE 1.17: Same as Figure 1.15 but for an accreting system. In this geometry, even an spherical outflow will have dependencies with the line of sight. While the face-on observer will see mainly blue-shifted absorption, the edge-on observer would see emission dominated profile. Credit: Knigge (1995).

& Naylor, 1998; Kafka & Honeycutt, 2004), which requires high densities and therefore high mass-loss rates.

In XRBs, the SED is dominated by X-ray emission, which results in a slightly different picture. In these systems, the most common signature of disc winds are blue-shifted absorption lines in the X-ray spectrum. The detection of these signatures is biased to systems with high inclination and detectable only during the soft state, when the jet is quenched. This anti-correlation between X-ray disk winds and radio-emitting jets is not well understood. One possibility is that both types of outflows are magnetically driven (e.g. Blandford & Payne, 1982; Miller et al., 2012; Scepi et al., 2019), but require different magnetic field geometries. If state transitions are associated with a reconfiguration of the global magnetic field structure, this would account for the apparent link between accretion state and outflow type (e.g. Neilsen & Lee, 2009). Alternatively, the disappearance of wind-formed X-ray absorption lines could be an observational selection effect, e.g. a thermal disk wind may be present, but simply become overionized in

the hard state (Díaz Trigo & Boirin, 2016). Indeed, state-of-art radiation-hydrodynamic simulations of BHXRBs predict that thermally driven winds *should* exist in the hard state of XRBs – and actually carry 20 times more kinetic energy than in the soft state – but are harder to detect observationally (Higginbottom et al., 2020).

Against this background, the recent discovery of P-Cygni profiles in the Balmer and He I lines of some LMXRBs came as a surprise (Muñoz-Darias et al., 2016, 2019). The formation of these *optical* disk wind signatures requires dense, massive and relatively cold outflows. The implied velocities are comparable to those inferred from the X-ray absorption lines, although optical absorption features have so far only been observed in the hard state. In addition to this, the recent detection of wind signatures also in the NIR Paschen series during the soft state suggests the presence of a steady cold outflow during the entire outburst, with the wind ionisation state increasing slightly from the hard to the soft state (Sánchez-Sierras & Muñoz-Darias, 2020). Steady disk winds like this have been invoked to account for the high angular momentum losses inferred from light curve modelling of these transients (Tetarenko et al., 2018b). Overall, our current picture of disc winds in XRBs is rather complex and quite far from being understood theoretically.

1.6.3.2 Bow-shocks

When an outflow propagates into a medium with a velocity that exceeds the speed of sound of that medium, it produces a shock. Such shocks are commonly observed in supernova remnants and pre-main-sequence stars, and they can also be produced by the strong jets emerging from powerful AGNs (e.g. Schwartz et al., 1983; Carilli et al., 1994). In XRBs, collimated jets interacting with the ISM can form arc-like structures, which have been detected in a handful of sources at radio (Gallo et al., 2005; Tetarenko et al., 2018a, 2020a) and optical wavelengths (Gallo et al., 2005; Russell et al., 2007). Stellar winds from massive stars moving supersonically with respect to the ISM can also produce bow shock structures, as seen, for example, around the O-star ζ *Ophiuchi* (Gull & Sofia, 1979). Until recently, only one CV exhibiting a wind driven bow-shock was known, the NL variable *BZ Cam* (Hollis et al., 1992). There are still only a handful of examples (e.g. Hollis et al., 1992; Hernández Santisteban et al., 2019a), one of which is the system explored in Chapter 2, V341 Ara.

In general, the collision of a supersonic wind with the surrounding medium will lead to an interaction region, known as a forward shock, that propagates through the medium while compressing it. After travelling a distance R_1 from its launching position, the high-speed wind encounters the shocked medium. In the resulting interaction, the kinetic energy of the wind is thermalised. This heats the wind material and produces a reverse shock (Weaver et al., 1977). The forward shock is radiative and slow, whereas

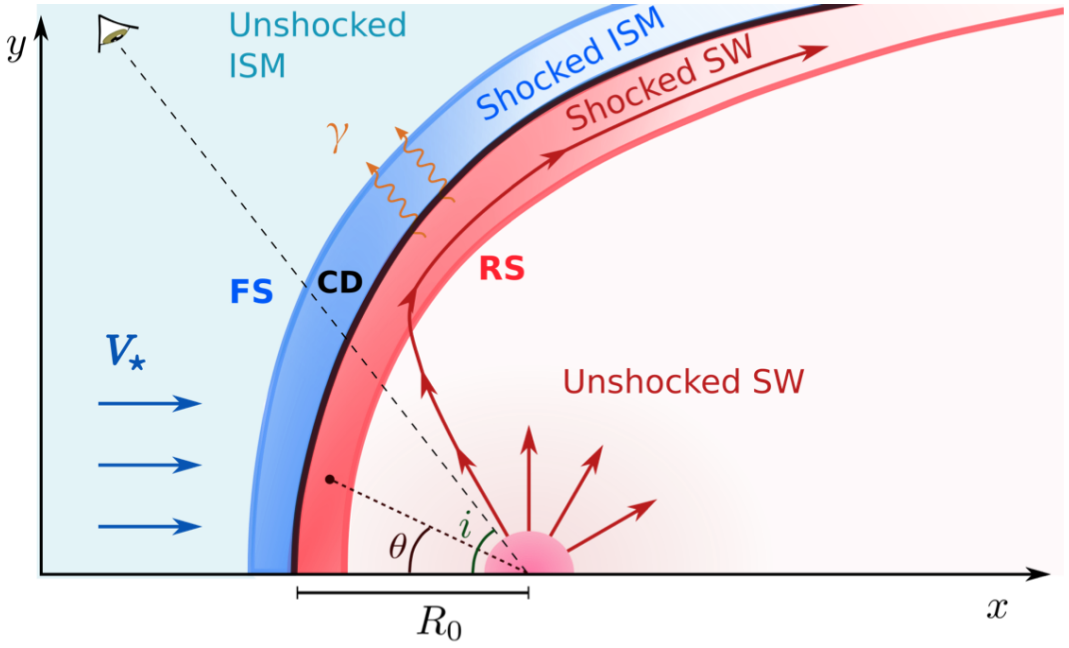

FIGURE 1.18: Sketch (not to scale) of a bow-shock created from an spherical wind illustrating the different components. In the star rest frame, the ISM moves with a velocity $V_\star$. The position of the forward shock (FS), contact discontinuity (CD), and reverse shock (RS) are indicated with solid lines. The arrows represent the stellar wind. When the wind enter the shocked region it is accelerated (solid line with arrows), if the acceleration is strong enough it produces non-thermal emission (γ). Credit: del Palacio et al. (2018).

the reverse shock is adiabatic and fast. Between these two shocks lies the so-called contact discontinuity, a surface that separates the shocked wind from the shocked medium; here, the net flux of particles is zero (see Figure 1.18). Ionising photons produced in the shocked wind immediately behind the radiative shock can photoionise the radiative forward shock, thereby producing an H II region (the recombination zone in Figure. 1.19).

The release of energy in these bow-shocks allows us to determine the mechanical power of the outflow (e.g. Weaver et al., 1977; Dopita, 1977). In addition, the size and morphology of bow-shocks are governed by the properties of the local ISM, the mass carried by the outflow and the relative velocities of the two flows (Weaver et al., 1977). Hence, with prior knowledge of the proper motion and the ambient ISM, bow-shocks can be used to independently constrain the properties of the outflow, such as the mass loss rate (e.g. Kobulnicky et al., 2018).

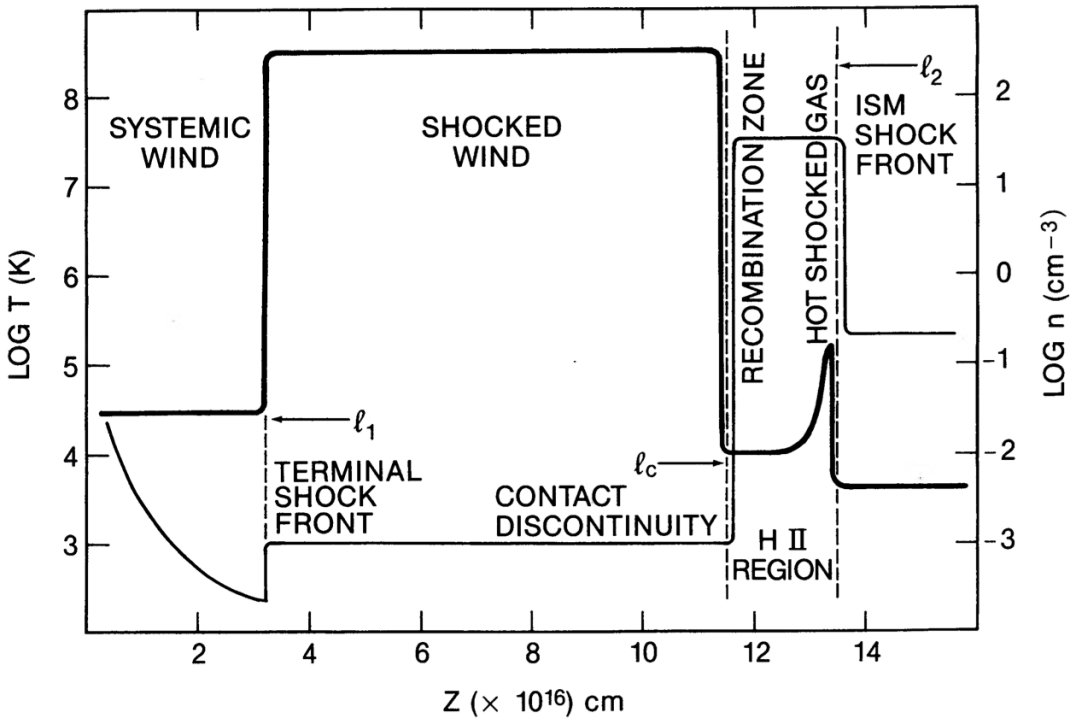

FIGURE 1.19: Schematic along the axis of symmetry of the idealised density (thin line) and temperature (thick line) profiles of the bow-shock nebula associated with the CV *BZ Cam*. The shapes of the profiles are merely illustrative and not well determined. The medium between l_1 and l_2 is assumed to be isobaric (i.e. $n \times T = 3.5 \times 10^5\,\mathrm{K\,cm^{-3}}$). Credit: Hollis et al. (1992).

1.7 This thesis

In this thesis, I present multi-wavelength studies of two accreting compact binaries. In the current chapter, I have provided a brief overview of the most relevant theoretical and observational features of accreting compact binaries and related outflows. The rest of the thesis is structured as follows.

In Chapter 2, I present a detailed study of the recently identified NL *V341 Ara*, one of the closest and brightest objects of its class. This unique system is surrounded by a bright emission nebula, likely the remnant of a recent nova eruption. Embedded within this nebula is a prominent bow-shock, where the system's accretion disc wind runs into its own nova shell, making this system the second example of a CV with a wind-driven bow shock (after *BZ Cam*, Section 1.6.3.2). In order to establish its fundamental properties, I present the first comprehensive multi-wavelength study of the system.

The remaining work described in this thesis concerns the recently discovered transient LMXB *Swift J1858.6-0814*. More specifically, it is based on a major observational campaign targeting this system, which I initiated and still lead. This campaign was motivated by the search for wind signatures in the ultraviolet (UV) region and led by

the award of a Hubble Space Telescope (HST) Director's Discretionary Program. It ultimately covered everything from X-rays to radio frequencies, based on data gathered by both ground-based and spaced-based observatories (including NuSTAR, NICER, VLA, MeerKAT, VLT/X-Shooter, VLT/HAWK-I, Gemini/Flamingos2 and GTC/Osiris).

First, in Chapter 3, I provide an overview of the campaign and a look at the multi-wavelength behaviour of the source during the campaign. Then, in Chapter 4, I present the first results coming from the far-UV, time-resolved spectroscopy obtained with HST. Lastly, in Chapter 5, I discuss the intrinsic luminosity and evolutionary stage of the system, based on the data gathered during the campaign.

Finally, in Chapter 6, I present my overall conclusions and highlight promising research directions for future work.

Chapter 2

Accretion and disc winds in the nova-like cataclysmic variable star *V341 Ara*.

2.1 Introduction

As discussed in 1.4.4, NLs are perhaps the only astrophysical systems where standard, steady-state, non-relativistic accretion disc theory (Shakura & Sunyaev, 1973) should apply without modification. This makes them extremely useful laboratories for testing the theory.

The 10^{th} magnitude variable star *V341 Ara* was first catalogued by Leavitt & Pickering (1907). It was then (mis-) classified by Hoffmeister (1956) as a Type II Cepheid, based on the presence of a $P \simeq 12$ d period in their light curve of the system. In spite of *V341 Ara*'s extremely blue colour, this mis-classification stood for more than 60 years, with subsequent photometric studies reporting similar, though not identical periodic variability ($P \simeq 11$ d, ESA 1997; $P \simeq 14$ d, Berdnikov & Szabados 1998).

In fact, *V341 Ara* is one of the brightest CVs known, though it was not identified as such until recently. This identification was made by Frew (2008, hereafter F08), based on a combination of spectroscopic signatures, flickering, blue colour and its identification with a ROSAT X-ray source [1]. F08's primary science objective was actually the identification of new planetary nebulae (PNe). Their study of *V341 Ara* was prompted by its association with a previously uncatalogued large ($8' \times 6'$) Hα nebula. More recently, Bond & Miszalski (2018, hereafter B18) confirmed the NL classification and carried

[1] Samus et al. (2007), as well as Kiraga (2012), independently proposed the classification of *V341 Ara* as a CV, based on the X-ray match.

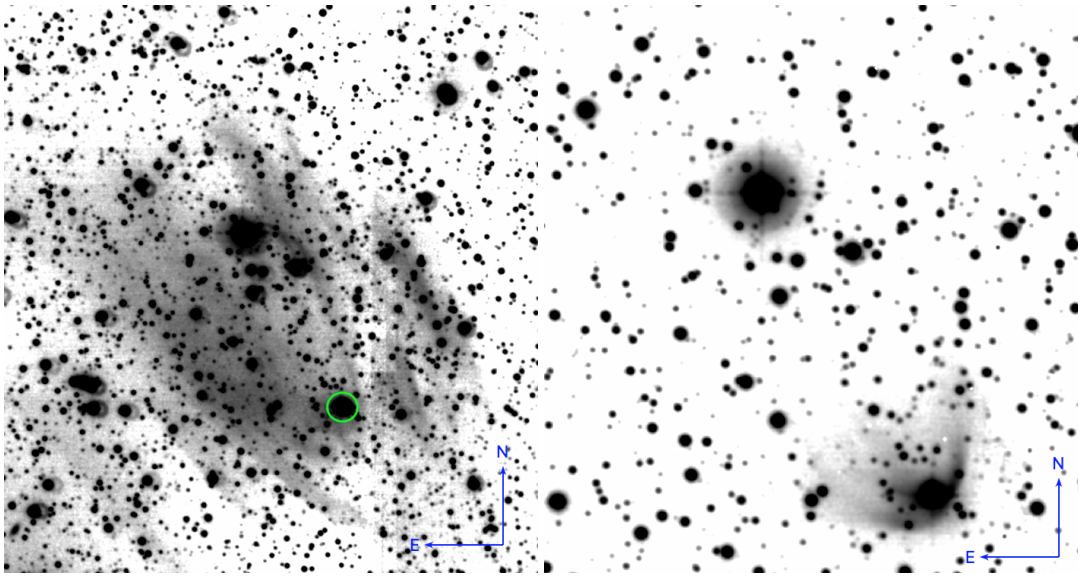

FIGURE 2.1: ESO/WFI narrow band images of the field around *V341 Ara*. Left: Hα illustrating the emission nebula in the vicinity of the nova-like variable, the star is marked with a green circle. Note the cosmetic defects North-West from the source due to gaps between different chips in the image. Right: Same field, but with 2x zoom, in [OIII] illustrating the bowshock around *V341 Ara*. Images were processed using THELI software (Erben et al., 2005; Schirmer, 2013).

out the first radial velocity study for the system. They reported an orbital period of $P_{orb} = 3.65$ h, consistent with the bulk of the NL population.

NLs with periods in the range 3 h $\lesssim P_{orb} \lesssim$ 4 h represent a critical evolutionary phase. The observed CV population exhibits a well-known "period gap" between $P_{orb} \simeq 2-$ h and $P_{orb} \simeq 3-$ h. Individual CVs are thought to approach the upper edge of the gap from above (i.e. longer periods), but to evolve *through* the gap as detached systems. NLs like *V341 Ara* are therefore systems whose donors will soon lose contact with the Roche lobe, possibly as they make the transition from partially radiative to fully convective stars (see Section 1.1.3; or Knigge et al. 2011 for a complete review). Many, if not all, of these systems also share at least some of the peculiar observational characteristics collectively known as the "SW Sex syndrome" (Dhillon, 1990; Thorstensen et al., 1991; Rodríguez-Gil et al., 2007; Schmidtobreick et al., 2012; Dhillon et al., 2013).

Based on its Hα luminosity, F08 estimated the mass of the nebula around *V341 Ara* as $M_{H\alpha} \simeq 5 \times 10^{-3}$ M$_\odot$, roughly 100$\times$ less massive than a typical PN. Both F08 and and B18 suggested that the nebula may therefore be an old nova remnant associated with *V341 Ara* itself. Intriguingly, the star is located $\simeq 2'$ from the center of the Hα nebula, which might be due to its high proper motion if the nova eruption occurred $\simeq$1000 yrs ago.

However, perhaps the most important and unusual feature of *V341 Ara* is that it lies near the apex of an impressive parabolic bow-shock, thought to be due to the interaction of its accretion disc wind with the ISM (F08, B18). This bow-shock is seen in both

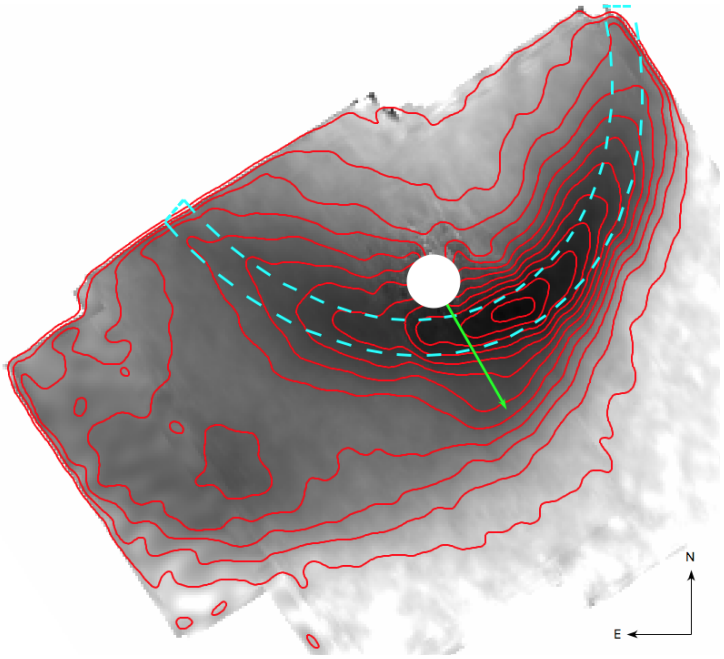

FIGURE 2.2:
λ5007Å emission line]Combined image with background subtracted of the numerically integrated [OIII] λ5007Å emission line from the integral field spectroscopy. The 4 arcsecond diameter circle is centered in the position of the source, while the green arrow represent the direction of the proper motion of the star derived from *Gaia DR2*. The dashed cyan paraboloid symmetry axis is aligned with the proper motion of the star and has a thickness of 3 arcseconds. Contours with equal flux density are plotted in red.

the [OIII] and [NII] nebular emission lines and is located within the larger scale Hα nebula (see fig.2.1). Only two other CVs surrounded by wind-driven bow-shocks are known: *BZ Cam* (Hollis et al., 1992) and *V1838 Aql* (Hernández Santisteban et al., 2019b) [2]. These objects are critical for testing disc wind models for CVs (e.g. Knigge et al., 1997; Long & Knigge, 2002; Matthews et al., 2015), since the observed shock properties can provide a model-independent mass-loss rate estimate (e.g. Kobulnicky et al. 2018).

In this Chapter, I present the first comprehensive multi-wavelength study of *V341 Ara* in order to establish the fundamental properties of the system. In Section 2.2, I introduce the data sets used in this study. Section 2.3 presents the analysis of the data, with Tables 2.3 and 2.4 in this section collecting some of our main results. Finally, in Section 2.4, I discuss the unique nature of this system, given all of the observational evidence available that has been collected to date. In Section 2.5 the main results are summarised.

[2] A bow-shock is also present around the NL IPHASX J210204.7+471015, but this is probably due to the interaction of this system's nova shell with the ISM (Guerrero et al., 2018).

2.2 Data Sets

For the present study, I have collected multi-wavelength data covering the radio, infrared, optical, near-ultraviolet and X-ray bands. This includes multiple sets of time-resolved optical photometry and time-resolved optical spectroscopy. It also includes 2-D optical spectroscopy covering the nebular emission around *V341 Ara*. In the remainder of this section, I briefly describe these data sets. A summary of the observations is provided in Tables 2.1 and 2.2 for the spectroscopic and photometric time-series respectively. For reference, Fig. 2.4 shows the epochs at which the various data sets were obtained, superposed on our long-term optical light curves.

2.2.1 Time-resolved photometry

2.2.1.1 ASAS-SN

The All-Sky Automated Survey for Supernovae (*ASAS-SN*) aims to provide near-continuous all-sky optical monitoring. It reaches a depth of $V \simeq 17$ and provides 3x90 s sequential exposures each night for the entire observable sky (Kochanek et al., 2017). The survey uses five stations, each of which consists of four 14 cm aperture Nikon telephoto lenses. The observations are made in the V-band (two stations) or g-band (three stations). *V341 Ara* has been monitored by *ASAS-SN* since March 2016. Here, I use all 893 g-band and 616 V-band measurement that were gathered prior to October 2019.

2.2.1.2 KELT

The Kilo-degree Extremely Little Telescope (*KELT*) project (Pepper et al., 2007, 2018) is a survey designed primarily for the detection of planetary transits around bright stars. Here, I use data from *KELT-South*, a 4-cm telescope that monitors the southern sky with a spatial resolution of $23''$ per pixel and a cadence of about 20-30 minutes (for airmass < 1.5). In order to maximize sensitivity, *KELT* does not employ filters, but the response function of the system peaks around 6000Å (Pepper et al., 2012). *KELT* gathered data for *V341 Ara* from 2013 to 2018, providing a a total of 5840 photometric measurements across this 6-year period.

2.2.1.3 TESS

The *Transiting Exoplanet Survey Satellite* (*TESS*, Ricker et al., 2015) is a space-based telescope launched in 2018. Like *KELT*, *TESS*'s primary mission is to detect transiting exoplanets around nearby stars. It provides optical images with an effective spatial resolution of $21''$, covering a bandpass of $\simeq 0.6 - 1\mu$m.

TESS monitors the sky in sectors, with each sector being observed continuously for 27 days. Full-frame images are provided at a cadence of 30 minutes, but 10×10 pixel postage stamps around a set of pre-selected targets are downloaded at the optimum 2 minute cadence. The data for these fortunate targets is reduced by the Science Processing Operations Center (SPOC) pipeline (Jenkins et al., 2016), during this process a pixel-by-pixel correction is applied, the optimal photometric aperture along with an estimation of the contamination by nearby stars is calculated before extracting the light curves. Barycentered light curves ("LCF files") are available from the *Mikulski Archive for Space Telescopes*[3] *(MAST)*.

V341 Ara was one of the pre-selected targets in *TESS* Sector 12. As such, it was observed with 2-minute cadence from 2019 May 21 to 2019 June 19.

2.2.2 Time-resolved 1D and 2D spectroscopy

2.2.2.1 CTIO: RC Spectrograph

B18 obtained medium resolution time-resolved spectroscopic observations of *V341 Ara* with the *RC Spectrograph* on the *SMARTS* 1.5 m telescope at the *Cerro Tololo Inter-american Observatory (CTIO)*. All of their data were collected between April and July of 2006, but most of their observations are missing from the CTIO archive. In our long-term radial velocity study, I therefore directly adopt the 59 measurements provided by B18 for the centroid of the Hα emission line core in their red exposures.

2.2.2.2 CTIO: Chiron

Chiron (Tokovinin et al., 2013) is a high dispersion bench-mounted echelle spectrograph on the *SMARTS 1.5m telescope* at *CTIO*. We used *Chiron* in fiber mode, covering the 4083-8901 Å region in 75 orders at a resolution of $R = \lambda/\Delta\lambda \simeq 27800$. We obtained a total of 26 exposures on two nights in 2018. Three exposures were taken on 25 March 2018, the remainder on 12 May 2018. All spectra were extracted and reduced using the CH_REDUCE code (Walter 2017[4]).

2.2.2.3 SAAO: SpUpNIC

SpUpNIC (Crause et al., 2016) is a low- to medium-resolution long-slit spectrograph mounted on the *1.9-m Radcliffe telescope* at the *South African Astronomical Observatory (SAAO)*. We used the *gr4* grating for our observations, which provides a wavelength

[3] http://archive.stsci.edu/tess/

[4] http://www.astro.sunysb.edu/fwalter/SMARTS/NovaAtlas/ch_reduce/ch_reduce.html

coverage of $\lambda\lambda 3750 - 5100$ Å with a dispersion of $\simeq 0.6$ Å/pix. We obtained 12 exposures covering slightly less than 1 hr on each of the nights of 2017 March 12 and 16. One additional exposure each was obtained on the nights of 2017 March 15 and 17. The spectra were reduced using standard IRAF routines. Cosmic ray rejection was performed with LACOSMIC (van Dokkum, 2001).

2.2.2.4 SAOO: SALT/HRS

The *High Resolution Spectrograph* (*HRS*; Crause et al., 2014) is a double-beam, fiber-feed echelle spectrograph mounted on the *Southern African Large Telescope (SALT)*. We used the low resolution mode of HRS to obtain spectra covering the range $\lambda\lambda 3800 - 8900$Å with a resolving power of $R \simeq 15000$. Our observations were carried out on four nights between 2018 April 15 and 2018 April 21, with 5 exposures being taken on each of these nights. Data reduction was performed with the PYSALT pipeline.

2.2.2.5 SSO: WiFeS

The *Wide Field Spectrograph* (*WiFeS*, Dopita et al., 2007) is a double-beam, image-slicing integral field unit (IFU) mounted on the Australian National University's 2.3 m telescope at *Siding Spring Observatory (SSO)*. It provides spectral images across a contiguous $25'' \times 38''$ field of view, using $25 \times 1''$ "slitlets" along the short axis and $0.5''$/pixel spatial sampling along the long axis. We used *WiFeS* in the B7000 (blue arm) and R7000 (red arm) configurations, which provides a resolution of $R \simeq 7000$ across the full wavelength range $\lambda\lambda 5300 - 7100$ Å. Our observations were obtained on the night of 2018 April 26, during which the target field was monitored for 4.5 hours without interruption, using 300 s integrations. In order to fully cover the bow-shock surrounding *V341 Ara*, I used several different pointings to cover a total field of approximately $50'' \times 40''$. The shifts and rotations between pointings were typically $20''$ and 90°, respectively.

Since *WiFeS* provides *spatially-resolved* spectroscopy, I used this data set for two distinct purposes. First, I extracted time-resolved 1-D spectroscopy for the central point source using a 3×3 spaxel aperture centered on the peak of the continuum count rate distribution. Second, I constructed narrow-band images by aligning all pointings to the central source and then combining them. I used a resampling factor of 5 for this mosaic, yielding a plate scale of $0.2''$ per spaxel for the final images. In order to create pure emission line images, I created narrow-band images centered on specific transitions and then subtracted a linear fit to the local continuum in each spaxel. Given that seeing was better than $0.9''$ throughout our observations, these are the highest-resolution, unsaturated images of *V341 Ara* and its bow-shock to date. Figure 2.2 shows the resulting emission line image for the [O III] $\lambda 5007$ Å transition.

2.2.3 *Swift* X-ray and ultraviolet observations

We observed *V341 Ara* twice with the *Neil Gehrels Swift Observatory* (Burrows et al., 2005), on 2018 July 04 and 2019 February 28, for a total exposure time of 4.6 ks. We used standard *Swift/XRT* routines (XRTPIPELINE 0.13.4 in *heasoft 6.25*) to reduce the XRT data, extract counts from a circular aperture of 5″ centered on the source and construct a spectrum covering the 0.3-10 keV range for each of the two epochs. There was no significant variability in the X-ray data within or between the two epochs.

We also used *Swift* to obtain near-ultraviolet (NUV) imaging observations with the *UV/Optical Telescope* (*UVOT Roming et al., 2005)*. In July 2018, we imaged the system for 326 s with the UVW1 filter ($\lambda_{eff} \simeq 2590$ Å), while in February 2019, we used the UWM2 filter ($\lambda_{eff} \simeq 2230$ Å) for a total of 680 s. Since *V341 Ara* was saturated in all of the *UVOT* images, we used readout-streak photometry (Page et al., 2013) to estimate source fluxes in the UVW1 and UVM2 bands. The scatter in each band was consistent with being due to photometric errors, so we combined the exposures in each band to produce a single flux estimate for each filter.

Finally, in February 2019, we also obtained a total of 2.2 ks of NUV spectroscopy using the *Swift/UVOT* UV grism, which covers the wavelength range $\lambda\lambda 1800 - 5200$ Å at a resolution of $R \simeq 150$. The spectroscopic data were reduced using the *Swift* UVOT Grism UVOTPY package (version 2.4, Kuin 2014, an implementation of the calibration from Kuin et al. 2015). The combined 1-D spectrum was corrected for a systematic wavelength shift by ensuring that the center of the Mg II emission line lies close to 2800 Å, its expected position. Since the detector sensitivity below 2000 Å is decreasing more rapidly than at longer wavelengths, the flux calibration for $\lambda \lesssim 2000$ Å is currently unreliable. We therefore removed this part of the spectrum.

2.2.4 *MeerKAT* radio observations

MeerKAT (Jonas, 2009) is a radio telescope consisting of 64×13.5 m antennas located in the Karoo region of South Africa. The field containing *V341 Ara* was observed with *MeerKAT* at a central frequency of 1.284 GHz on 2019 March 29 as part of the *ThunderKAT* Large Survey Project (Fender et al., 2017). The full bandwidth of 856 MHz was split into 4096 channels, visibilities were recorded every 8 seconds, and 60 of the *MeerKAT* antennae were utilised. The Seyfert 2 galaxy *J1939-6342* was used as a bandpass and flux calibrator. The total integration time on *V341 Ara* was approximately 120 mins. The data were flagged using AOFLAGGER version 2.9.0 (Offringa, 2010) to remove radio frequency interference, averaged by a factor of 8 in frequency and then calibrated using standard procedures in CASA version 5.1.1 (McMullin et al., 2007). The calibrated data was imaged using the multi-facet-based radio imaging package

TABLE 2.1: Spectroscopic observing log

Telescope	Instrument	Grating	$R = \lambda/\Delta\lambda$	t_{exp}	N_{exp}
ANU	WiFeS	B7000/R7000	7000	300	41
SALT	HRS	LR	15000	1500	4
SAAO	SpUpNIC	g4	2500	600	26
SMARTS 1.5	Chiron	-	27800	600	26
SMARTS 1.5	RC Spectrograph	47/Ib	3000	300	59*
Swift	UVOT	UV	150	275	8

* Taken from B18

TABLE 2.2: Photometric observing log

Telescope	Filter	t_{exp}	N_{exp}
ASAS-SN	V	90	616
ASAS-SN	g	90	893
KELT	White light	150	5934
TESS	White light	120	19104

DDFACET (Tasse et al., 2018), with Briggs weighting, a robustness parameter of R=-0.5 and the SSD deconvolution algorithm. No self-calibration was implemented. Flux measurements and source-fitting were executed using PyBDSF [5] and noise levels were measured within the local area surrounding the source. The restoring beam had a size of 5.87×4.63 arcsecond^2.

Some CVs are strong radio emitters (see Coppejans & Knigge, 2020, for a review). Unfortunately, *V341 Ara* was not detected in these observations, unlike some other southern NLs (Hewitt et al., 2020). The corresponding 3σ flux limit is 30 μJy beam^{-1}.

2.2.5 Supplementary photometric data

In order to characterise the overall spectral energy distribution of *V341 Ara*, I have collated additional photometric measurements from the following sources: SkyMapper DR1 (optical: uvgriz; Wolf et al., 2018), APASS (optical: BV+gri; Henden et al., 2016), Gaia DR2 (optical: G+B_p+R_p; Gaia Collaboration et al., 2018), 2MASS (near-infrared: JHK_s; Skrutskie et al., 2006), VISTA VHS DR4 (JK_s; McMahon et al., 2019), WISE/ALLWISE (mid-infrared: W1+W2+W3+W4; Cutri & et al., 2014).

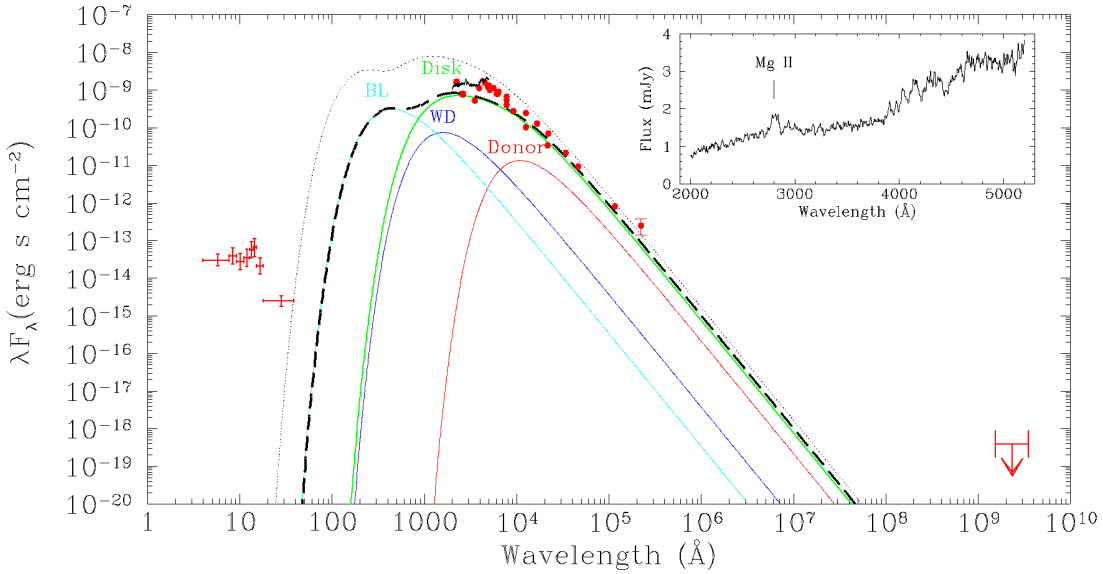

FIGURE 2.3: Spectral energy distribution of *V341 Ara* based on archival broad band photometry (Sec. 2.2.5), *Swift* and *MeerKAT* data sets (Sections 2.2.3 and 2.2.4 respectively). The inset is a zoom into the NUV spectroscopy obtained with *Swift/UVOT*. These data sets were not obtained simultaneously, so the photometric scatter is due to the intrinsic variability of the source. The different components of the system with the estimated parameters from Knigge, Baraffe, & Patterson (2011) are overlaid on top of the data for reference. Dashed black curve is the sum of the system components accreting at 10^{-9} $M_{\odot}yr^{-1}$ (green line), while dotted curve is the same but at higher accretion rate (10^{-8} $M_{\odot}yr^{-1}$).

2.3 Analysis and Results

2.3.1 Spectral energy distribution: luminosity and accretion rate

Figure 2.3 shows the panchromatic SED of *V341 Ara*, based on the data sets described in Sections 2.2.3, 2.2.4 and 2.2.5. These data sets were not obtained simultaneously, so the photometric scatter in Figure 2.3 is consistent with the observed variability of the source. As is already clear from Figures 2.4 and 2.7, *V341 Ara* exhibits significant super-orbital variability in the optical (see Section 2.3.2 for details).

To provide context and guide the eye, I also show in Figure 2.3 a simple model SED that is the sum of four components: (i) a geometrically thin, optically thick accretion disc; (ii) an optically thick boundary layer (BL); (iii) an accretion-heated WD; (iv) a donor star. The inclination towards *V341 Ara* is not known, but its absorption line dominated optical spectrum suggest a relatively face-on viewing angle (c.f. Beuermann & Thomas, 1990; Beuermann et al., 1992; Matthews et al., 2015); I therefore adopt $i \simeq 30^{\circ}$ in our SED model.

[5] https://www.astron.nl/citt/pybdsf/

Most of the remaining system parameters were taken directly from the best-fit CV evolution sequence provided by Knigge, Baraffe, & Patterson (2011, hereafter KBP11). Specifically, I adopted a mass-transfer rate of $\dot{M} \simeq 10^{-9}$ $M_{\odot}yr^{-1}$, a donor mass of $M_2 \simeq 0.26$ $M_{\odot}$, a donor radius of $R_2 \simeq 0.34$ $R_{\odot}$ and a donor temperature of $T_{eff,2} \simeq 3380$ K. Based on the results shown in Section 2.3.4.4 below, the WD mass was taken to be $M_{WD} = 0.5$ $M_{\odot}$. The WD temperature, $T_{WD} = 23,2000$ K and radius, $R_{WD} = 1.2 \times 10^9$ cm were estimated from accretion heating models of Townsley & Bildsten (2004) and the WD cooling models of Holberg & Bergeron (2006), respectively.

Each of the radiating components in the model (the WD, the BL, the donor and each disc annulus) is assumed to emit as a blackbody. The BL is modelled as an cylindrical strip wrapped around the equator of the WD that generates half of the accretion luminosity. The total vertical extent of the BL is taken to be $H_{BL} = 0.1$ R_{WD}, though only the top half of the BL is visible to the observer. With these assumptions, the effective temperature of the BL in the model is $T_{eff,BL} \simeq 83,300$ K. For comparison, Figure 2.3 also includes a second SED model that corresponds to a higher mass-transfer rate, $\dot{M} = 10^{-8}$ $M_{\odot}yr^{-1}$. The WD and BL temperatures are then $T_{\rm eff,WD} \simeq 43,300$ K and $T_{eff,BL} \simeq 150,700$ K, respectively.

Figure 2.3 shows that – with the exception of the X-ray band – *V341 Ara*'s SED is broadly consistent with these simple SED models. The excess X-ray emission compared to the model is not unusual for a NL variable (e.g. Pratt et al., 2004) and will be discussed further in Section 2.3.5. Thus, based on its SED, *V341 Ara* appears to be a normal NL variable, with system parameters typical for its orbital period. In particular, its accretion rate is likely between 10^{-9} $M_{\odot}yr^{-1}$ and 10^{-8} $M_{\odot}yr^{-1}$.

2.3.2 Optical light curves: large-amplitude, super-orbital, quasi-periodic variations

Figure 2.4, provides an overview on each of the last 3 observing seasons, during which all of our other data sets were taken. In this figure, the *TESS* observing window is indicated by a vertical green band, and the dates on which spectroscopic, X-ray/UV (*Swift*) and radio (*MeerKAT*) observations were carried out, are marked by vertical lines. The 2-minute cadence, 27-day *TESS* light curve is shown in Figure 2.5.

The first obvious and important point to note is that *V341 Ara*'s variability is dominated by large-amplitude – $\delta_m \simeq 0.5 - 2.0$ mag – super-orbital modulations (see also Figure 2.7). The characteristic time-scale of these oscillations – $\simeq$10-16 days – is far longer than the orbital period of $P_{orb} \simeq 3.7$ hrs (B18; also see Section 2.3.4.3). However, the amplitude and time-scale of these variations are comparable to those associated with the pulsations of Type II Cepheids, and specifically the W Vir subclass (e.g. Berdnikov & Szabados, 1998). This, in addition to the lack of statistically significant

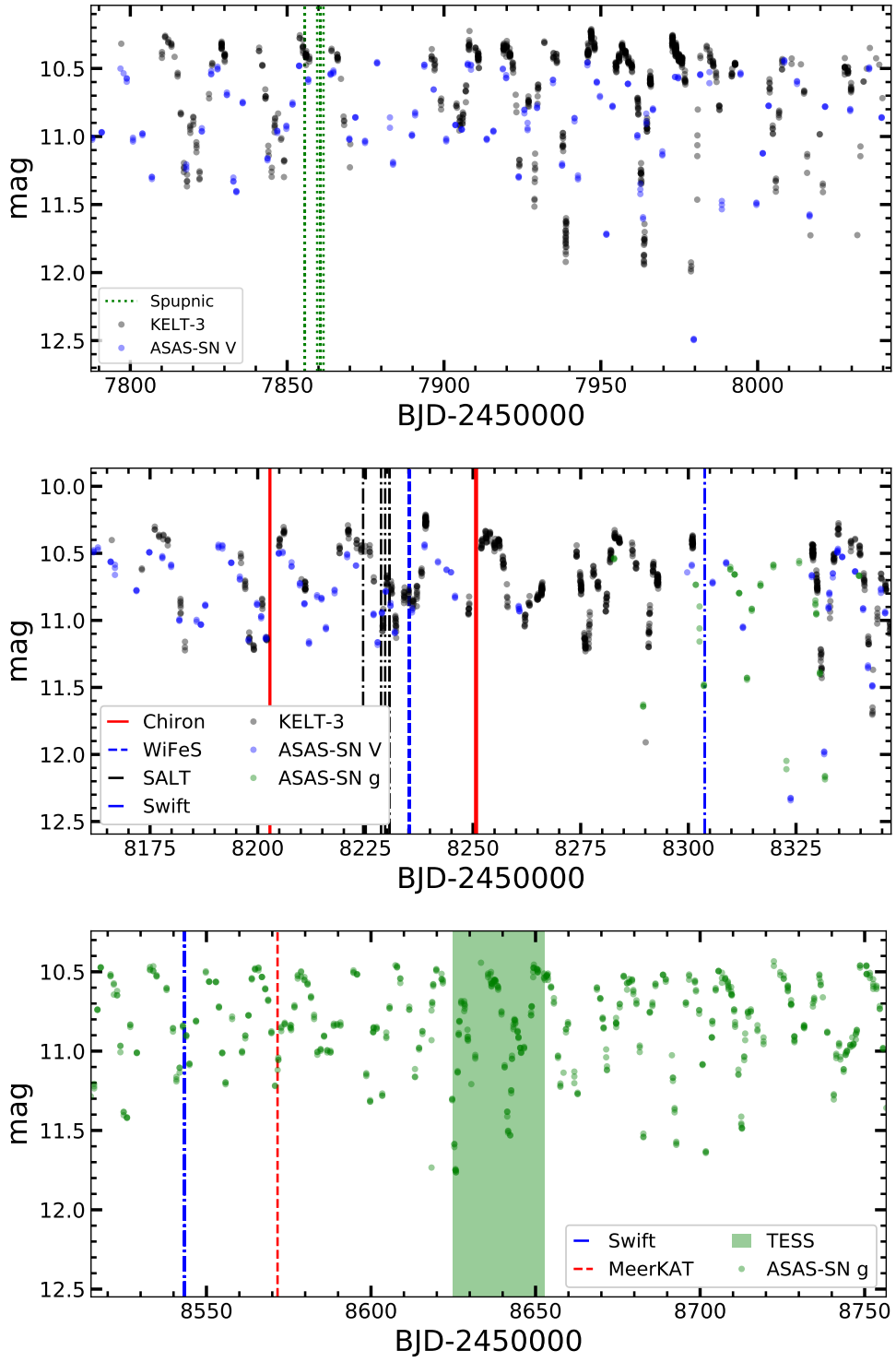

FIGURE 2.4: Long term optical light curve of the seasons when the different datasets where gathered, these are marked with vertical lines. Note I only shift the baseline of the *KELT* data, by subtracting 3 mags, to match the median magnitude of the *ASAS-SN* data. I do not make any additional attempt to place the different time series photometry on the same absolute scale.

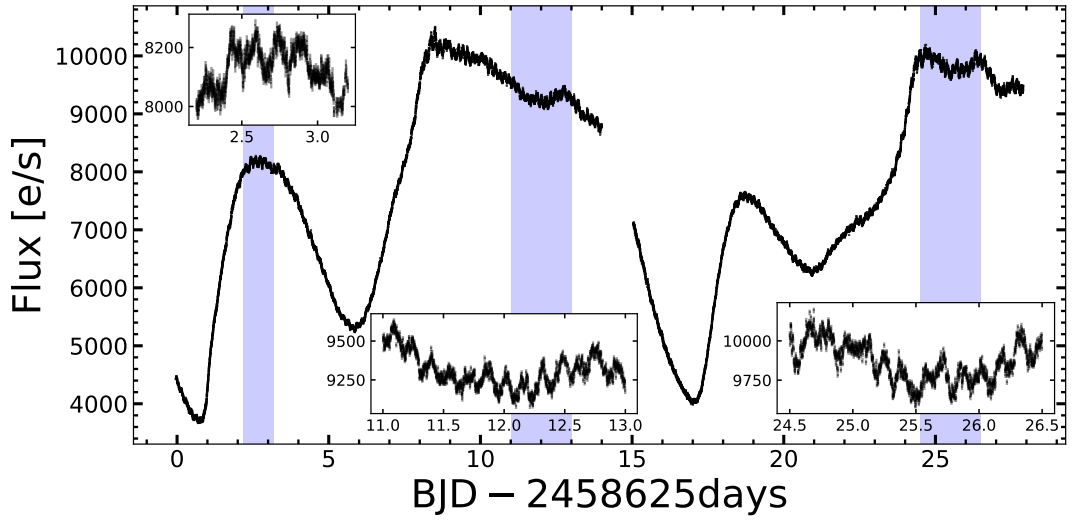

FIGURE 2.5: The *TESS* lightcurve of *V341 Ara* during sector 12 illustrate the complexity of the super-orbital modulation; insets are zooms of the overlapping shaded regions. Here, the orbital and superhump modulations are superimposed to the main signal with an amplitude roughly 3%. The $\sim$ 1 day data gap is due the perigee passage of the spacecraft while downloading the data.

power around the orbital frequency explains the long mis-classification of *V341 Ara* as a Cepheid variable.

The prevalence and quasi-periodic nature of these slow variations are apparent in Figures 2.6 and 2.7, which shows generalized Lomb-Scargle (Lomb, 1976; Scargle, 1982; Zechmeister & Kürster, 2009; VanderPlas, 2018) periodograms for each of the light curves. Every data segment produces a strong power excess in this frequency range, but the exact location of the peak frequency changes across data sets and observing seasons. The amplitude of these variations is also highly variable. For example, Figure 2.7 shows that the peak-to-peak variability level in the *KELT* Year 1 data is $\lesssim$1 mag, but in a similar-sized segment of the *KELT* Year 5 data, it reaches $>$ 1.5 mag.

To illustrate these features more clearly, Figure 2.7 shows a dynamic power spectrum I have constructed for the *KELT* data set, along with the season-by-season light curve. In calculating this power spectrum, I require each time bin to span at least $\pm$15 days and include a minimum of 20 data points; note that this will tend to smooth any sudden change in the periodic signal.

By contrast, only the high-cadence, high-S/N *TESS* data set reveals a (weak) orbital signal (see insets in Figure 2.5 and Figure 2.8). The characteristic amplitude of this signal is just $\simeq$ 1%, which suggests a relatively low (face-on) orbital inclination for *V341 Ara*, in agreement with the assumption in previous section.

Perhaps more importantly, however, the power spectrum of the *TESS* data actually exhibits *two* peaks near the orbital frequency. One of these — $f_{orb,TESS} = 6.569 \pm$

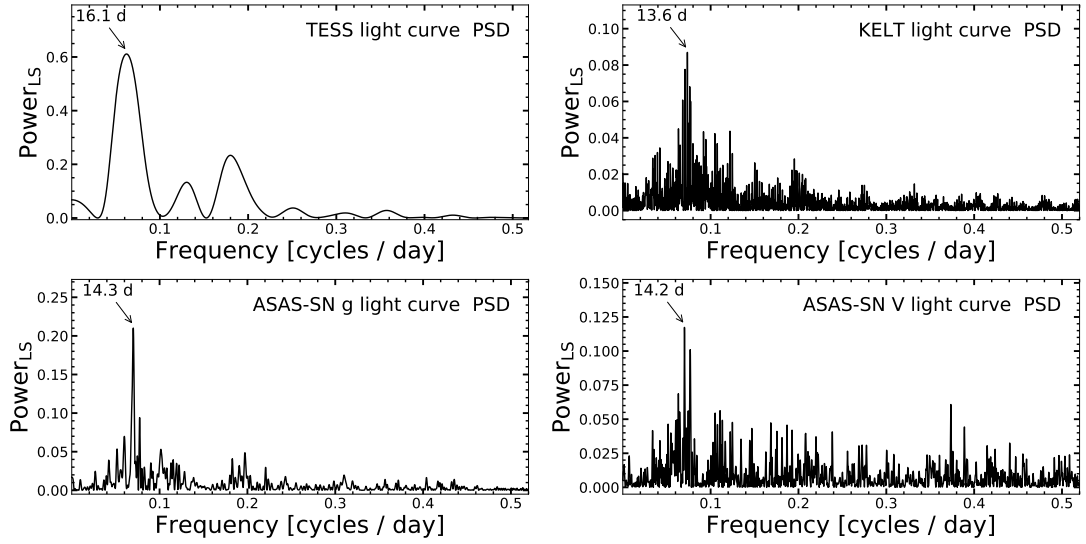

FIGURE 2.6: Low frequency generalized Lomb-Scargle power spectrum of the different light curves illustrating the super-orbital period and its variability across sessions and data sets. Note the figures are shown up to 0.55 cycles/day due to lack of statistically significant power around the orbital frequency since these frequencies are dominated by strong aliases of the super-orbital modulation in the ground-based observatories.

0.007 c/d), corresponding to $P_{orb} = 3.654 \pm 0.004$ hrs — is consistent with the orbital period obtained from our multi-year spectroscopic data (see Section 2.3.4.3). The other — $f_{SH-} = 6.628 \pm 0.006$ c/d, corresponding to $P_{SH-} = 3.621 \pm 0.003$ hrs — is roughly 1% *faster* than the orbital signal. This signal is similar to the so-called "negative superhumps" seen in the light curves of several other nova-like variables (e.g. Patterson et al., 2005). As discussed in Section 1.4.7, the negative superhump signal is thought to represent a beat between the binary orbit and the much slower, retrograde, nodal precession of a tilted accretion disc.

If the same interpretation holds for *V341 Ara*, it is tempting to associate the dominant large-amplitude $10 - 16$ day signals in the photometric data with the disc precession period itself. Is this viable? The frequency difference between f_{orb} and f_{SH-} in the *TESS* data is $\Delta f = 0.06 \pm 0.006$ c/d, which corresponds to an implied precession period of $P_{prec} = 16.4 \pm 1.6$ d. This is completely in line with the measured period of the slow photometric variations during the *TESS* observations, which was $P_{slow} \simeq 16.1$ d (see Figure 2.6).

2.3.3 Astrometry: distance and membership of the thin disc population

V341 Ara is included in Gaia DR2 (Gaia Collaboration et al., 2018). I therefore estimate its distance from the Gaia parallax, $\pi = 6.40 \pm 0.08$ m*as*, using the Bayesian approach described in Luri et al. (2018) to account for the covariance of the distance and proper motion. This yields a distance of 156 ± 2 parsecs (pc), for a prior with a length scale

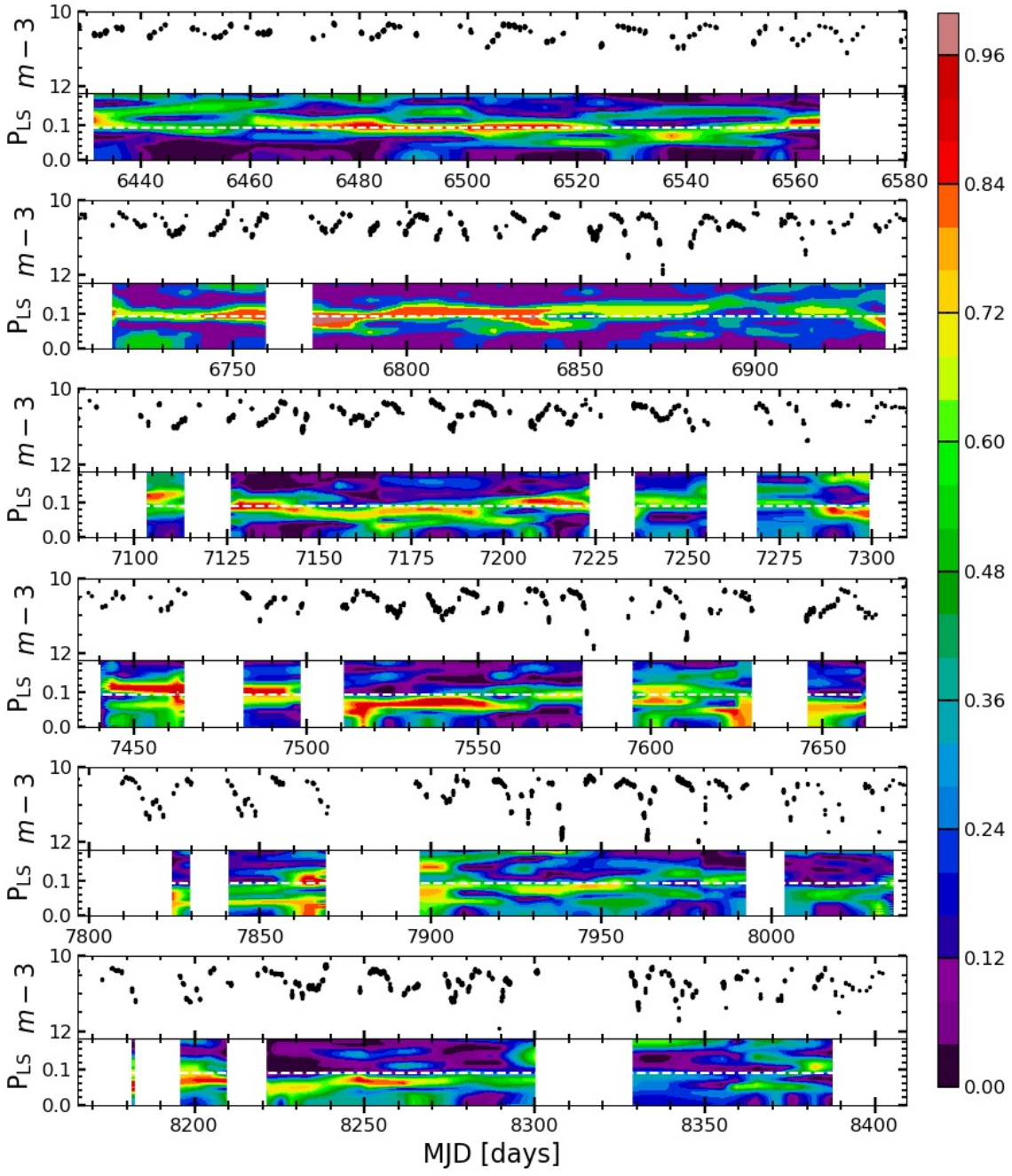

FIGURE 2.7: *KELT* light curve and dynamic power spectrum. Top panels: *KELT* instrumental magnitude - 3 vs time. Bottom panels: dynamic Lomb-Scargle power spectrum, abscissas axis represent the time in days and the frequency in cycles per day in the ordinates, the Lomb-Scargle power is represented in the colour scale. Each bin in the periodogram includes the contiguous ± 15 days with a minimum of 20 data points. The horizontal white dotted line represent the frequency with highest power in the periodogram of the whole set.

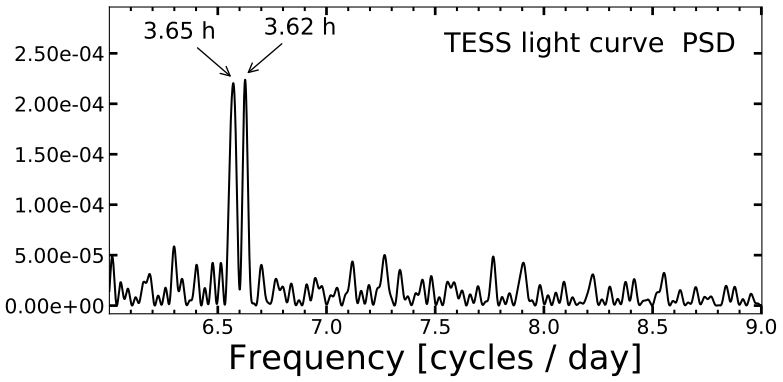

FIGURE 2.8: High frequency generalized Lomb-Scargle power spectrum of TESS light curve. The 3.65 peak is consistent with the orbital period, while the 3.62 h is consistent with the beat frequency of the super-orbital modulation with the orbital period.

of 1.5 kpc. However, given the precision of the parallax measurement, the distance estimate is highly insensitive to the prior. Based on this estimate, *V341 Ara* is the 3$^{\rm rd}$ closest non-magnetic NL.

The proper motion of *V341 Ara* provided by Gaia is $\mu_\alpha \cos\delta = -48.32 \pm 0.07$ mas yr^{-1} and $\mu_\delta = -84.91 \pm 0.08$ mas yr^{-1}. Given its distance, this corresponds to a transverse velocity of 72 ± 1 km s^{-1} .

I also checked for possible distant companions to the *V341 Ara* binary system by searching for Gaia sources within 1° of its position that also have similar proper motions and distances. No such sources were found.

In order to identify the Galactic population to which *V341 Ara* belongs (thin disc, thick disc or halo), I carried out Galactic orbit integrations with GALPY, assuming a standard Milky Way potential (MWPotential2014, Bovy, 2015). The starting point for these integrations is the system's current position in the full six-dimensional phase space, which is defined by proper motion (2 components), position (2 components), distance (1 component) and systemic radial velocity (1 component). All but the last of these are provided by Gaia. For the systemic radial velocity, I adopt the value obtain by our spectroscopic analysis in Section 2.3.4.4, $v_{sys} = 42 \pm 2$ km s^{-1}.

The Galactic orbit implied by these parameters is characterized by a pericenter distance of 5.32 kpc and an apocenter radius of 8.46 kpc, which corresponds to an eccentricity of $e = 0.23$. The maximum height of the orbit above the mid-plane of the Galactic disc, $h_{max} = 57.3$ pc, clearly suggests membership of the thin disc population (Figure. 2.9). This is in line with expectations for long-period CVs from Pretorius et al. (2007).

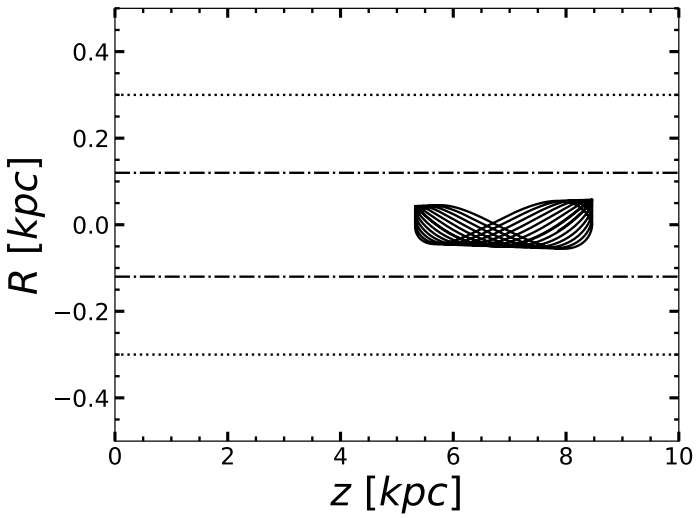

FIGURE 2.9: Vertical vs radial projection of *V341 Ara* orbit around The Galaxy integrated for 1 Gyr in a Milky Way potential produced with GALPY. Horizontal dash-dotted line correspond to the scale height for long period CVs from Pretorius et al. (2007), while the dotted line represent galactic thin disc population scale height from Gilmore & Reid (1983).

2.3.4 Optical spectroscopy: orbital ephemeris and mass ratio

2.3.4.1 The mean spectrum

Figure 2.10 shows the mean optical spectrum of *V341 Ara*, as obtained by averaging all of the observations we obtained with *Chiron* at the CTIO. Prior to combining the individual spectra, each was shifted to the rest frame of the secondary, based on the radial velocity curve derived in Section 2.3.4.4 below.

As expected from the overall SED (Figure 2.3), the optical spectrum is very blue. The continuum shape is reasonably approximated by $F_\lambda \simeq \lambda^{-7/3}$, the spectrum expected for the central part (between the Wien and Rayleigh-Jeans tails) of a Shakura-Sunyaev multi-temperature black-body disc.

The other key aspect of Figure 2.10 is that it shows an *absorption* line spectrum. This, again, suggests a face-on for *V341 Ara*. Overall, the optical spectrum is reminiscent of that produced by RW Sex, another bright, nearby, long-period, low-inclination non-magnetic NL (Beuermann et al., 1992).

2.3.4.2 Radial velocity measurements

Figure 2.11 shows a trail of the Hα and He I λ6678Å region in our 4.5 hrs of continuous observations with *WiFeS*. For clarity, the data are already shown here folded on the orbital period of $P_{orb} \simeq 3.65$ hrs.

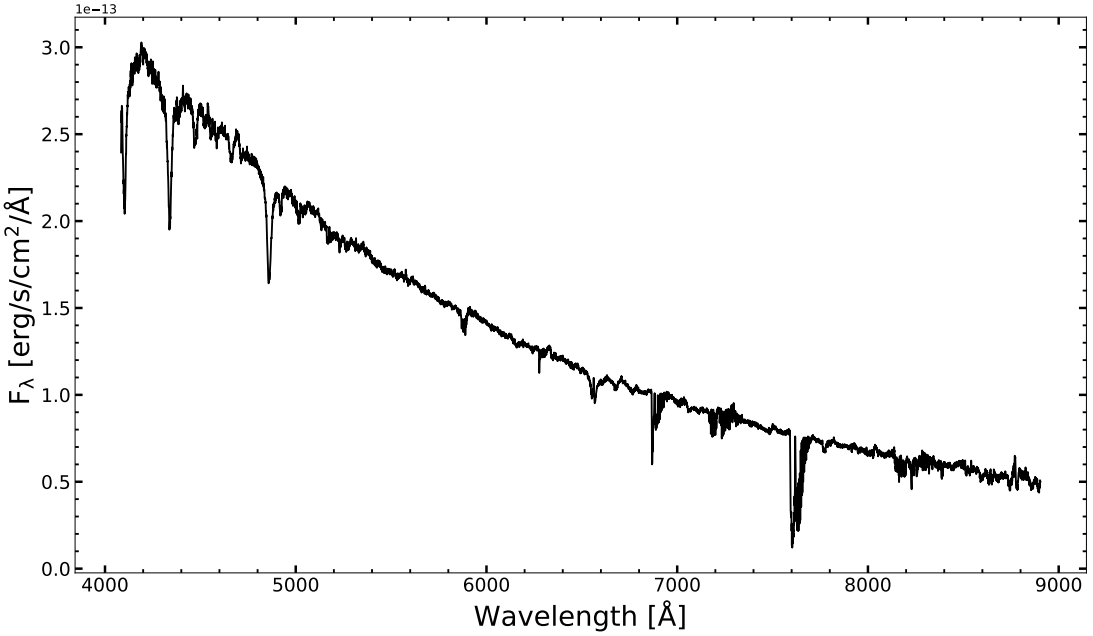

FIGURE 2.10: Median spectrum of all the observations taken with *Chiron spectrograph*. In contrast to the *WiFeS* campaign (see fig. 2.12), the combined spectrum is dominated by the high flux state in where the absorption lines from the accretion disc's atmosphere strongly dominate the observed spectrum. Note strong features at wavelengths above $\lambda \simeq 6800$Å are due to telluric absorption.

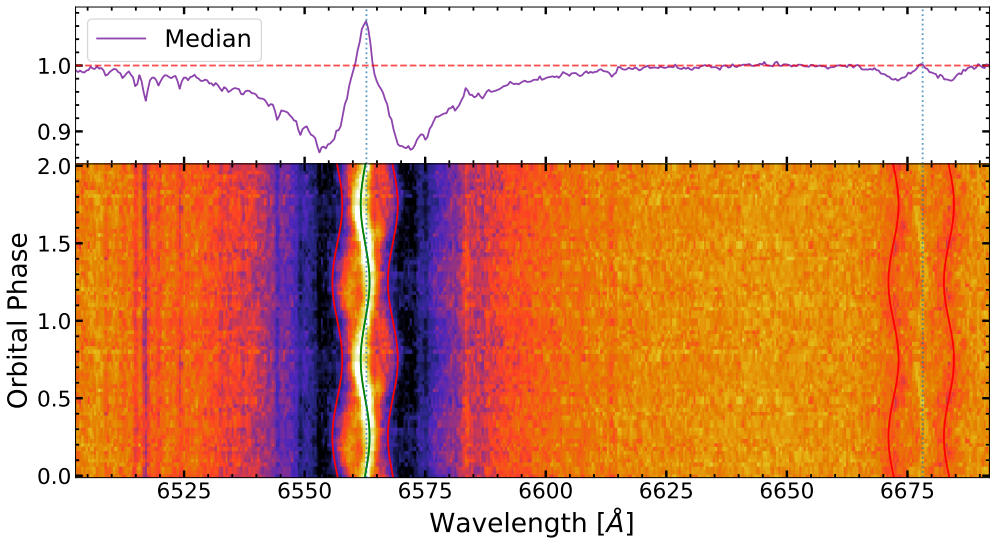

FIGURE 2.11: Phase folded trailed spectrum of the *WiFeS* time-resolved spectroscopy (bottom), normalized median in arbitrary units (top). Rest position of Hα λ6562Å and He I λ6678Å are marked with vertical dotted lines, sine-waves of the primary (red) and secondary (green) components from parameters quoted in Table 2.3 overlaid to guide the eye. The He I component illustrate better the "S-wave" of the absorption component. For clarity, the primary (absorption) component is plotted twice with a shift in order to lay on top of the absorption wings.

It is immediately obvious from Figure 2.11 that *V341 Ara* is a double-lined spectroscopic binary. In both transitions, the central emission peaks and broad absorption wings display clear, anti-phased S-waves. The obvious interpretation is that the broad absorption lines are produced in the atmosphere of the optically thick accretion disc, whereas the narrow emission line cores are formed in the irradiated face of the secondary star. The same phenomenology is seen in other accreting compact binaries, including bright NLs, such as IX Vel (Beuermann & Thomas, 1990) and RW Sex (Beuermann et al., 1992).

Closer inspection of Figure 2.11 suggests the presence of additional emission line components. For example, a faint S-wave that is roughly anti-phased to that associated with the main emission core, but shares a similar velocity amplitude, can be seen near the center of the Hα line. As illustrated in Figure 2.12, this and at least one other component can be more clearly identified in some of our high resolution, high signal-to-noise spectra. These components are probably associated with asymmetric line-emitting structures in the accretion disc, such as the bright spot at the point where the stream impacts on the outer disc (Section. 1.1.4.4).

If not accounted for, the presence of these additional components could bias radial velocity measurements of the two main components, which I intend to use as tracers of the primary and the secondary. This concern applies particularly to the disc-formed, "double-dipped", broad absorption line, which is harder to centroid than the narrow central emission line core. In order to avoid such biases, I therefore fit each spectrum in each of our data sets (*Chiron*, *SALT*, *SpUpNIC*, *WiFeS*) with a combination of a single Lorentzian absorption component and three Gaussian emission components. An initial fit in which all parameters were allowed to vary freely revealed that the components could be split into three distinct groups with different widths: FWHM < 150 km s^{-1}, 150 km s^{-1} $<$ FWHM < 220 km s^{-1} and FWHM > 250 km s^{-1}. Visual inspection of the data also provided limits on the centroid of the main emission component. This information was then used to set the initial parameter guesses and constrain a refined fit in which the posterior probability distributions for all model parameters were obtained via Markov Chain Monte Carlo with EMCEE[6] (Foreman-Mackey et al., 2013). Simple non-informative uniform priors were adopted for all fit parameters. The uncertainties on the fit parameters were then estimated from the 16% and 84% quantiles of the sampled posterior. These posteriors exhibit roughly normal distribution for the parameters of interest.

2.3.4.3 Orbital period and ephemeris

In order to determine an accurate orbital period and ephemeris for *V341 Ara*, I focused on the main emission component of the Hα line. This allowed us to combine our radial velocity estimates for this component with those obtained by B18, which greatly

[6] http://dfm.io/emcee/current/

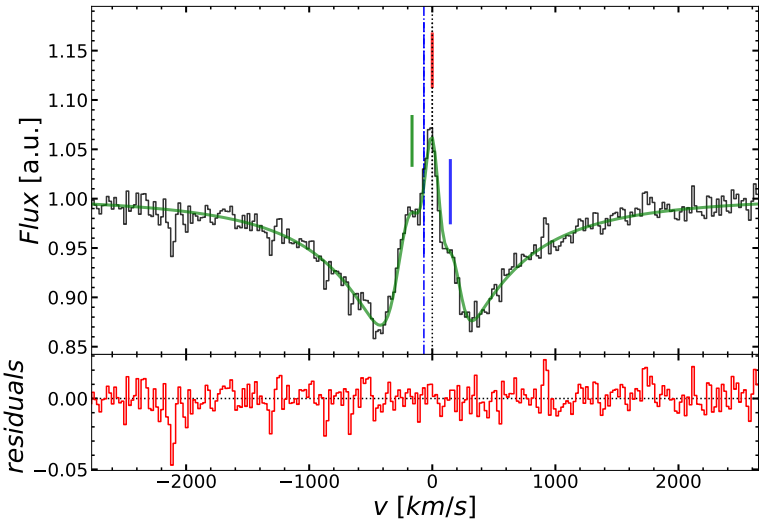

FIGURE 2.12: Zoom in to Hα emission component illustrating the evidence of simultaneous three emission components filling the broad absorption. Black histogram is the observed spectrum while green line is the best fit to a composite model with one absorption plus three emission components. Rest velocity of the transition is marked with a vertical black dotted line, the blue dash dotted line indicate the estimated position for the absorption component, while the colour vertical bars are centered in the position of each component in the model. Residuals of the fits are shown in the bottom panel.

extends the time base of the analysis, and hence increases the precision of the result. All observation times were transformed to a barycentric reference frame using the algorithm described by Eastman et al. (2010).

Before combining all of these measurements, I first estimated periods separately for the 2006, 2017 and 2018 data sets. I found that all of these agreed to within their respective errors, and also with the period estimate for the 2006 data previously reported by B18.

The combined data from 2017 and 2018 provide sufficient precision to phase these observations without cycle count ambiguities across the $\simeq$27000 orbit gap to the 2006 CTIO/RC data set. Applying the same Lomb-Scargle periodogram and bootstrapping techniques described in Section 2.3.2 to the combined radial velocity data allowed us to determine the orbital period to millisecond accuracy, $P_{orb} = 3.6529454^{+0.0000016}_{-0.0000013}$ hrs. The corresponding full orbital ephemeris is

$$T_0(BJD) = 2457098.01142(39) + 0.15220606(6)E \tag{2.1}$$

where T_0 refers to the blue-to-red crossing of the narrow emission line. This should correspond to inferior conjunction of the secondary, provided the line faithfully traces the orbital motion of the companion star.

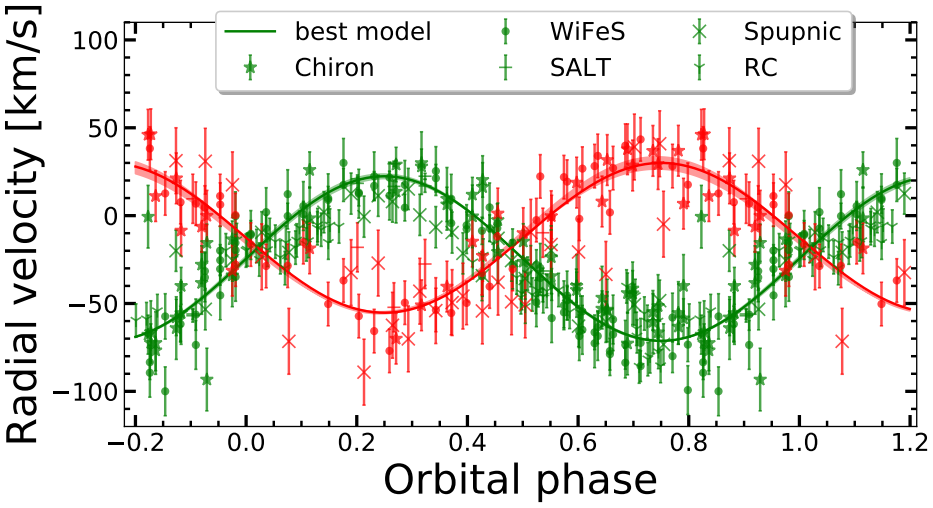

FIGURE 2.13: Phase folded radial velocity curve of the main emission component (green, including Hα and Hβ) and broad absorption (red, only Hβ). Best fit sinusoidal model is represented with a solid line with 1σ uncertainties as shaded region.

2.3.4.4 K-velocities and system parameters

In order to determine the K-velocities of the primary and secondary, I fit the radial velocity measurements of the absorption and main emission components with sinusoids,

$$v_{abs} = \gamma_1 + K_1 \sin\left(2\pi/P_{orb} + \phi_1\right), \tag{2.2}$$

and

$$v_{em} = \gamma_2 + K_{2,obs} \sin\left(2\pi/P_{orb} + \phi_2\right). \tag{2.3}$$

All parameters were allowed to vary in the fit, except the orbital period, which was sampled from the probability distribution obtained above. The resulting parameters and uncertainties are listed in Table 2.3.

The measured phase offset between the absorption and emission line radial velocity curves is $180.0^\circ \pm 0.3^\circ$. This gives us confidence that these components are tracing the motions of the primary and secondary, respectively (c.f. Cantrell & Bailyn, 2007, and references therein).

If the absorption lines are formed in the atmosphere of an optically thick, symmetric accretion disc, the measured $K_1 = 42 \pm 2\,\mathrm{km\ s^{-1}}$, is an unbiased estimate of the projected orbital velocity of the primary. However, if the main emission line component arises only on the irradiated front face of the secondary star, $K_{2,obs} = 47.4 \pm 0.6\,\mathrm{km\ s^{-1}}$, is *not* an unbiased estimate of the secondary's projected orbital velocity. In order to determine the mass ratio of the binary system from our data, I therefore first need to correct $K_{2,obs}$ to the center-of-mass frame of the secondary. This "*K-correction*" (Muñoz-Darias et al., 2005) depends on the opening angle of the shadow cast by the accretion disc on the secondary and also (weakly) on the inclination of the system.

TABLE 2.3: System parameters derived from spectroscopy in Section 2.3.4.

Parameter	units	value	error
$\delta\phi$	degrees	180.0°	0.3°
γ_1	km/s	-12.6	1.4
K_1	km/s	42	2
γ_2	km/s	-24.43	$+0.52/-0.57$
K_{em}	km/s	47.4	0.6
K_2	km/s	84.5	1.6
$q = K_1/K_2$		0.5	0.02
P_{orb} =	$3.6529454^{+0.0000016}_{-0.0000013}$		hours
T_0^{BJD} =	$2457098.01142 \pm 0.00039$		days

For the low-inclination case considered by Muñoz-Darias et al. (2005), $i = 40^\circ$, a moderate opening angle of $\alpha = 10^\circ$ would correspond to a corrected estimate of $K_2 = 82.5$ km s^{-1}. Changing α to 6° or 14° would change this estimate to $K_2 = 85.8$ km s^{-1} or $K_2 = 76.7$ km s^{-1}, respectively. I therefore adopt $K_2 = 85.8^{+3.3}_{-5.8}$ km s^{-1} with the characteristic systematic uncertainty associated with this correction. For no shadowing at all ($\alpha = 0^\circ$), $K_2 = 88.7$ km s^{-1}.

The ratio implied by these K-velocities is $q = M_2/M_1 = K_1/K_2 = 0.51 \pm 0.03(\text{stat})^{+0.4}_{-0.2}(\text{sys})$. This is consistent with the upper limit on the mass ratio imposed by the requirement for stability against dynamical or thermal time-scale mass transfer, $q < q_{crit} \simeq 2/3$ (Politano, 1996; Hjellming, 1989). However, it is somewhat higher than expected for a typical CV at this period. For example, as already noted in Section 2.3.1, a typical donor mass at this *V341 Ara*'s orbital period would be $M_2 \simeq 0.26\,M_\odot$ (Knigge, 2006; Knigge et al., 2011). Combining this with the inferred mass ratio would suggest a low WD mass of $M_1 \simeq 0.5\,M_\odot$. Even allowing for the maximum K-correction (no disc shadowing, i.e. $\alpha = 0^\circ$) would only increase this estimate to $M_1 \simeq 0.55\,M_\odot$.

Both of these numbers are considerably lower than the $\simeq 0.8\,M_\odot$ that is typical for WDs in CVs (Zorotovic et al., 2011). Moreover, the presence of a nova shell around *V341 Ara* would tend to suggest a relatively *high* WD mass for the system. At any given accretion rate, nova eruptions on massive WDs repeat with shorter recurrence times, so *observed* samples of classical novae will tend to be dominated by CVs with high-mass primaries (Ritter et al., 1991). Even though the absorption and emission lines are perfectly anti-phased, this result suggests their radial velocity amplitudes are only proxies for the true K_1 and K_2. Given all this, it is clearly important to confirm the apparently anomalous mass of *V341 Ara*'s WD.

2.3.5 X-ray properties

Figure 2.14 shows the *Swift/XRT* spectra of *V341 Ara* obtained during our two observing epochs. There was no statistically significant variability in the X-ray data within or

between these epochs, so we analysed both spectra simultaneously. The average XRT count rate was only $\simeq 2 \times 10^{-2}$ c s^{-1}, which corresponds to a rather low X-ray luminosity of $L_X, 0.3-10$ keV $\simeq 10^{30}$ erg s^{-1}. As a result, the signal-to-noise of the spectra is relatively poor. Nevertheless, it is clear that there are at least two components contributing to the X-ray emission, with the softer one being dominant. Using 1 keV as the boundary between soft and hard photons gives a hardness ratio of $\simeq 0.6$, which is typical for accreting white dwarfs (AWDs) in a high state (e.g. Patterson & Raymond, 1985).

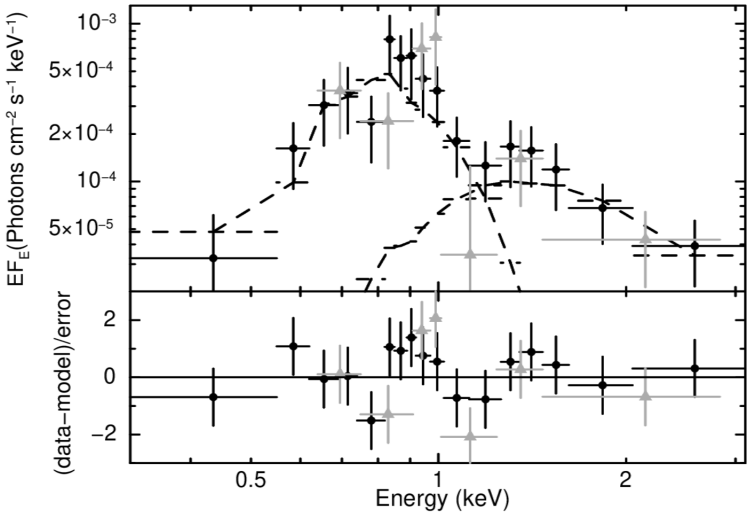

FIGURE 2.14: Combined *Swift/XRT*. Top panel: measured X-ray spectrum. 2019 and 2018 data sets are represented with black dot and grey triangles respectively, the dashed lines are the different components of the model. We use the XSpec model which consists of the Galactic absorption, a blackbody and thermal bremsstrahlung being absorbed with partially ionized gas. In the bottom panel the residuals of the modelling are shown.

Could the dominant soft component be the signature of the optically thick BL? We begin by noting that a relatively cool BL – $T_{BL} \simeq (1-2) \times 10^5$ K, as adopted in our SED models in Figure 2.3 – would be undetectable in our *Swift/XRT* data. Its emission would lie almost exclusively in the extreme ultraviolet band, where even modest interstellar Hydrogen columns are sufficient to extinguish its flux.

How hot would an optically thick emitter need to be in order to account for the soft component in our XRT spectra? We address this by modelling the soft X-ray component as a simple BB and the harder component with a single-temperature bremsstrahlung model. Both components were assumed to be affected by a combination of intrinsic, partially ionised absorption (`tbabs` in XSPEC), plus extinction by the neutral interstellar medium (`phabs` in *XSPEC*, with $N_H = 2.9 \times 10^{20}$ cm^{-2} fixed at a fraction of the Galactic line-of-sight value; Schlafly & Finkbeiner 2011; Zhu et al. 2017). Intrinsic absorption of this type is fairly common in disc-accreting CVs (e.g. Pratt et al., 2004; Mukai, 2017, and references therein).

This model achieves a reasonable fit, $\chi^2_\nu = 1.13$, and the resulting model parameters are summarized in Table 2.4. The $2-\sigma$ lower limit on the temperature of the soft component is $T_{BB} > 600,000$ K. This is much hotter than theoretically expected for an optically thick BL (Balsara et al., 2009; Hertfelder et al., 2013).

We conclude that the *Swift/XRT* spectra of *V341 Ara* are *not* dominated by an optically thick BL. Instead, we suspect that the observed spectrum is produced by non-thermal processes (e.g. shocks in the accretion disc wind of the system; e.g. Mauche 2004a, also see Section 2.3.1) and/or by optically thin thermal emission (e.g. due to an optically thin "chromosphere" or "corona" on top of the optically thick disc and/or boundary layer; e.g. Aranzana et al. 2018). As a qualitative test of these ideas, we also fit the *Swift/XRT* spectra with an optically thin, multi-temperature plasma emission line model (`cemekl`), which has been successfully applied to X-ray observations of other NL CVs in the past (Pratt et al., 2004). Such a model can produce an acceptable fit, but the signal-to-noise of our data is too poor to provide physically interesting constraints on the model parameters.

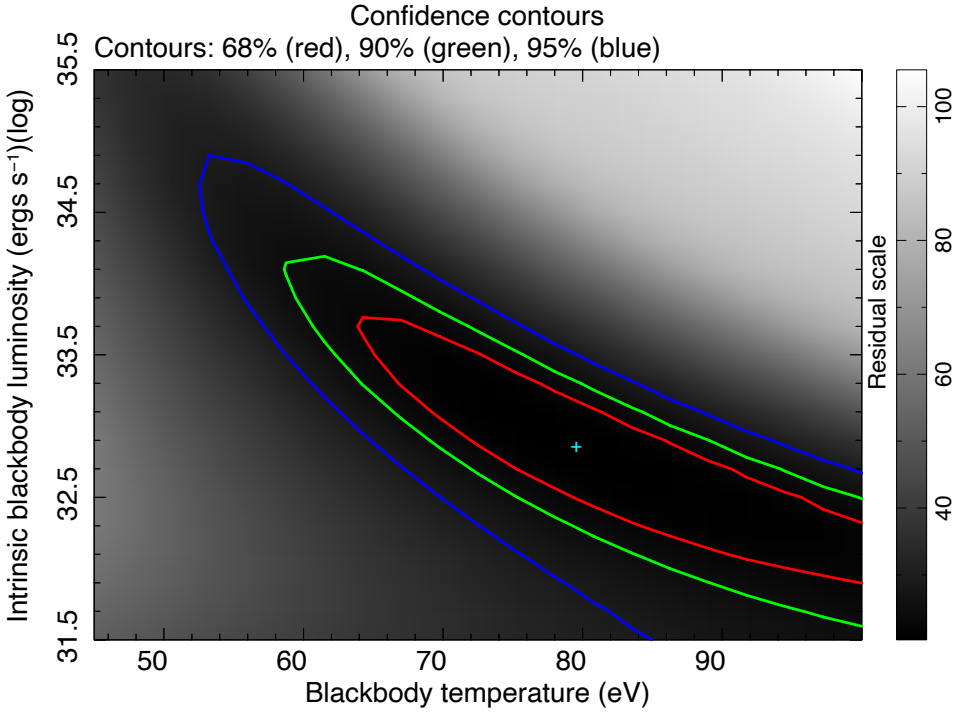

FIGURE 2.15: Intrinsic blackbody luminosity versus effective temperature for an optically thick boundary layer, contours represent the confidence intervals, while the colour scale the residuals for the tested model.

TABLE 2.4: Best parameters estimated from the fit of the two *Swift/XRT* epochs simultaneously (fig. 2.14). * The column density in the line of sight was fixed at a fraction of the Galactic line-of-sight value in order to accommodate the intrinsic n_H.

Model	parameter	units	value	
phabs*	nH	cm^{-2}	2.9	$\times 10^{20}$
tbabs	nH	cm^{-2}	$1.08^{+0.6}_{-0.5}$	$\times 10^{22}$
bremss	kT	keV	$0.73^{+1.25}_{-0.26}$	
	norm		$1.2^{+4.1}_{-1.0}$	$\times 10^{-3}$
bbody	kT	eV	80^{+40}_{-20}	
	norm		$2.3^{+6.4}_{-2.0}$	$\times 10^{-3}$

χ^2	χ^2_ν	C-stats	PHA	DOF
21.45	1.129	20.25	24	19

2.3.6 Optical imaging: nova shell and bow-shock

2.3.6.1 The extended nebula (Fr 2-11)

As discussed by F08 and B18, there are two viable scenarios for the origin of the large-scale Hα nebula around *V341 Ara*: (i) a small HII region composed of interstellar gas that is photoionised by the radiation field of the CV; (ii) material ejected in a relatively recent nova eruption of the system. A third scenario, in which the emitting material is a planetary nebula (PN), can be ruled out, since the mass estimate for this material (based on its Hα luminosity) is only $M_{shell} \simeq 0.005\,M_\odot$, about 40$\times$ less than what is typical for a PN (F08). In both scenarios, the smaller-scale bow-shock is produced where the accretion disc wind associated with the fast-moving CV interacts with the (now) more-or-less stationary large-scale nebula (c.f. Shara et al., 2017; Wareing et al., 2007).

F08 favours the first scenario, on two grounds. First, the emission lines in the nebular spectra are relatively narrow, contrary to what may be expected for a fast, differentially expanding nova shell. Second, there is no *distinct* forward shock at the south-eastern edge of the nebula, nor any other sign of decelerative interaction between a nova shell and the surrounding ISM (B18). Such features might be expected if the large-scale nebula is a nova shell expanding into the ISM. B18 are somewhat more circumspect, noting that the proper motion vector *V341 Ara* places it near the center of the nebula approximately 800 years ago. This positional coincidence, as well as the associated time scale, not unreasonable numbers in the context of the second, nova-shell scenario.

Since identifying the center of the nebula is non-trivial, I obtained an independent estimate of this displacement time scale by overlaying ellipses on the Hα image, centered on the position of *V341 Ara* at times 800, 900, 1000 and 1200 yrs in the past. The middle two of these ellipses provide the best match to the overall shape of the large-scale nebula, so our new estimate of the displacement time scale is 900-1000 years. This is

broadly consistent with B18 and hence in line with the possibility that the nebula is an old nova shell.

I can further test this scenario by considering the luminosity and mass of the nebula. The Hα flux measured by F08 for Fr 2-11 from the Southern Hα Sky Survey Atlas (SHASSA; Gaustad et al., 2001) plates is $\log F_{H\alpha} = 10.99 \pm 0.06$ (in cgs units). This corresponds to an Hα luminosity of $L_{H\alpha} \simeq 3 \times 10^{31}$ erg s^{-1} and, as noted above, a nebular mass of $M_{shell} \simeq 5 \times 10^{-3} M_{\odot}$. At first sight, this mass is somewhat high compared to other known nova shells, which tend to lie in the range $10^{-6} \lesssim M_{shell} \lesssim 10^{-4}$ (Cohen & Rosenthal, 1983; Williams, 1994). However, an eruption $\simeq 1000$ yrs ago would tend to make *V341 Ara* one of the oldest known classical novae, with plenty of time for the nebula to grow in mass by sweeping up material from the ISM. A useful point of comparison here is the recently discovered nova shell around the NL *V1315 Aql* (Sahman et al., 2015), which likely has a similar age and an inferred mass of $M_{shell} \simeq 2 \times 10^{-4}$ M$_{\odot}$yr^{-1}.

On balance, I agree with B18 that the nova-shell scenario for the large-scale nebulosity should not be discounted. As already noted by them, it would therefore be useful to estimate (limits on) the expansion rate of the nebula from archival and/or future images. To provide some context for this, I consider a $\simeq 10^{-5}$ M$_{\odot}$ nova shell that initially expands freely with a velocity of $\simeq 1000$ km s^{-1}. This free expansion phase would then last for about 50-60 years, during which the material travels an angular distance of 2′. After this time, the mass of swept-up material exceeds that of the ejected material, and the expanding shock enters a deceleration phase (the "Taylor-Sedov" phase; Taylor, 1950; Sedov, 1959), during which the expansion velocity scales as $v \propto t^{-0.6}$. Assuming that the ISM is at rest, and adopting a relatively high ISM density $n_e \simeq 10$ cm^{-3} (F08), I then find that in $\simeq$1000 years the edge of the nebula would travel a radial distance of $\simeq 3' - 4'$, in line with the observations.

2.3.6.2 The bow-shock

As discussed in Section 1.6.3.2, an outflow propagating into a medium produces a shock if its speed exceeds the sound speed of that medium; if the source expelling the outflow is also moving supersonically with respect to the medium, a bow-shock forms (e.g. del Palacio et al., 2018, and references therein). Such is the case of *V341 Ara* (see Fig. 2.1 and 2.2), in which the supersonic wind produced by the accretion disc is interacting with a dense environment. The high proper motion of the system ($v \simeq 70$ km s^{-1}) shapes the resulting structure into a bow-shock.

The structure of the bow-shock is determined by the ram pressure associated with the movement of the system through the medium, which produces a quasi-parabolic shell of swept-up material (van Buren & McCray, 1988; Hollis et al., 1992). However, when

the star is not moving in the plane of the sky, projection effects play an important role in determining the observed shape of the shock (Meyer et al., 2016).

In Fig. 2.2 it can be seen that there is an extra, fainter component of the shock South from the source. This suggests that the source is moving mainly in the radial direction, in agreement with the results obtained in our radial velocity study. Our narrow band imaging also shows that, even though the orientation of the bow-shock matches with the proper motion of the star, there is a slight misalignment with the apex of the bow-shock. Specifically, the peak of the enhanced [O III] emission lies slightly West of the source. This could be the manifestation of the biconical shape of the accretion disc wind (Matthews et al., 2015), combined with the misalignment of the accretion disc relative to the plane of the sky.

The presence of the bow-shock allows us to estimate the energetics of the wind. The wind deposits energy into the reverse shock at a rate

$$L_w = \frac{1}{2}\dot{M}_w V_w^2 \,, \tag{2.4}$$

where L_w is the kinetic wind luminosity, and $\dot{M}_w$ and V_w are the mass-loss rate and velocity of the wind, respectively. Under the assumption of an intrinsically parabolic bow-shock, Weaver et al. (1977) derived the minimum distance from the stellar system to the apex of the nebula or the stagnation point (R_2') in terms of the other relevant physical parameters:

$$R_2' = \frac{\sqrt{20 L_w}}{3\sqrt{33\pi\rho_{ISM} V_{ISM}^3}} \,. \tag{2.5}$$

Here, ρ_{ISM} and V_{ISM} are the density of the ISM and its velocity relative to the star, respectively. Dopita (1977) showed that [OIII] originates closer to the front shock compared to other shock-excited emission lines. Therefore, I can estimate $R_2 \simeq 7.5 \pm 0.5'' \simeq 1.7 \pm 0.1 \times 10^{16}$ cm from the [OIII] image (Fig. 2.2). F08 obtained optical spectroscopy of the nebular region around *V341 Ara*. Given that the heliocentric radial velocities of the extended nebular lines are negligible, he concluded that the ISM around the source is at rest with respect to the Sun. He also estimated the electron density of the ISM to be $n_e \simeq 10\, cm^{-3}$ from the extended Hα emission imaging. In Sections 2.3.3 and 2.3.6.2, I measured a relative velocity $V_{ISM} \simeq 76 \pm 1\, km\, s^{-1}$ with an inclination angle of $\theta = 18.7 \pm 0.4$ from the plane of the sky. Rearranging equation 2.5, I can therefore estimate the kinetic power of the wind as

$$L_w = 14.85\pi(R_2 \sec\theta)^2 \rho_{ISM} V_{ISM}^3 = 1.2 \pm 0.2 \times 10^{32}\, \mathrm{erg\, s^{-1}} \,, \tag{2.6}$$

where the $\sec\theta$ term accounts for the symmetry axis of the parabola not being aligned with the plane of the sky, and I have approximated the ISM density as $\rho_{ISM} \simeq n_e m_H$, where m_H is the mass of the hydrogen atom.

To estimate the wind mass-loss rate ($\dot{M}_w$), I need to estimate the terminal wind velocity. Ideally, this would be estimated from wind-formed P-Cygni lines, which are normally seen in the far-UV region (e.g. Prinja et al., 2000). Unfortunately, no FUV spectra of this source have been obtained to date.

In the absence of such data, I adopt a different approach to set an approximate upper limit to the mass loss rate of the source. I consider the region in the flow where the momentum flux of the wind is exactly balanced by the ISM ram pressure: $\rho_w V_w^2 = \rho_{ISM} V_{ISM}^2$. Here, ρ_w is the density of the wind at this point. Approximating the wind as spherical, I can use the continuity equation to express the wind density as $\rho_w \simeq \dot{M}_w / 4\pi R_1^2 V_w$. Combining the two expressions allows us to express the mass-loss rate as

$$\dot{M}_w \simeq \frac{4\pi R_1^2 V_{ISM}^2 \rho_{ISM}}{V_w} \,. \tag{2.7}$$

I can now combine Equations 2.4 and 2.5 to obtain an expression for V_w. Substituting this into Equation 2.7 I obtain

$$\dot{M}_w = \frac{0.54\pi \rho_{ISM} V_{ISM} R_1^4}{R_2^2 \cos^2\theta} \,. \tag{2.8}$$

This include a factor of $\sec^2\theta$ to account for the inclination of the system. Unfortunately, R_1 is not observable, since the high-temperature shocked wind does not produce any optical emission (Weaver et al., 1977; Hollis et al., 1992). However, since $R_1 < R_c < R_2$, I can set an upper limit on the mass loss rate by estimating $R_c = R_2 - \Delta R$, where $\Delta R = 3 \pm 0.5''$ is the thickness of the [O III] bow-shock. With $R_c = 4.5 \pm 0.7''$, the wind mass loss rate has to be $\dot{M}_w < 1.5 \pm 0.9 \times 10^{-10}\, M_\odot\, yr^{-1}$. This, in turn, implies a lower limit on the terminal wind velocity of $V_w > 1600 \pm 500\,\mathrm{km\,s^{-1}}$.

We can extract physical information from the radio upper-limit by introducing a radiative model for the bow-shock. For this purpose, we adapt the one-zone model developed by del Palacio et al. (2018) for bow-shocks produced by runaway massive stars. In a nutshell, relativistic electrons are expected to be accelerated at the strong shock and produce synchrotron emission that dominates the low-frequency radio spectrum. The flux upper limit $S_{1.28\mathrm{GHz}} < 30\ \mu$Jy allow us to constrain parameters related to the synchrotron luminosity: the magnetic field strength, B, and the amount of power injected in non-thermal particles, L_{NT}. To break the degeneracy between these two parameters, we assume a minimum energy condition for the relativistic particles and the magnetic field ($U_{\mathrm{NT}} = 0.75\, U_{\mathrm{mag}}$; Longair, 2011). Adopting $R_0 \sim 10^{16}$ cm, $V_w \approx 1600\,\mathrm{km\,s^{-1}}$ and $\dot{M}_w \approx 10^{-10}\, M_\odot\,\mathrm{yr}^{-1}$, we constrain the non-thermal luminosity to $L_{\mathrm{NT}} < 0.7\%\, L_{\mathrm{w}}$ and $B < 0.5$ mG. This result suggests that disc winds in CVs are not efficient cosmic-ray accelerators.

2.4 Discussion

2.4.1 *V341 Ara* as an old nova

Almost all CVs that are classified as novae were *discovered* on the basis of an observed eruption. This introduces a strong selection bias, since it restricts the time-frame over which we can estimate typical nova rates and recurrence times. In particular, large-area, high-cadence photometric data has only started to become available over the last few decades, a much shorter period than the typical inter-outburst recurrence times expected from nova models ($\tau_{rec} \sim 10^4$ yrs). The population of known novae is thus heavily biased towards systems with unusually short τ_{rec}, i.e. systems with high M_{WD} and/or high $\dot{M}_{acc}$ (e.g. Townsley & Bildsten, 2004; Yaron et al., 2005; Wolf et al., 2013; Kato et al., 2014).

I can mitigate this selection effect by identifying older novae among the "normal" CV population, i.e. among systems where no eruption has so far been noted. One way to achieve this is to match known CVs to bright "guest stars" in old historical records (e.g. Patterson et al., 2013; Vogt et al., 2019). However, probably the best and most systematic method is to search for nova shells around known CVs (e.g. Cohen & Rosenthal, 1983). These shells are composed of material ejected in the nova eruption (plus any swept-up ISM). They are usually observed as emission line nebulae and can remain detectable for centuries (Downes et al., 2001; Duerbeck, 2003).

However, despite several systematic searches (Shara et al., 2012; Sahman et al., 2015; Schmidtobreick et al., 2015), nova shells have so far been identified around only 6 CVs without previously known outbursts: Z Cam (Shara et al., 2007), AT Cnc (Shara et al., 2012), V1315 Aql (Sahman et al., 2015, 2018), Te 11 (Miszalski et al., 2016), IPHASX J210204.7+471015 (Guerrero et al., 2018; Santamaría et al., 2019) and a CV in the globular cluster M22 (Göttgens et al., 2019). The identification of *V341 Ara* as another member of this small group is therefore significant, particularly because it permits two valuable checks.

First, as discussed in Section 2.3.6.1, the offset of *V341 Ara* from the center of the nebula, combined with its proper motion, suggests that the nova eruption took place $\simeq 1000$ years ago. This makes the system one of the oldest "recovered" novae known. It is also a useful constraint for nova models. Specifically, recurrence times are predicted to decrease with increasing M_{WD} and increasing $\dot{M}_{acc}$. Adopting $t_{rec} \gtrsim 1000$ yrs as a lower limit on the recurrence time therefore sets a mass-dependent upper limit on the accretion rate averaged over a nova cycle. For example, interpolating on the model grid of Yaron et al. (2005), I estimate that $\overline{\dot{M}_{acc}} \lesssim 1.7 \times 10^{-8} \left[(M_{Ch} - M_{WD}]/(0.44 M_{\odot})\right]^{1.76}$, in agreement with the SED (Sec. 2.3.1). Here, $M_{Ch} = 1.44\, M_{\odot}$ is the Chandrasekhar mass, and this specific fit is for WD models with a core temperature of $T_{\rm core} = 3 \times 10^7$ K.

Second, *V341 Ara* must have been exceptionally bright during its nova eruption, so it might have been recorded as a "guest star" in historical records. At optical wavelengths, nova eruptions typically have amplitudes of $\Delta m \simeq 11$ mag (Vogt et al., 2019). This implies that *V341 Ara* probably reached $m_{peak} < 0$ during its nova eruption. This would have temporarily placed the system among the top-5 brightest stars visible from Earth; it may even have made it *the* brightest star, other than the Sun. For comparison, Kepler's and Tycho's supernovae are thought to have reached $m_{peak} \simeq -3$ and at $m_{peak} \simeq -4$, respectively (Green & Stephenson, 2003). We thus checked for positional coincidences in several compilations of historical guest star observations (Tse-Tsung, 1957; Stephenson, 1976, 1971; Clark & Stephenson, 1976; Yang et al., 2005; Stephenson & Green, 2009; Hoffmann et al., 2020). There were no matches closer than about 18^{o}, but we did uncover one potential counterpart: # 45 in Stephenson & Green (2009).

This guest star was recorded by Chinese astronomers on Aug 17 of AD 1240 – during the Southern Song dynasty, at a right ascension in the range $16:50 \lesssim \alpha \lesssim 18:05$. Unfortunately, its peak apparent magnitude is not known, and its declination is almost unconstrained. On one hand, V341 Ara would not have been visible on this date from the observatories established in the capital Lin'an (now Hangzhou) during this dynasty (Dao 2019). On the other hand, its altitude at meridian crossing was only $\simeq 1$ below the horizon as seen from Hangzhou (allowing for proper motion, precession and refraction). Thus if the guest star was originally reported by observers located just slightly south of the capital, V341 Ara would be a viable counterpart. In this case, it would be the fourth oldest recovered nova (Vogt et al., 2019) and an excellent laboratory for testing nova theory.

2.4.2 Large-amplitude super-orbital variations from tilted precessing discs

As noted in Section 2.3.2, *V341 Ara* exhibits large-amplitude ($\Delta m \simeq 0.5 - 2.0$ mag), super-orbital quasi-periodic oscillations on a characteristic time-scale of $P_{slow} \simeq 10 - 16$ days. Moreover, the high-quality *TESS* light curve additionally reveals *two* signals at higher frequencies. One of these corresponds to the orbital period ($P_{orb} \simeq 3.654$ hrs), while the other ($P_{SH-} \simeq 3.621$ hrs) is $\simeq$1% faster and consistent with the beat frequency between P_{slow} and P_{orb}.

Photometric signals near P_{orb} have been detected in many CVs. They are generally interpreted as beats between the orbital signal and an intrinsically much slower signal. More specifically, photometric signals slightly slower than P_{orb} are usually called *"positive superhumps"*. The underlying slow signal in this case is thought to be associated with the *prograde* precession of an *eccentric* accretion disc. By contrast, photometric signals slightly faster than P_{orb} are usually called *"negative superhumps"*. The underlying slow signal in this case is thought to be the *retrograde* precession of a disc that is

tilted (or perhaps warped) relative to the orbital plane. A comprehensive discussion of superhumps can be found in Patterson (????).

It is clearly tempting to interpret *V341 Ara*'s large-amplitude super-orbital variations on P_{slow} as the signature of a tilted disc undergoing retrograde precession. The slightly faster-than-orbital variations on P_{SH-} would then correspond to the usual negative superhump signal at the beat period between P_{orb} and P_{slow}. However, there are two serious problems with this idea. First, the so-called period deficit I infer from the *TESS* data, $\epsilon_- = (P_{orb} - P_{SH-})/P_{orb}) \simeq 0.01$ is unusually small. It is significantly smaller than theoretically expected for a tilted disc in a system with $q = M_2/M_1 \simeq 0.5$ (Wood et al., 2009), and it is also smaller than the deficits typically seen in other NL systems (Patterson et al., 2005; Wood et al., 2009, and references therein). Second, the amplitude of the super-orbital variations is exceptionally large. In most NLs exhibiting negative superhumps, the actual precession signal on P_{slow} is either weak or not detected at all, and even the stronger signal on P_{SH-} exhibits amplitudes of $\Delta m \lesssim 0.6$ mag (Harvey et al., 1995).

I suggest that the solution to these problems is connected to the recent discovery of slow, large-amplitude oscillations in a subset of Z Cam stars (Simonsen, 2011; Szkody et al., 2013; Kato, 2019). Z Cam stars are DNe that occasionally "get stuck" near the plateau phase of their outbursts. The photometric variations first noticed by Simonsen (2011) in the proto-type *IW And* (and also in *V513 Cas*) can be roughly described as large-amplitude, damped, quasi-periodic slow oscillations in this stand-still phase (e.g. Kato, 2019). I will refer to this as the *IW And* phenomenon. Several additional systems exhibiting this phenomenon were identified by Kato (2019). He proposed that these variations might be produced by the same thermal-viscous instability that is responsible for ordinary dwarf nova eruptions, if the instability could be somehow confined to the outer disc in these systems (with the inner disc remaining in a hot stable state).

Building on this idea, and noting that several systems exhibiting the *IW And* phenomenon also display negative superhumps, Kimura et al. (2020) suggested that spatially confined disc instabilities may occur naturally in *tilted* accretion discs. The accretion stream from the donor star will impact a tilted accretion disc at a distance from the accretor that depends on both the tilt angle and the precession phase. Kimura et al. (2020) therefore carried out 1-dimensional disc instability simulations in which mass is added in this time- and radius-dependent fashion. The light curves produced by their simulations depend strongly on the adopted system parameters and tilt angles, and some of them show promise as models for the *IW And* phenomenon.

Most of the system parameters investigated by Kimura et al. (2020) lie in a range where ordinary dwarf nova eruptions would be expected for non-tilted discs. However, the highest accretion rates they consider would produce *steady* accretion in the absence of any disc tilt. Systems accreting at these rates would normally be NL variables. Figure 8

in Kimura et al. (2020) shows the predicted light curves for such systems, from simulations designed to mimic tilt angle between 0° and 15°. Remarkably, the light curves for moderate to high tilt angles exhibit large-amplitude variations on the precession period, reaching $\Delta \simeq 2$ mag peak-to-peak. These variations occur because, with mass being deposited mostly at smaller radii, the outer disc is unable to maintain a stable thermal equilibrium and instead periodically drops into a low state. I propose that this provides a natural explanation for the super-orbital variations we observe in *V341 Ara*.

What about the anomalously small "superhump" period deficit I have found in *V341 Ara*? The super-orbital variations in the NL simulations presented in Kimura et al. (2020) are driven entirely by the behaviour of the outer disc. Moreover, Kimura et al. (2020) note that a gap may form in the accretion disc near the radius of the stream-disc impact point. This raises the possibility that the outer disc may precess effectively as a thin ring. This is interesting, because Montgomery (2009) predicts period deficits of $\epsilon_- \simeq 0.01$ for this case, with only a weak dependence on mass ratio, in line with what we observe in *V341 Ara*. However, Montgomery's calculations are for a ring located in the inner disc, and the period deficit scales roughly as $R_{ring}^{3/2}$ (Montgomery 2009; Eq 30), where R_{ring} is the radius of the ring. If this is the explanation for the small period deficit, the outer disc in *V341 Ara* must either be truncated well inside the tidal limit or its precession rate must be driven by conditions at smaller radii (perhaps the stream-disc impact radius).

2.5 Summary

I have presented the first comprehensive multi-wavelength study of the recently discovered cataclysmic variable *V341 Ara*. This system is remarkable because it is the third closest non-magnetic nova-like known, is surrounded by a probable nova shell, and displays a clear bow-shock where its disk wind interacts with the nova shell. The main results and conclusions of our study are as follows.

1. Super-orbital, quasi-periodic oscillations are clearly present in all photometric data sets. *TESS* data additionally revealing both the orbital period and the beat between these two signals. The amplitude of the super-orbital signal is large: $\simeq 0.5$ mag variations are typical, but much larger drops in flux are seen occasionally.

2. The tilted disc instability model recently proposed by Kimura et al. (2020) to explain slow, large-amplitude oscillations in a subset of dwarf novae may also account for the super-orbital variations of *V341 Ara*.

3. Based on its position and proper motion, *V341 Ara* is a member of the Galactic thin disc population.

4. I confirm the $\simeq 3.65$ hr orbital period of the system and provide a high-precision orbital ephemeris.

5. I clearly detect anti-phased absorption and emission line components in our spectroscopy, allowing us to establish the K-velocity of both the accreting primary ($K_1 = 42 \pm 2$) and the irradiated face of the donor star ($K_{2,obs} = 47.4 \pm 0.6$). This allows us to estimate the center-of-mass orbital velocity of the donor, and thus determine the spectroscopic mass ratio of the system, $q = K_1/K_{2,true} = M_2/M_1 = 0.51 \pm 0.03(stat)^{+0.4}_{-0.2}(sys)$. For the expected companion based in the evolutionary tracks, this would imply a WD mass of $M_1 \simeq 0.5 M_\odot$

6. With the exception of the X-ray band, the SED of *V341 Ara* is broadly consistent with expectations based on the evolutionary tracks from KPB11, implying an accretion rate in the range $\dot{M}_{acc} \simeq 10^{-9} - 10^{-8} M_\odot\ yr^{-1}$.

7. *V341 Ara*'s X-ray spectrum is composed of at least two components. If the brighter soft component is modelled as a blackbody, its temperature ($kT_{BB} = 80^{+40}_{-20}$ eV, i.e. $T_{BB} \simeq 9^{+4}_{-2} \times 10^5$ K) is significantly higher – and its luminosity ($\log L_{BB}[\text{ergs s}^{-1}] \simeq 32.9$) lower – than expected for an optically thick boundary layer (BL). The fainter hard component might be associated with shocks in the disc wind.

8. The large-scale nebulosity surrounding *V341 Ara* is thought to have been produced during a nova eruption $\simeq 1000$ yrs ago. Near maximum, it was probably one of the 5 brightest stars in the sky. I tentatively suggest that this eruption might be associated with a "guest star" recorded by Chinese astronomers in AD 1240. This would make *V341 Ara* the fourth oldest recovered nova.

9. I have redetermined the stand-off distance of the bow-shock, $R_{stand-off} \simeq 2 \times 10^{16}$cm. This, in turn, allows us to constrain the mass-loss rate of the system's disc wind: $\dot{M}_{wind} \lesssim 10^{-10} M_\odot\ yr^{-1}$.

V341 Ara is expected to display strong, blue-shifted absorption lines in its far-UV spectrum. Modelling these lines is the standard way to determine the mass-loss rates of CV disc winds, so *V341 Ara* provides us with a rare opportunity to directly test this approach.

Chapter 3

Multi-wavelength observations of the LMXB *Swift J1858-0814*: Overview of the campaign

3.1 Introduction

As discussed in Section 1.6.2, essentially all disc-accreting astrophysical objects show evidence for mass loss in the form of disc winds and/or jets. These outflows allow accreting systems to interact with their environments (Gallo et al., 2005; Fender & Muñoz-Darias, 2016), and may also be critical for the accretion process itself (Esin et al., 1997; Neilsen & Lee, 2009; Scepi et al., 2019).

In compact binaries containing neutron stars or stellar-mass black holes, the disc is often unstable, and most of the accretion takes place during violent outbursts that can last months to years. The most commonly observed disc wind signatures during these outbursts are blue-shifted X-ray absorption lines. However, these signatures are mostly seen in the so-called "soft state", when the jet is quenched and the accretion disc generates most of the luminosity (Ponti et al., 2012). Recently, highly variable wind-formed absorption lines have also been detected in the optical spectra of transient compact binaries in a different configuration, the "luminous hard state", when the power output is dominated by a hot, X-ray emitting corona and a radio jet (Muñoz-Darias et al., 2020). However, the relationship between these disc wind signatures is currently unknown, and no wind-formed lines have so far been seen in an erupting compact binary *between* the X-ray and optical bands, even though the UV contains many of the strongest resonance transitions (e.g. Prinja et al., 2000; Long & Knigge, 2002).

In October 2018, Swift announced the discovery of a new Galactic X-ray transient, *Swift J1858.6−0814* (hereafter J1858). Just before Sun-angle constraints rendered the system

unobservable, X-ray and optical follow-up observations revealed extreme flaring activity, of a kind that has so far only been seen in the famous BHXRB V404 Cyg during its 2015 eruption (e.g. Kimura et al., 2016; Muñoz-Darias et al., 2016; Dallilar et al., 2017) and in V4641 Sgr (Chaty et al., 2003; Muñoz-Darias et al., 2018). The peculiar behaviour of these sources is thought to be a consequence of BHs in super-Eddington accretion regime.

After several months of unusual strong and rapid flaring in its high-luminosity state, the source exhibited strong optical P-Cygni profiles (Muñoz-Darias et al., 2020), suggesting the presence of a dense and cool wind from the outer accretion disc. The dominant spectroscopic signatures of such winds are actually expected to lie in the far-UV region, but they are usually inaccessible in XRBs, due to interstellar reddening. Given its low extinction, J1858 provided us with a rare chance to study the accretion disc wind in the crucial UV band – an opportunity that was missed in the other two extreme flaring systems (V404 Cyg and V4641 Sgr).

Following the approval of an HST Director's Discretionary Program, which would provide time-resolved UV spectroscopy, I initiated a multi-wavelength campaign centered on the date of the HST observations. The aim here was to construct a complete picture of the system by obtaining *simultaneous* time-resolved observations across the electromagnetic spectrum. In addition to HST, the observatories that took part in the campaign were the *Neutron star Interior Composition Explorer* (*NICER*), the *Nuclear Spectroscopic Telescope Array* (*NuStar*), *Swift*, the *Gran Telescopio de Canarias* (*GTC*), the *Very Large Telescopes* (*VLT*; specifically the *X-Shooter* and *Hawk-I* instruments), the *Arcminute Microkelvin Imager* (*AMI*), and the *Karl G. Jansky Very Large Array* (*VLA*). In this chapter, I will provide an overview of this campaign. The observations are described in Section 3.2, and a first, global look at the data is presented in 3.3. The main results from the UV spectroscopy are presented in Chapter 4 and further results are presented in Chapter 5.

3.2 Data Sets

Some of the data sets presented here were contributed to the campaign via existing long-term observational programs. Most of these data sets have already been published, submitted or are in preparation. A summary of all the observations is provided in Table 3.1. To provide context, the *NICER* X-ray light curve of the entire outburst is shown in Figure 3.1 (note that the source emerged from the second sun constrain in a renewed soft state), and the *MAXI* hardness-intensity diagram is shown in Figure 3.2. The strictly simultaneous multi-wavelength light curves constructed from the campaign data are shown in Figure 3.3.

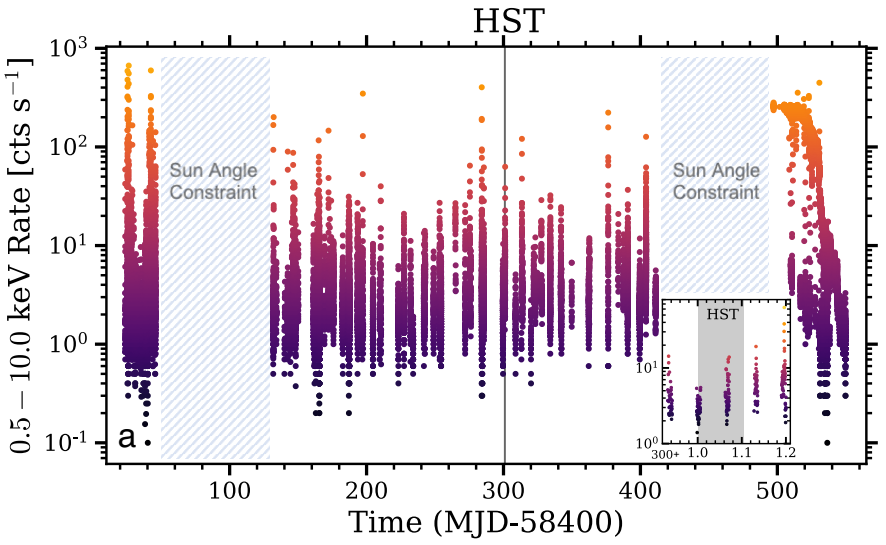

FIGURE 3.1: Outburst evolution overview of the X-ray transient *Swift J1858.6−0814* as observed observed with with *NICER* in the 0.5–10 keV band (reproduced from Buisson et al., 2021); the two large gaps are caused by Sun constraints. The source exhibits flares that reach the Eddington limit during the first 450 days while it is in the hard state. The time of the multi-wavelength campaign led by HST is marked with a vertical line. Colour code refers to the observed count rate. Inset shows a zoom-in around the time of the far-UV HST observations (MJD≃ 58701), indicated with the shaded area.

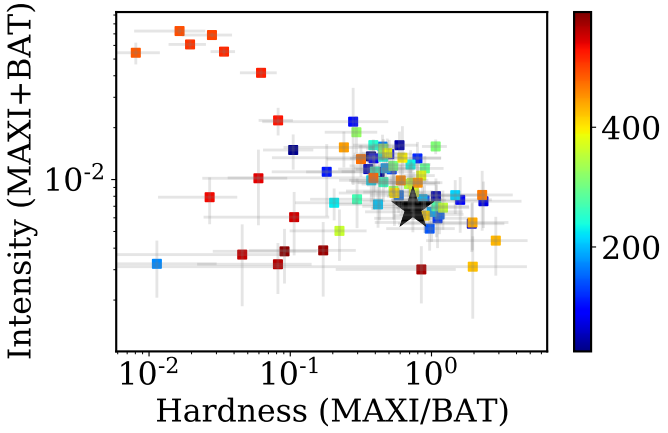

FIGURE 3.2: Hardness intensity diagram of the entire outburst gathered with *MAXI* and *Swift/BAT* all sky monitoring. Data points are binned to ∼10 d in order to achieve enough signal-to-noise. The colour scale represent days in the same scale as Figure 3.1. The state at the time of the campaign is marked with a star, indicating that the source was observed during it hard state. The relatively short soft state of the source correspond to the top left of the diagram.

3.2.1 X-ray

X-ray coverage of the campaign was provided by *NICER* (Gendreau et al., 2016) OBSIDs from 2200400143/4 and *NuSTAR* (Harrison et al., 2013) OBSID 90501333002. *NuSTAR*

data was reduced using the standard NUPIPELINE and NUPRODUCTS software, version 1.9.0. *NICER* data was reduced using the standard pipeline.

3.2.2 Ultraviolet spectroscopy

Swift J1858.6−0814 was observed with *HST* under program GO/DD 15984 (PI: N. Castro Segura) on Aug 5, 2019 23:49:20 UT. A total exposure time of 4.9 kilo seconds (ks) was obtained in the far-UV with the *Cosmic Origin Spectrograph* (COS; Green et al., 2012) and the G140L grating using the primary science aperture (PSA). This configuration provides a spectral resolution of R $= \lambda/\Delta\lambda \sim 900$. In addition to this, near-UV was gathered with the *Space Telescope Imaging Spectrograph* (STIS; Woodgate et al., 1998) and the G230L grating with a 0.2 arcsec slit. In the near-UV, an exposure time of $\simeq$ 2.2ks was sufficient to achieve the required signal-to-noise ratio. All observations were obtained in TIME-TAG mode, yielding a stream of detected events at a time resolution of 32 ms and 125μs for *COS* and *STIS*, respectively.

I reduced the UV data using the HST CALCOS and CALSTIS pipelines[1]. One-dimensional spectra were extracted using the TWOZONE algorithm, which sums over the cross-dispersion direction such that 99% of the flux is extracted at each wavelength. Errors are estimated from Poisson statistics, and the background is modelled with a smooth polynomial and subtracted from the target spectrum.

I also extracted far-UV and near-UV light curves from the TIME-TAG event files, using the same regions defined by the pipeline, except that empirical background correction was directly applied. Regions affected by geocoronal airglow emission associated with *Lyman* α ($\lambda\lambda 1208 - 1225$ Å) and O II ($\lambda\lambda 1298 - 1312$ Å) were masked when extracting the light curves.

3.2.3 Optical spectroscopy

During the *HST* visit, strictly simultaneous observations of *Swift J1858.6−0814* were carried out with *X-Shooter* (Vernet et al., 2011) (program ID 2103.D-5052(A)) and *OSIRIS* (Cepa et al., 2000) spectrographs (program ID GTC23-19A), mounted on the *VLT UT2-Kueyen* telescope at Paranal Observatory and on the *GTC* at the Roque de los Muchachos Observatory, respectively.

X-Shoooter yielded time-resolved optical/NIR spectra covering the range $\lambda\lambda 0.3 - 2.4$ μm. With this instrument we obtained a total of 58 individual exposures with integration times of $\simeq$ 300 s, for a total exposure time of $\simeq$ 17.4 ks. We used slit widths of 0.9 and 1.0 arcsec in the UVB and visible (VIS), respectively, yielding corresponding velocity

[1]Provided by The Space Telescope Science Institute (`https://github.com/spacetelescope`)

resolutions of $\sim$ 51 km s^{-1} and 33 km s^{-1}, respectively. The *X-Shooter* data set was reduced using the standard ESO pipeline ESOREFLEX (Freudling et al., 2013) version 3.3.5. Calibration frames were taken every 1 h and additionally during the occultation of HST by the Earth.

The *GTC/OSIRIS* data set consisted of 20x5 min science exposures, covering the first two hours of the campaign. The R2500R ($\lambda\lambda$5575 – 7685 Å) and R1000B ($\lambda\lambda$4200 – 7400 Å) grisms were used, delivering a velocity resolution of $\sim$ 160 km s^{-1} and $\sim$ 350 km s^{-1} respectively. Further details on the data reduction of these observation are given in (Muñoz-Darias et al., 2020).

3.2.4 Fast photometry

3.2.4.1 Optical

During the first half of the multi-wavelength campaign, we obtained 4.5 ks (1.25 h) of high time-resolution photometry with the *RISE* fast-readout camera (Steele et al., 2008) attached to the 2 m *Liverpool Telescope* at the *Observatorio del Roque de los Muchachos*. The observations were carried out using the 720 nm long-pass filter ($\sim$ I+Z band). The fast readout time of RISE ($\sim$ 0.04 s) resulted in 5 s time resolution. The data reduction was done using the pipeline for the optical imaging component of the LT's infrared-optical software suite. Flux calibration was carried out performed using ASTROPY-PHOTUTILS and referenced to a field star catalogued in PanSTARRS (broad-band i filter).

3.2.4.2 NIR

We collected 4 h of near-IR time-resolved photometry in the K_s band (effective wavelength, $\lambda_{eff} = 2.2\mu m$) with *HAWK-I* (Pirard et al., 2004) mounted on the *VLT UT-4/Yepun* under Program 103.201A.001. The instrument consists of four Hawaii 2RG 2048 $\times$ 2048 pixel detectors. However, by using the FAST-PHOT mode, only a 128 $\times$ 64 pixel window per quadrant is actually read out, allowing us to achieve a time resolution of 0.2 s. The resulting images were stacked in "data-cubes" of 251 frames, separated by a readout gap of $\simeq$ 20s.

The data was reduced with the ULTRACAM software tools (Dhillon et al., 2007). Aperture parameters were derived from the point spread function of a bright (12.51mag) reference star located $\sim$ 22″ west of the target. In order to mitigate seeing effects, calibrated light curves were constructed both for the target and for a comparison star (13.11 $\pm$ 0.03 mag, located $\sim$ 33″ west of the target).

3.2.5 Broad band photometry: GROND

Additional optical (g',r',i',z') and NIR (*JHK*) photometry was obtained using *GROND* (Greiner et al., 2008), a 7-channel imager at the MPG 2.2 m telescope at La Silla, Chile. We observed *Swift J1858.6−0814* with *GROND* between 58701.013568 and 58701.20173, using a series of 12 minute exposures, each with 6 dithers. This produce light curves with a 19 minute cadence. Data reduction was performed using the public *GROND* pipeline from Krühler et al. (2008). Aperture photometry was performed using Source Extractor (Bertin & Arnouts, 1996). A model of the point spread function (PSF) was constructed on bright stars using the PSFEx software package (Bertin, 2011). This model was then fit to the target source to determine the appropriate aperture correction. The resulting net count rates were converted to magnitudes using three comparison stars. In the optical bands, calibration was performed using the magnitudes listed in the *Pan-STARRS1* (Chambers et al., 2016; Flewelling et al., 2020) Data Release 2. In the near-IR, calibration was performed using the magnitudes listed in the Two Micron All Sky Survey (Skrutskie et al., 2006).

3.2.6 Radio

3.2.6.1 VLA

Coordinated radio observations were obtained with the *Karl G. Jansky Very Large Array* (VLA) for $\sim$ 3 h ($\sim$ 10ks) during the last section of the campaign under program 19A-495. All observations, including setup and calibration scans, were taken in C-band using 8 bit modes, with two sub-bands centred at 4.5 and 7.5 GHz, with a bandwidth of 1024 MHz each. Calibration was performed against *3C 286*.

In order to obtain a high resolution light-curve, we split the observation into a set of images with 3-minute cadence in both bands. This allow us to also estimate the radio spectral index α (where $S_\nu \propto \nu^\alpha$). The error on this parameter was computed via Monte-Carlo simulations. Further details on the data reduction are given in van den Eijnden et al. (2020).

3.2.6.2 MeerKAT

We observed *Swift J1858.6−0814* for an hour with *MeerKAT*, as part of the large survey program *ThunderKAT* (Fender et al., 2017). *MeerKAT* observes at 1.28GHz with a bandwidth of 856MHz. We used *PKS B*1934 − 638 as a bandpass and flux calibrator, and *PKS J*1911 − 2006 as a phase calibrator. The data were processed using OxKAT, which is a set of semi-automatic python scripts detailed in Heywood (2020). The scripts calibrate the measurement set within CASA (Version 4.7.0, McMullin et al., 2007), perform

TABLE 3.1: Observing log of the multi-wavelength campaign. t_{obs} indicate the total observing time, PID is the proposal ID, acronyms for the PIs are below the talbe.

Telescope	Instrument	Grating/filter/ band	t_{obs}	PI/Co-PI	PID/ObsID
HST	COS	G140L	4.9 ks	NCS	15984
HST	STIS	G230L	2.2 ks	NCS	15984
VLT	X-Shooter	—	14.4 ks	NCS	2103.D-5052(A)
GTC	OSIRIS	XX	7.2 ks	TMD	23-19A
Gemini-S	Flamingos II	R3K:2.200	6 ks	VC/NCS	2019B-DD-101
VLT	Hawk-I	K_s	14.4 ks	FV	103.201A.001
LT	RISE	720 nm	4.8 ks	TMD/FJI	CL19A04
MPG	GROND	—	15.5 ks	PW/NCS	—
ISS	NICER	0.7-10 keV	6.2 ks	DA	2200400143/4
NuSTAR	—	2-30 keV	22 ks	MOA	90501333002
VLA	—	4.5/7.5 GHz	10.8 ks	JvDE/TR	19A-495
MeerKAT	—	1.28 GHz	3.6 ks	RF/LR	ThunderKAT
AMI-LA	—	15.5 GHz	14.4 ks	RF/LR	—

PIs: Noel Castro Segura, Teo Muñoz Darias, Virginia Cúneo, Federico Vincentelli, Phil Wiseman, Felipe Jimenez Ibarra, Diego Altamirano, Mehtap Özbey Arabacı, Jakob van den Eijnden, Tom Russell, Rob Fender, Lauren Rhodes.

flagging using tricolour[2] and carry out imaging with WSCLEAN (Version 2.5, Offringa et al., 2014).

3.2.6.3 AMI

We also observed *Swift J1858.6−0814* with the *Arcminute Microkelvin Imager – Large Array* (AMI-LA) for 4 hours, starting at MJD 58611.8. AMI-LA is a set of 8 interferometers that observes at 15.5 GHz with a bandwidth of 5 GHz (Zwart et al., 2008; Hickish et al., 2018). We reduced the data using a custom pipeline REDUCE_DC, a script that performs RFI flagging, primary calibration against *3C 286* and phase correction against *J1846-0651* (Perrott et al., 2013). The calibrated data set was interactively cleaned and imaged using the task CLEAN in CASA. Further details about *AMI* and *MeerKAT* data reduction are given in Rhodes et al. (2021; submitted).

3.2.7 Supplementary data

In order to characterise spectral energy distribution of *Swift J1858.6−0814* in quiescence, we have collated additional photometric measurements from PanSTARRS DR1 (optical: grizy; Lin et al., 2016) and VISTA VHS DR4 (J_s; McMahon et al., 2019). We also used data from X-ray all-sky monitor instruments such as *Swift/BAT* and *MAXI* to estimate the X-ray hardness of the source.

[2]https://github.com/ska-sa/tricolour

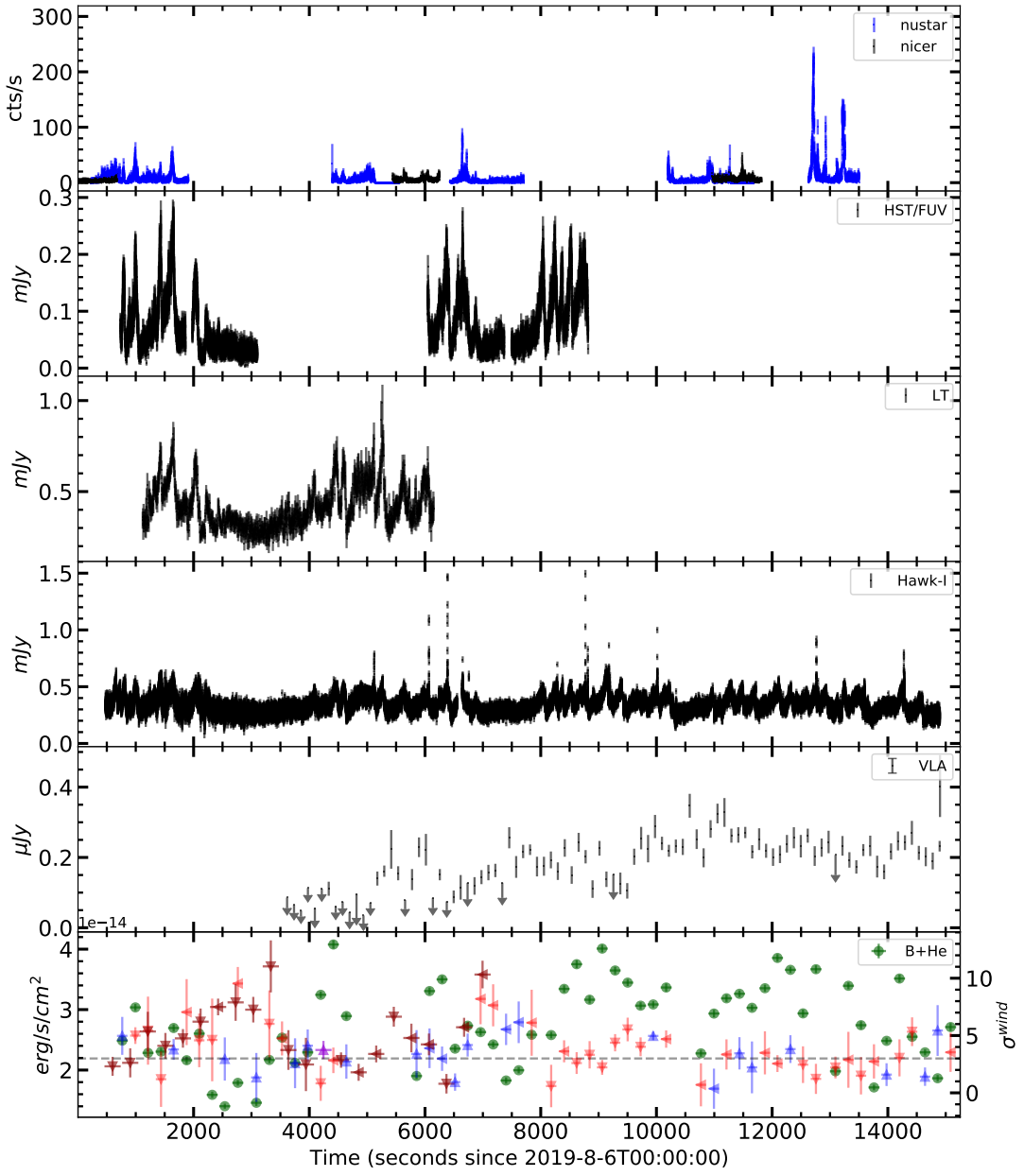

FIGURE 3.3: Overview of the strictly simultaneous data collected during the campaign. Instruments were sorted from top to bottom with increasing wavelength, in the X-rays *NICER* and *NuSTAR*, *HST* in the UV, *Liverpool Telescope* in the optical, *VLT/HAWK-I* in the NIR and *VLA* (4.5 + 7.5 GHz bands) in radio. Finally, in the bottom panel the flux of the Bowen blend and the optical He II as measured from the*VLT/X-Shooter* spectra is shown with green dots. The dark (GTC/OSIRIS) and light (VLT/X-Shooter) triangles in the same panel indicate the significance of the wind signatures (right axis) and the horizontal dashed line indicate the 3 σ level.

3.3 *Swift J1858.6−0814* 's multi-wavelength behaviour during the campaign

J1858 displayed extreme variability during the first stage of its outburst. This was the case in all energy bands, but the variability amplitude was largest in the X-ray region, where the luminosity changed by 1–2 orders of magnitude on time-scales of seconds (see Figure 3.1; Buisson et al., 2021; Baglio et al., 2018; Paice et al., 2018; Rajwade et al., 2018).

The reported X-ray spectrum consisted of a heavily absorbed thermal accretion disc component plus a very shallow non-thermal power law tail (photon flux $N_{ph}(E) \propto E^{-\Gamma}$, with $\Gamma < 1$, e.g. Ludlam et al., 2018; Reynolds et al., 2018). Both the peculiar X-ray spectrum and spectacular variability are reminiscent of the behaviour seen in the outbursts of the well-studied black-hole X-ray binaries *V404 Cyg* and *V4641 Sgr*. In these systems, accretion at super-Eddington rates is thought to be responsible for these signatures (Kimura et al., 2016; Motta et al., 2017a,b; Hare et al., 2020).

In March 2020, several months after the campaign, the detection of Type I X-ray bursts associated with thermonuclear runaways established that the accreting object in *Swift J1858.6−0814* is a neutron star located at a distance of about 13 kpc (Buisson et al., 2020a). The system was also found to undergo eclipses, implying a nearly edge-on viewing angle with respect to the disc ($i \gtrsim 70^{\circ}$) and revealing the orbital period to be $P_{\rm orb} \simeq 21.3$ h (Buisson et al., 2021).

At the time of the campaign, the source still was in its bright hard state (Figure 3.2). In line with previously reported observations (Vasilopoulos et al., 2018; van den Eijnden et al., 2020; Buisson et al., 2021), the source exhibited dramatic flaring activity across all bands, with decreasing amplitude towards longer wavelengths (Figure 3.4).

The X-ray, far-UV and optical variability are clearly correlated, with any lags between these time series being $\lesssim 3$ s (Vincentelli et al. in prep). This suggests that the multi-wavelength flaring is driven by a variable central X-ray source that irradiates the large accretion disc in this system.

The NIR light curve additionally shows strong irregular flares on timescales of $\lesssim 1$ s, this suggest a non thermal origin given the length and brightness (see Figure. 3.6). There is no clear correlation between the slower broad-band flaring activity and the rapid NIR flares. That said, there may be a hint that the latter are preferentially seen during periods of relatively little broad-band flaring activity.

The variable radio counterpart of the source was analysed in detail in van den Eijnden et al. (2020). The long term monitoring of the source reveals a flat to inverted radio spectrum, consistent with a compact jet being launched from the system. (van den Eijnden et al., 2020) found that the radio variability during the hard state was likely

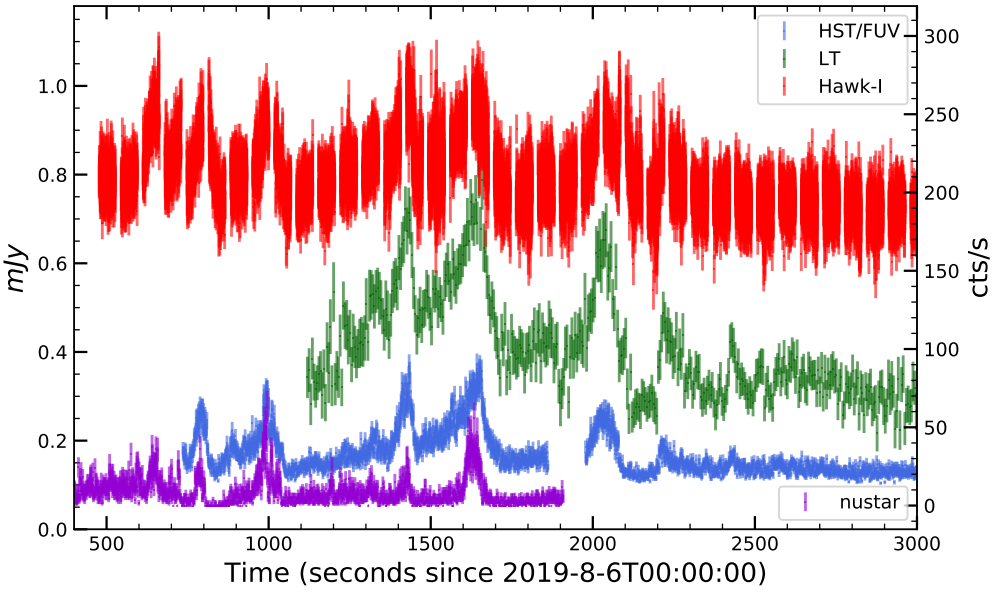

FIGURE 3.4: Light curves of the first $\sim$ 45 minutes of the strictly simultaneous data. Sorted with decreasing wavelength from bottom to top. The amplitude of the broad band flares decrease toward lower energies suggesting the modulation being driven by the X-ray component of the source.

driven by variations in the inner accretion flow that are propagating down the compact jet (e.g. Malzac, 2014). During the campaign, we do not observe any clear correlation between the different bands and the radio emission.

The optical spectroscopy was used to reconstruct a light curve of the Bowen blend + He II emission line flux (hereafter B+He, green points in Figure 3.3). This flux is a proxy of the unobservable extreme-ultraviolet (EUV) emission from the source, under the assumption that the λ4686 line arises from the recombination of He I photoionised in the the system by photons with energies between 55 and 280 eV (e.g. Patterson & Raymond, 1985; Marsh et al., 1994).

The significance with which optical wind signatures could be detected in a given spectrum was also estimated for the optical spectroscopic data sets. For this, I used the method described in Mata Sánchez et al. (2018), which is based on the asymmetries of the Hα emission line profile and has been used in previous searches for wind signatures in XRBs (e.g. Muñoz-Darias et al., 2019). Briefly, the method involves fitting a single Gaussian profile to both sides of the disc line, masking the double-peaked central profile and the wings. After subtracting this Gaussian, the equivalent width (EW) in the wings of the residuals is estimated, and the error is computed by performing a Monte Carlo simulation, using the noise estimated from the nearby continuum.

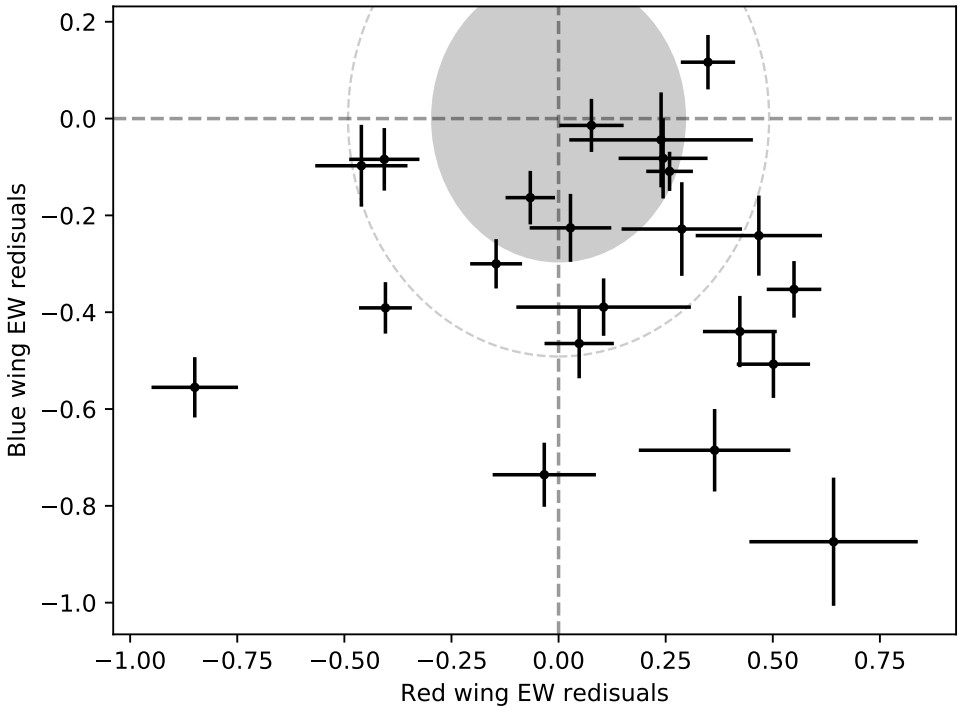

FIGURE 3.5: Wind diagnosis diagram for the *GTC* data obtained during the campaign. The asymmetry of the Hα emission line is estimated by subtracting a Gaussian component from the line, the EW of the residuals is computed. In the sign convention used a negative EW indicate the presence of absorption troughs in the corresponding side of the line. Hence, A negative value in the Y-axis indicate a blue-shifted absorption trough. Shaded and dotted circles indicate the 3σ and 5σ confidence intervals estimated empirically from the noise in the nearby continuum.

For each observed line profile, this procedure yields two numbers: the blue wing and red wing EWs. Either can be positive (emission) or negative (absorption). These measurements are then plotted on a 2-dimensional plot centred on zero (see Figure 3.5), indicating the detection of broad emission wings or absorption troughs on either side of the line. The smoking gun signature of an outflow on this plot will have negative values in the Y-axis.

In the bottom panel of Figure 3.3, the significance which wind signatures are (or are not) detected in this 2-dimensional plot is shown for *X-Shooter* and *GTC* in light and dark colours, respectively. The quadrant in a given measurement lies is coded by different colours and symbols: blue colours indicate a emission feature in the blue wing, while red colours indicate absorption in the blue end, when the point lies in the negative red wing region indicate absorption in the red end of the line. It's worth noting here that the longer exposure times and bigger primary mirror of the *GTC* translates to a better signal-to-noise, hence more reliable spectroscopic data for this purpose.

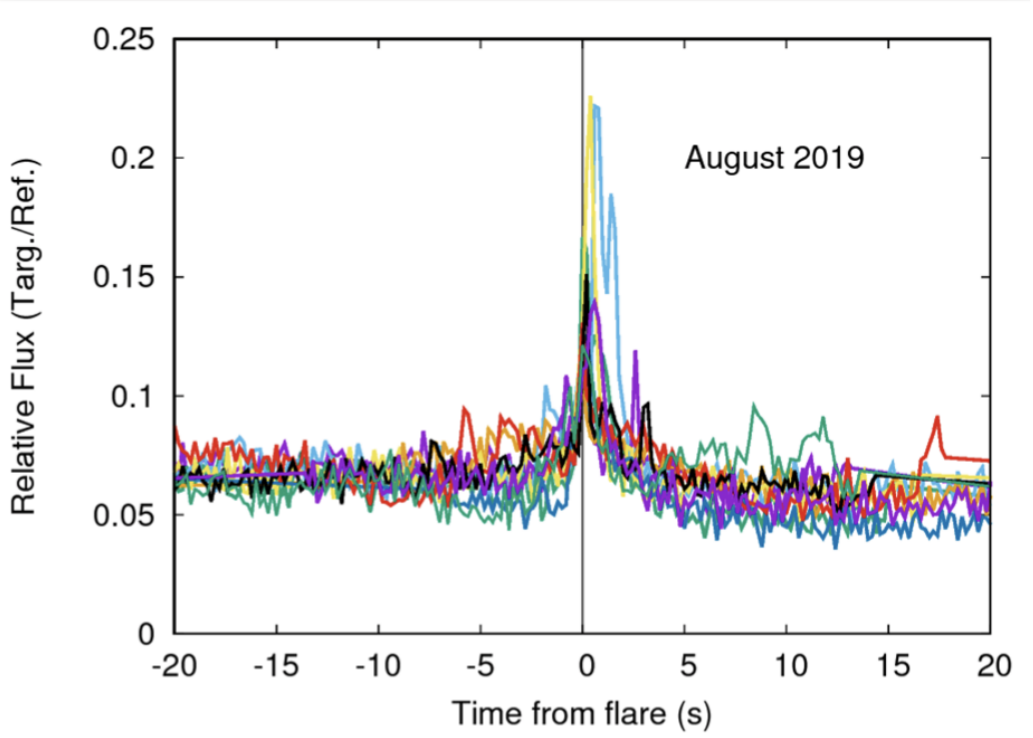

FIGURE 3.6: Large amplitude NIR short flares as observed with *HAWK-I*. The time $t = 0$ indicates the maximum of each flare. No clear morphology pattern is observed.

The strongest B+He emission is stronger when the broad band flaring activity is present. By contrast, the significance of the optical wind signatures is anti-correlated the B+He. This anti-correlation of the EUV/X-ray flux with the strength of the optical troughs was noted by (Muñoz-Darias et al., 2016) in their analysis of the 2016 outburst from *V404 Cyg*. They interpret this effect as a result of H and He becoming overionised, rendering the absorption troughs undetectable. The trailed *X-Shooter* spectrum (Figure 3.7) may support this picture, since the Balmer edge is more accentuated during the non-flaring periods, indicating a higher column density which may help preventing the over-ionisation of the wind when the stronger optical wind signatures and lower EUV flux is observed.

3.4 Summary

The emerging picture of *Swift J1858.6−0814* is of a long-orbital period ($\sim$ 21 h) eclipsing neutron star binary that exhibited variability of more than one order of magnitude across all bands during its hard state. This behaviour resembles BH-XRBs accreting at super Eddington rates. The absence of obvious lags between the variations in different bands are consistent with the reprocessing of the X-rays by the accretion disc atmosphere, this indicates that the variability at longer wavelengths is likely due to X-rays

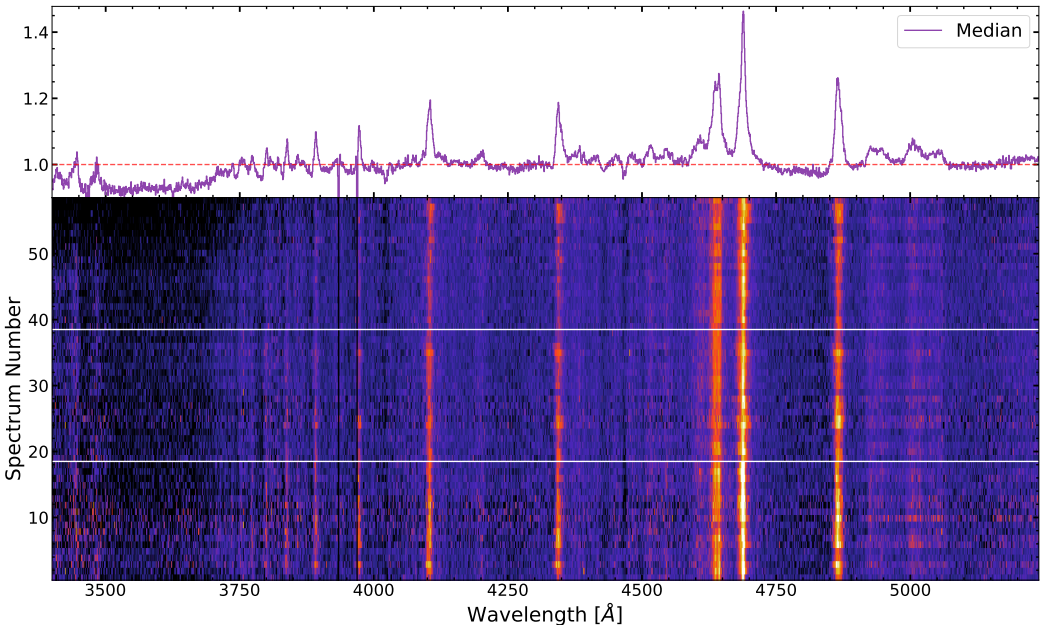

FIGURE 3.7: Normalised trailed spectra of the UVB data obtained with *X-Shooter*. Horizontal white strips indicate the end of the two first HST orbits. The blue end ($\lambda > 3750$Å) was avoided in the normalisation process in order to emphasise the Balmer jump.

emitted near the compact object being reflected/reprocessed further out in the disc. The source also exhibits wind signatures in the optical spectrum, which are anti-correlated with the EUV emission that drives the He II line and the Bowen blend.

In the following two chapters, I will analyse some of the data obtained during the campaign in more detail.

Chapter 4

Multi-wavelength observations of the LMXB *Swift J1858-0814*: A persistent ultraviolet outflow

4.1 Introduction

As introduced in Chapter 3, the trigger of this campaign was the search for accretion disc winds in the ultraviolet resonant lines of the LMXB *Swift J1858.6−0814* . In a first inspection of the far-UV data I noticed most of the lines being skewed to the red with relatively weak absorption troughs. Simultaneous spectroscopic data gathered with *X-Shooter* and *GTC* also also exhibited the same phenomenology in their spectral lines. As discussed in Section 3.3, the profiles in the optical lines exhibit significant variability during the time span of the campaign. Such variations have been already noticed in the context of the long-term campaign, with such variations being more evident from epoch to epoch and within some particular epochs (Muñoz-Darias et al., 2020). The combination of the strong variation in the far-UV light curve during our observation (Figure 4.1), with the variability in the line profiles, motivated us to investigate how these two are related. For this I leveraged the photon counting nature of the COS detectors in order to decompose the spectrum in two components.

In this Chapter, I present the first detection of a wind driven outflow in the UV spectrum of a transient LMXB, and how this relates to the broad band variability in this source. The methodology implemented to study its spectral variability is presented in Section 4.2, along with the mass loss rate inferred from the UV resonant lines and the feasibility of the wind being driven by irradiation of the disc. Results are discussed in Section 4.3.

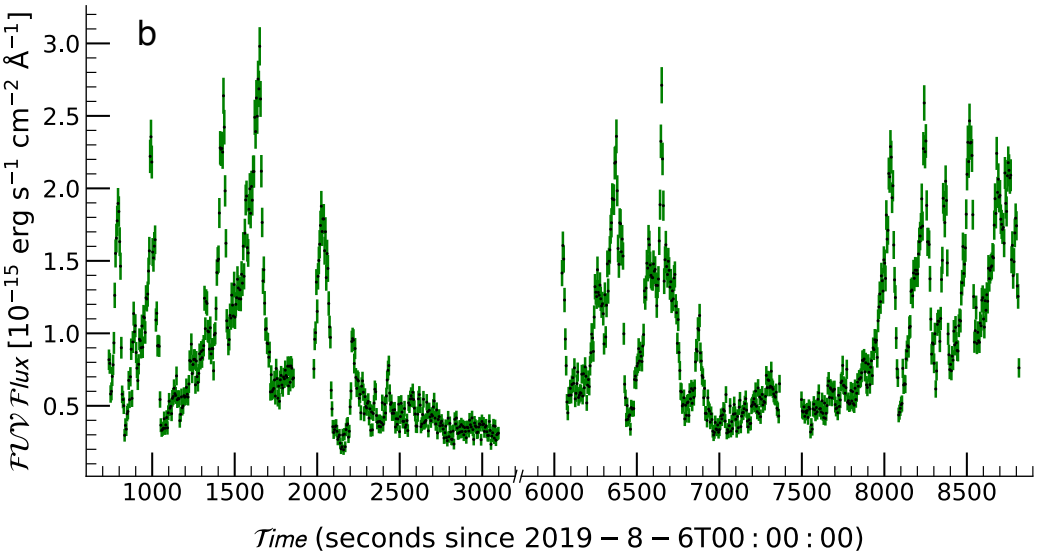

FIGURE 4.1: HST far-UV light-curve in 5s bins of the X-ray transient *Swift J1858.6−0814* , showing strong flares (up to a factor of 10 increase in flux) and flickering at lower flux levels. Green bars represent the standard error, the mean is indicated with small black dot.

4.1.1 Previous X-ray Spectroscopy

Swift J1858.6−0814 was observed by *XMM–Newton* with the *Reflection Grating Spectrometer* (RGS) during March/April of 2019, a few months before the multi-wavelength campaign. A detailed analysis of *XMM–Newton/RGS* observations has already been presented elsewhere (Buisson et al., 2020b), so here I just briefly summarize some relevant results.

As during our campaign, *Swift J1858.6−0814* was in a hard spectral state at the time of the *XMM–Newton/RGS* observations. In fact, there is no significant difference between the X-ray hardness ratios between the two epochs as seen by the all sky monitoring telescopes *MAXI* and *Swift/BAT*.

A search for wind signatures in the X-ray spectrum obtained with the *RGS* did not reveal any clear blue-shifted absorption features, which would be the "smoking gun" for the presence of outflowing material. However, the N VII emission line is significantly redshifted, which suggests that photons in the blue wing might be scattered out of our line of sight by an outflow. Thus, there is tentative evidence for an X-ray processing wind in the hard state from these observations. Assuming a neutron star with typical mass of $1.4 M_{\odot}$, the velocity dispersion observed in this narrow line indicates that the bulk of the emission is originated at $2 - 8 \times 10^9$ cm from the central source, consistent with the wind being thermally driven as discussed bellow.

Finally, the absorbing column density inferred during its soft state is $n_H \simeq 2 \times 10^{21}$ cm^2, similar to the galactic extinction in the line of sight (Buisson et al., 2020a).

4.2 Analysis

4.2.1 Spectral decomposition

The highly variable far-UV luminosity during our observations gives rise to a strongly bimodal logarithmic flux distribution (Figure 4.2). This is in line with the visual impression from the far-UV light curve that the dominant variability is due to "shots" or "flares" superposed on a roughly constant background (Figure 4.1).

I have isolated the spectra associated with these two components by carrying out a simple linear decomposition of our time-resolved spectroscopic data into a constant and a flaring (variable) component. Following Eracleous & Horne (1996), I assume that the flux density $F(\lambda, t)$ at wavelength λ and time t can be written as

$$F(\lambda, t) = C(\lambda) + V(\lambda)D(t), \tag{4.1}$$

where $C(\lambda)$ and $V(\lambda)$ are the spectra of the constant and flaring components, respectively. The function $D(t)$ is the driving light curve of the flaring component.

In order to estimate $D(t)$, I constructed a far-UV continuum light curve at 10 s time resolution. I then estimated the underlying constant level in this light curve and created a normalized driving light curve from which this estimate was removed. I finally smooth the resulting time series with a 5-point, second-order Savitzky-Golay filter to obtain our estimate of $D(t)$. The result is shown as the red curve in Figure 4.3.

With $D(t)$ fixed, the decomposition described by Equation 4.1 becomes just a series of N_λ 2-parameter fits, where N_λ is the number of wavelength bins being considered. Since *HST/COS* uses a photon-counting far-UV detector, the data set actually consists of a time- and wavelength-tagged event stream. Our decomposition is therefore based an unbinned (in time) maximum likelihood fit to the data at the individual photon-event level, since this maximizes the signal-to-noise ratio of the inferred spectral components. The log-likelihood for this model can be derived from Poisson statistics and turns out to be

$$\ln \mathcal{L} \propto \left[\sum_{i=0}^{N_{phot}} \ln \left[\mathcal{C}(\lambda) + D(t)\mathcal{V}(\lambda) \right] \right] - \mathcal{N}. \tag{4.2}$$

Here, $\mathcal{C}$ and $\mathcal{V}$ are now the count-rates associated with the constant and variable components, and $\mathcal{N}$ is the total number of photons predicted by the model. I obtain best-fit estimates of $\mathcal{C}$ and $\mathcal{V}$ by maximising Equation 4.2. The flux-calibrated spectra described as constant and flaring components in Figure 4.6 are then constructed in the usual way, by multiplying by the wavelength-dependent inverse sensitivity curve. Detector regions dominated by background and/or geo-coronal emission are excluded from the fit.

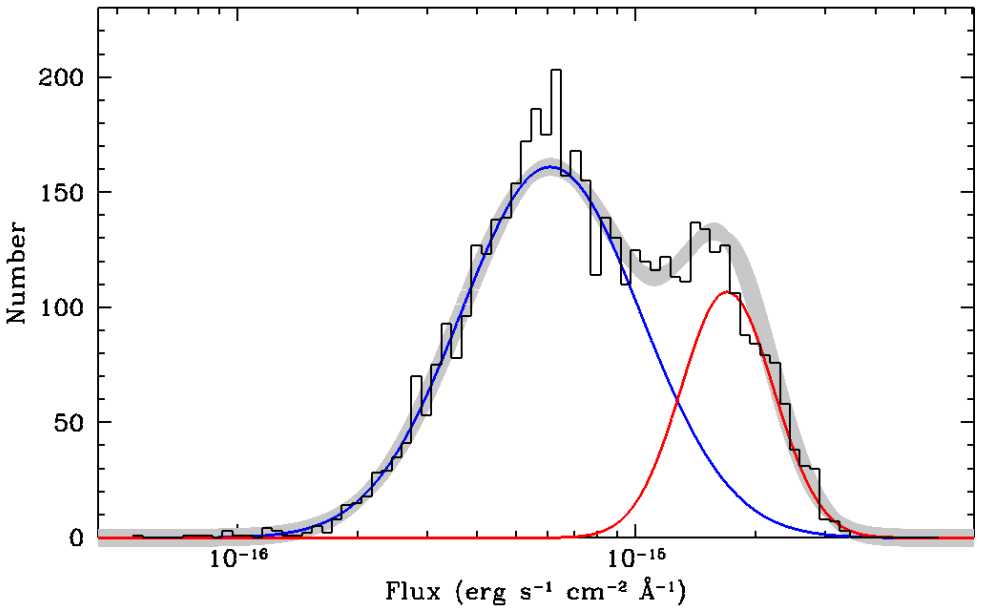

FIGURE 4.2: **The logarithmic far-UV flux distribution of J1858 during our observations.** The distribution is clearly bimodal, consistent with the visual impression from the light curve (Figure 3.1 lower panel) of the variability being due to a flaring component that is superposed on a roughly constant component. The grey line is the optimal decomposition of the distribution into two Gaussians, as suggested by the KMM algorithm(Ashman et al., 1994). The blue and red lines correspond to the individual Gaussians. KMM rejects the null hypothesis of a single component with extremely high significance ($p < 10^{-43}$).

4.2.1.1 Outflow diagnostics

The presence of blue-shifted absorption associated with far-UV and optical lines implies a significant column density of material in the lower level of the relevant atomic transition. This, in turn, can be used to set a rough lower limit on the mass-loss rate of the outflow.

Following Drew (1987), I approximate the outflow as spherical and adopt a simple Hubble-like $v \propto R$ velocity law. Combining the expression for the Sobolev optical depth with the continuity equation, the characteristic optical depth presented by such an outflow at velocity v in a given line can be written as

$$\tau \simeq 74.1 \left(\frac{f_{\rm osc}}{0.2847}\right)\left(\frac{\lambda}{1549.062\ \text{Å}}\right)\left(\frac{A}{7\times10^{-5}}\right)\left(\frac{f_{\rm ion}}{1.00}\right)\left(\frac{\dot{M}_w}{10^{-10}\ \mathrm{M_\odot\ yr^{-1}}}\right)\left(\frac{v}{1500\ \mathrm{km\ s^{-1}}}\right)^{-2}\left(\frac{R(v)}{10^{10}\ \mathrm{cm}}\right)^{-1}. \quad (4.3)$$

Here, $f_{\rm osc}$ and λ are the oscillator strength and wavelength of the line, respectively, A is the abundance of the relevant element, $f_{\rm ion}$ is the fraction of those atoms in the correct ionization level, $\dot{M}_w$ is the mass-loss rate of the outflow, and $R(v)$ is the radius where velocity v is reached in the wind.

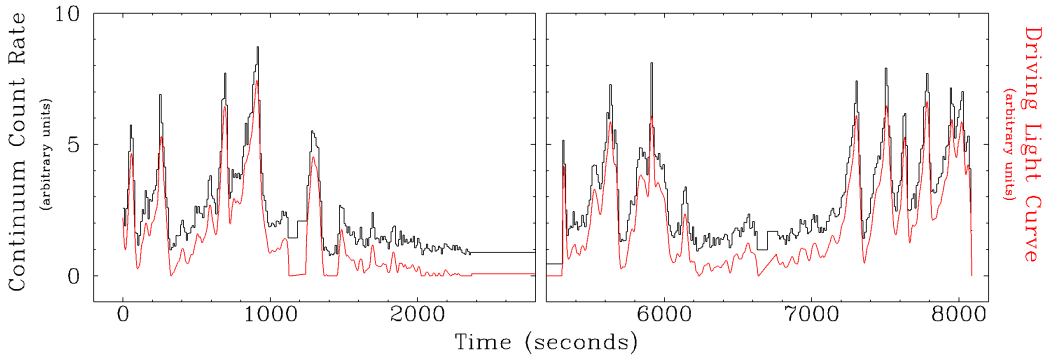

FIGURE 4.3: **The far-UV continuum and driving light curves.** The black histogram shows the light curve of *Swift J1858.6−0814* constructed from three broad wavelength regions that exclude the three strongest emission lines (N V λ1240, Si IV λ1400 and He II λ1640). The specific regions used were $\lambda\lambda$1290 Å – 1390 Å, 1410 Å – 1630 Å, 1660 Å – 1850 Å. The light curve is shown normalized to an estimate of the underlying constant level (80 c s^{-1}). The driving light curve used in the decomposition, $D(t)$, was constructed from this and is shown as the red curve. It was obtained by subtracting the estimate of the constant level, setting any slightly negative values to zero, and using a 5-point, 2nd order Savitzky-Golay filter to produce a slightly smoother, higher S/N version of the light curve.

The reference values adopted for $f_{\rm osc}$, λ and A in Equation 4.3 are representative of the C IV resonance line (treated as a singlet). The reference velocity, $v \simeq 1500$ km s^{-1}, is chosen based on the location of the blue-shifted absorption trough in the far-UV line profiles (cf Figure 4.6). Our adopted value of $R(v) \simeq 10^{10}$ cm corresponds to the radius in the disc beyond which a thermally driven outflow is expected to be launched (see below); it is also roughly the radius where $v_{\rm esc} \simeq 1500$ km s^{-1}. Finally, by taking $f_{\rm ion} = 1$, I ensure that our estimate of $\dot{M}_w$ is a lower limit (modulo uncertainties in the other parameters).

Based on the depth of the absorption features in the far-UV line profiles, I expect that $\tau \gtrsim 1$ for both N V and C IV. The estimated lower limits on the mass-loss rates are then $\dot{M}_w \gtrsim 2 \times 10^{-11}$ from N V and $\dot{M}_w \gtrsim 3 \times 10^{-12}$ from C IV. The larger of these numbers corresponds to a Hydrogen column density of $N_H \simeq 2 \times 10^{19}$cm^{-2}, if I adopt the same quasi-spherical wind model with an inner radius of 10^{10} cm. For comparison, a total column of $N_H \simeq 10^{24}$cm^{-2} is required for the electron-scattering optical depth to reach $\tau_{es} \simeq 1$, as might be expected if the observed flaring is driven by time-dependent obscuration.

4.2.2 A thermally driven disc wind in *Swift J1858.6−0814* ?

The accretion discs in luminous X-ray binaries are subject to strong irradiation. As a result, the upper layers of the atmosphere can be heated to the inverse Compton temperature, which depends only on the spectral energy distribution of the radiation field. The X-ray spectrum of *Swift J1858.6−0814* in the hard state can be approximated

as a power law with photon index $\Gamma = 1.5$ and an exponential cut off at $E_{\rm max} \simeq 30$ keV (Buisson et al., 2020b). For such a spectrum, the Compton temperature is approximately $kT_{IC} \simeq E_{\rm max}/12$ (Done, 2010), which gives $T_{IC} \simeq 3 \times 10^7$ K for *Swift J1858.6−0814* .

Mass loss from these heated layers is inevitable at radii where the characteristic thermal speed of the ions, $v_{\rm th} \simeq 3kT_{IC}/m_p$ exceeds the local escape velocity, $v_{\rm esc}^2 = 2GM/R$. Discs larger than the so-called Compton radius, $R_{IC} = (2GMm_p)/(3kT_{IC})$, are therefore expected to produce thermally driven outflows. For *Swift J1858.6−0814* , I obtain $R_{IC} \simeq 5 \times 10^{10}$ cm. In reality, the radius at which this mechanism turns on is typically $R_{\rm min} \simeq 0.1\ R_{IC}$ (Woods et al., 1996; Proga & Kallman, 2002; Done et al., 2018b). In our mass-loss rate calculation above, I have adopted a characteristic radius $R \simeq 0.3R_{IC}$ for the line-forming region in the outflow.

The disc in *Swift J1858.6−0814* is certainly large enough to drive such an outflow. The orbital period of the system is $P_{\rm orb} \simeq 21.3$ h (Buisson et al., 2021). From Kepler's third law, and assuming that $q = M_2/M_1 \lesssim 1$, the binary separation is $a_{\rm bin} \simeq 3 \times 10^{11}$ cm. If the disc is tidally limited, its outer radius will be roughly $R_{\rm disc} \simeq 0.9R_1$, where R_1 is the Roche-lobe radius of the neutron star (Frank et al., 2002). The outer disc radius is therefore expected to be $R_{\rm disc} \simeq 1 - 2 \times 10^{11}$cm – much larger than R_{IC}, let alone $R_{\rm min} \simeq 0.1\ R_{IC}$.

The final condition for *strong* thermally driven mass loss is that the irradiating luminosity should be sufficiently strong, $L \gtrsim L_{crit} = 0.05L_{Edd}$ (Begelman et al., 1983). This is comparable to the time-averaged luminosity in the flaring hard state of *Swift J1858.6−0814* (Hare et al., 2020). It is therefore likely that the system was luminous enough to drive a powerful thermal disc wind.

4.3 Results and Discussion

The presence of a large, strongly irradiated accretion disc is the key requirement for a thermally-driven outflow (Begelman et al., 1983; Done et al., 2007; Higginbottom & Proga, 2015), while high inclinations tend to strengthen wind-formed absorption features (Ponti et al., 2012; Díaz Trigo & Boirin, 2016; Higginbottom et al., 2020). All of this makes J1858 an ideal candidate for displaying clear observational outflow signatures. X-ray spectroscopy of the source obtained earlier in the same outburst already found tentative evidence for an outflow (Buisson et al., 2020b). Time-resolved optical spectroscopy also revealed clear, but highly variable P Cygni wind features in Hα and He I 5876 Å during the bright hard state (Muñoz-Darias et al., 2020, Figure 4.4).

Figure 4.5 shows the time-averaged far-UV spectrum we obtained with HST in the hard state. The spectrum is rich in both absorption and emission lines that span a wide range of ionization states. Most of the low-ionization absorption lines are centered

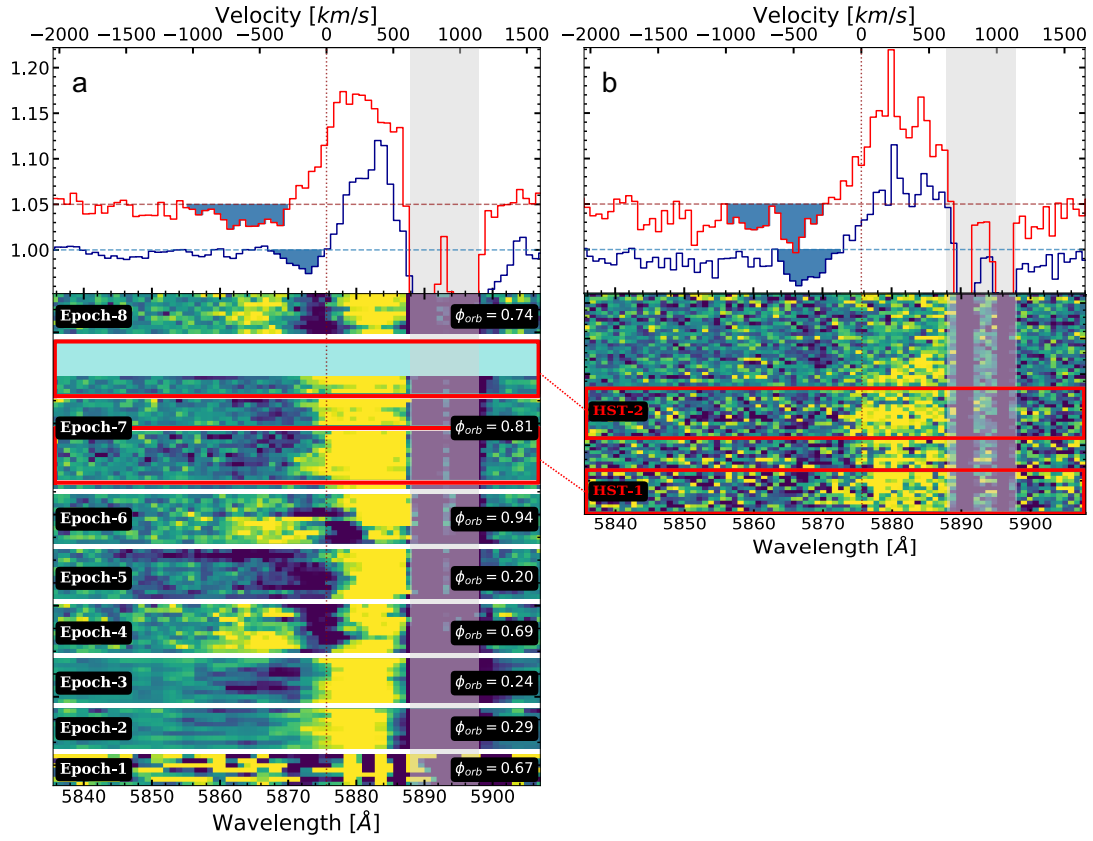

FIGURE 4.4: **Apparently transient optical wind signatures.** (a) Trailed spectra of the 8 *GTC/OSIRIS* epochs published in Muñoz-Darias et al. (2020) with the corresponding orbital phaseBuisson et al. (2021) and (b) *VLT/X-Shooter* during the HST visit centered on He I 5876 Å. The average spectrum of all the observations is shown in the top panel with a blue line. Strictly simultaneous observations during the two ultraviolet exposures are highlighted in red boxes, with their corresponding averaged spectrum shown in red in the top panels with a 5% offset for clarity. Absorption troughs below continuum levels are highlighted with a shaded area. Telluric absorption region around λ 5836 Å is indicated with the shaded vertical band.

at or near the rest wavelength of the relevant transition, with most of these lines not being intrinsic to the system but rather due to interstellar absorption along the line of sight. However, at least two emission lines – N V 1240 Å and C IV 1550 Å – show clear evidence for associated blue-shifted absorption. Since these species are associated with temperatures of $T \simeq$ a few $\times 10^4$ K, their presence unambiguously establishes the existence of a warm and moderately ionized outflowing component.

Several other transitions – e.g. O V 1370 Å and Si III 1440 Å – also show tentative evidence for blue-shifted absorption. Moreover, all strong emission lines in the spectrum – which includes the Si IV 1400Å doublet resonance line and the He II 1640 Å recombination feature – show evidence for a slight red-shift or a red-skew, suggesting that they are also affected by blue-shifted wind absorption.

As shown in the insets of Figure 4.5, the blue edges of the far-UV absorption features extend up to $\simeq -2000$ km s^{-1}, similar to the wind speed inferred from the optical data.

However, the far-UV absorption troughs are considerably deeper than those in the optical, which rarely fall below 90% − 95% of the continuum. This is likely because most of the strong far-UV lines are associated with strongly scattering resonance transitions, whereas the optical features are associated with recombination lines that connect two excited levels. Very high (column) densities are required in order for such recombination lines to produce absorption. On the other hand, sensitivity of far-UV resonance lines to intervening material makes this waveband particularly valuable for studying outflows (Prinja et al., 2000).

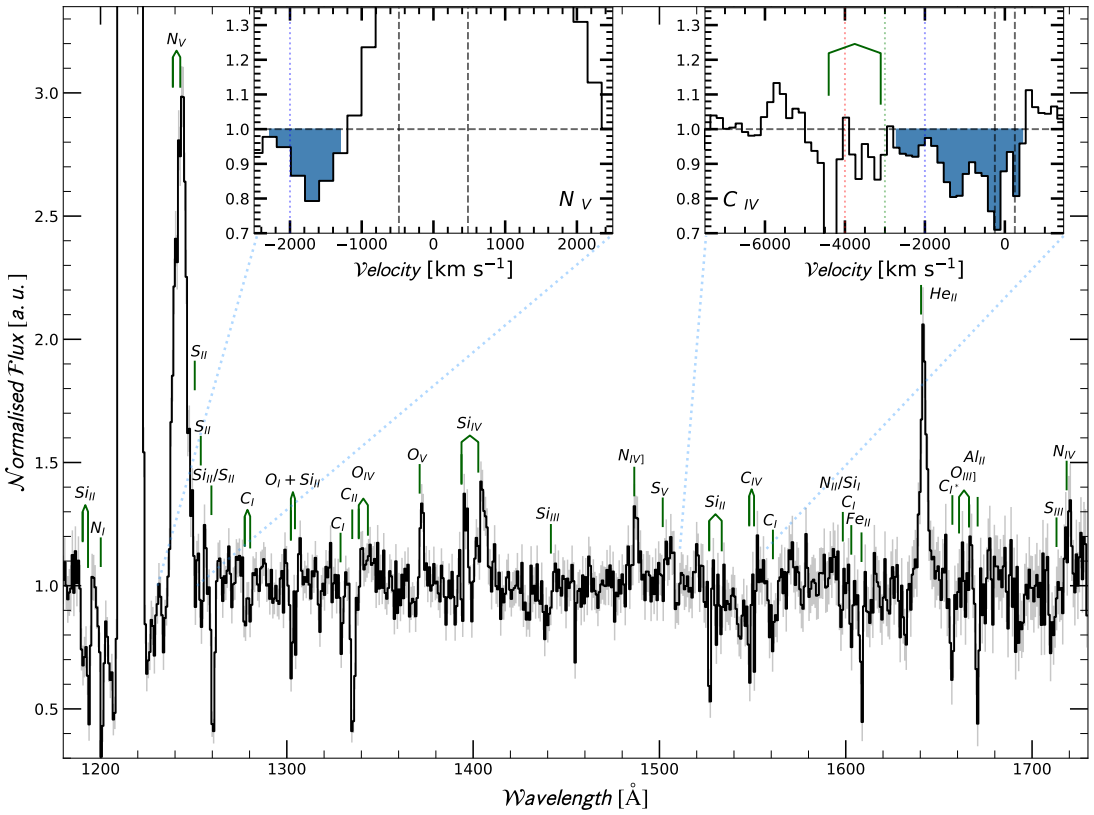

FIGURE 4.5: **Average far-UV spectrum of *Swift J1858.6−0814* during the luminous hard state.** Numerous emission and absorption lines are present; the dominant transitions have been labeled with their corresponding rest position indicated with a green tick. All the emission components are skewed toward shorter wavelengths with blue absorption troughs, which are the characteristic footprint of disc outflows. Light gray area represent the standard error. Insets show a zoom-in to the N V ($\lambda\lambda$1284 − 1437 Å) and C IV ($\lambda\lambda$1513 − 1668 Å) profiles with the blue-shifted absorption signatures highlighted in blue, in the latter nearby Si II interstellar absorption is indicated with connected green ticks. These signatures indicate the presence of a warm, moderately ionized accretion disc wind with characteristic velocities similar to those observed in the optical.

It is important to establish if the far-UV wind signatures are always present or are instead associated with the strong flaring events in the light curve. I have therefore carried out a maximum likelihood linear decomposition of the time-resolved spectroscopy into a constant and a flaring (variable) component. The spectra inferred for the two

components are shown in Figure 4.6. In both N V 1240 Å and C IV 1550 Å, the blue-shifted absorption signature is clearly associated with the constant component. This suggests that either our line of sight to the emitting region responsible for the flaring component does not pass through the warm outflow or that the ionization state of the outflow changes significantly during the flares. Perhaps more importantly, it also suggests that the outflow is, in fact, always present, but that its signatures may sometimes be swamped by the flaring component (in which these signatures are absent). The same effect may be responsible for the transience of the blue-shifted absorption seen in the optical data, especially considering how weak these features are (c.f. Figure 4.4).

The presence of detectable blue-shifted absorption associated with the UV resonance lines (e.g. N V 1240 Å, C IV 1550 Å) implies that the optical depth in these transitions must be significant. This, in turn, requires minimum column densities for the relevant ions, which can be cast as approximate lower limits on the mass-loss rate carried away by the outflow. Conservatively assuming ionization fractions of $f = 1$ for both C^{3+} and N^{4+}, these limits are $\dot{M}_{wind} \gtrsim 2 \times 10^{-11}$ M$_\odot$ yr^{-1} for N V 1240 Å and $\dot{M}_{wind} \gtrsim 3 \times 10^{-12}$ M$_\odot$ yr^{-1} for C IV 1550 Å. The actual ionization fractions may be considerably lower, and the mass-loss rate correspondingly higher.

The apparent time-averaged X-ray luminosity during the flaring hard state in which we observed J1858 was $L_X \simeq 0.01 L_{\rm Edd}$, although individual flares appear to have reached super-Eddington levels Buisson et al. (2020a). Taken at face value, this corresponds to an average accretion rate in this state of $\dot{M}_{\rm acc} \simeq 10^{-10}$ M$_\odot$ yr^{-1}. In this case, $\dot{M}_{\rm wind}/\dot{M}_{\rm acc} \gtrsim 0.2$, suggesting that the wind is dynamically important and could significantly affect the accretion flow (Muñoz-Darias et al., 2016; Shields et al., 1986, but also see Ganguly & Proga (2020)). However, it is also possible that the intrinsic luminosity was much higher throughout this state, with time-variable obscuration being responsible for the reduction in the time-averaged flux (and perhaps also the flaring activity). Such obscuration need not necessarily be associated with the disk wind itself . In the extreme case that $L \simeq L_{Edd}$, the constraint on the wind efficiency is $\dot{M}_{\rm wind}/\dot{M}_{\rm acc} \gtrsim 10^{-3}$.

The discovery of optical, UV and (probably) X-ray outflow signatures in the luminous hard state of J1858 suggests that disc winds may *always* be present in transient X-ray binaries, not just in disc-dominated soft states. Our identification of the *constant* (non-flaring) spectral component as the carrier of these signatures in the far-UV strongly supports this idea. X-ray and far-UV wind signatures have also been observed in some *persistent* soft-state X-ray binaries (Ioannou et al., 2003; Bayless et al., 2010; Allen et al., 2018; Neilsen et al., 2020), i.e. systems in which the disc is not subject to the instability that drives the outbursts of transient accretors (Lasota, 2016; Dubus et al., 2001; Coriat et al., 2012)

The emerging physical picture of disc winds being an integral part of the accretion flows in X-ray binaries is consistent with theoretical modeling of outburst light curves

(Dubus et al., 2001; Tetarenko et al., 2018c). It is also in line with radiation-hydrodynamical modeling of thermally-driven outflows from X-ray binary discs (Luketic et al., 2010; Done et al., 2018b; Higginbottom et al., 2020). These simulations confirm that strong mass loss is inevitable in any systems with a sufficiently large disc subject to strong irradiation, regardless of accretion state Higginbottom et al. (2020). These conditions are met in J1858 as shown in previous sections. A key test of the thermally-driven wind scenario will be to check that wind signatures are absent in systems where these conditions are not met (Charles et al., 2019).

Regardless of the driving mechanism, two key outstanding questions are where and how these outflows manage to sustain a sufficiently low ionization state to allow the formation of optical and UV lines. The most likely answers are that self-shielding, probably coupled with clumping, protects parts of the dense base of the wind above the outermost disc regions from over-ionization. Indeed, recent hydrodynamical simulations of irradiated discs in active galactic nuclei predict the existence of clumpy, thermally unstable, multi-phase outflows (Waters et al., 2021). This mechanism might also be at work in X-ray binaries, but new radiation-hydrodynamic simulations will be needed to confirm this.

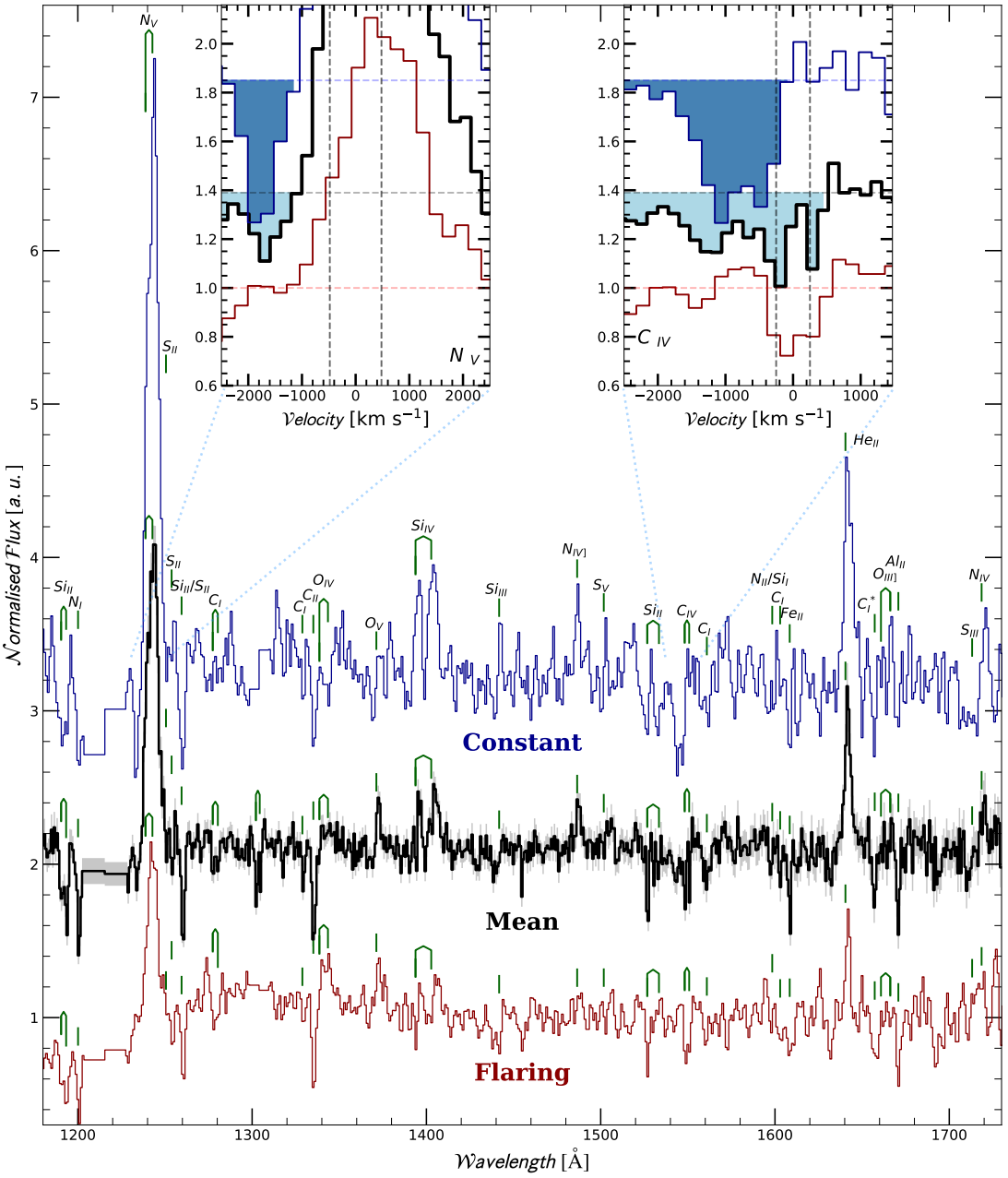

FIGURE 4.6: **Spectral decomposition into a constant (blue) and flaring component (red)**. The latter is driven by the observed continuum variability in the far-UV. The average normalized spectrum is displayed with a thick black line for reference, and all are normalized to the continuum level. An offset has been added to the spectra for clarity. The regions of geocoronal emission like Lyman α and Si II were removed to avoid artifacts in the spectral decomposition. Rest positions of the dominant ions are marked with a green tick and labeled in the top spectrum. Insets are zooms into the two transitions in which the presence of the outflow is more prominent. Specifically, regions covered in the insets are $\lambda\lambda 1284 - 1474$ Å for N V and $\lambda\lambda 1525 - 1717$ Å for C IV.

Chapter 5

Multi-wavelength observations of the LMXB *Swift J1858-0814*: Evolution and intrinsic luminosity

5.1 Introduction

As briefly discussed in previous chapters, the peculiar flaring behaviour exhibited by *Swift J1858.6−0814* is reminiscent of that observed in BH-LMXBs accreting at super-Eddington rates. However, J1858 revealed the true nature of its accretor – a neutron star – by exhibiting thermonuclear powered X-ray bursts during its soft state. This is important, since it provides a good estimate of the distance to the system (Buisson et al., 2020a). In addition to this, the presence of deep eclipses allows us to constrain the inclination and orbital period of the system (Buisson et al., 2021). All of this provides us with an excellent opportunity to study the intrinsic luminosity and broad-band SED of J1858 from the data obtained during the campaign described in 3.

If the donor star dominates the optical light in quiescence, the availability of an accurate distance also allows us to place it on a Hertzsprung-Russell diagram. Additional information regarding the nature of the secondary can be obtained from the ratios of the far-UV resonance lines (e.g. Haswell et al., 2002; Gänsicke et al., 2003). The combination of these constraints allows us to determine its evolutionary state – and hence that of the binary system.

In this Chapter, I use the UV spectroscopy obtained during the campaign, coupled with archival images of the system in quiescence, to determine the mass and evolutionary stage of the donor star in the system. I also use the broad-band SED presented in Chapter 3 to estimate the system's luminosity and discuss the accretion state it was in during its outburst.

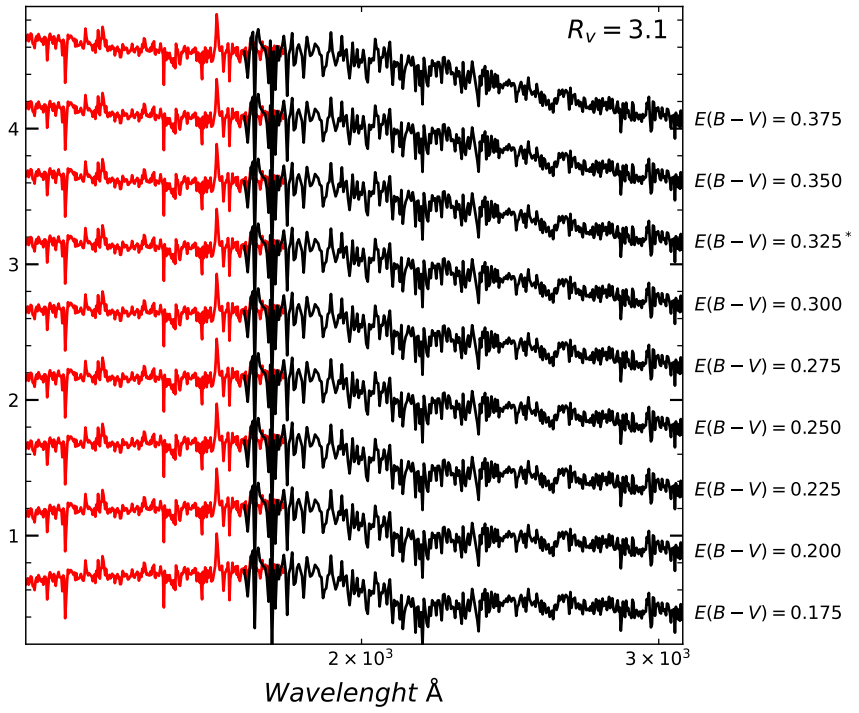

FIGURE 5.1: Time averaged ultraviolet spectrum of *Swift J1858.6−0814* covering Far-UV (red) and near-UV (black) from $1265 - 3100$ Å in arbitrary units. Different reddening values ($E(B-V)$) are applied to illustrate the correction of the UV hump ($\lambda \simeq 2100$) is barely appreciable in steps of 0.025. For illustration purposes the near-UV spectrum was multiplied by a factor of 5 in order to match the overlapping flux

5.2 Analysis and Results

5.2.1 Extinction

Determining the extinction along the line of sight is important for determining the luminosity and SED of the system . This problem is complicated by the fact that there are significant variations between the extinction curves along different lines of sights (e.g. Fitzpatrick & Massa, 1990). The most common approach is to consider a family of generic extinction curves parameterised by the reddening, $R_V = A_V / E(B-V)$. Ultimately, this value depends on the density of the material in the line of sight, being higher for denser environments (see Fitzpatrick, 1999, for a review). For Galactic sources, R_V is normally taken as the average value for the Milky Way, i.e. $R_V = 3.1$.

I estimated the amount of extinction by matching the 2175 Å interstellar absorption feature in the Cardelli et al. (1989) extinction curve to the dip in this region in the *HST/STIS* spectra. This approach is commonly used in a wide class of astronomical objects. Examples of XRBs to which this method has been successfully applied include Nova Muscae 1991 (Cheng et al., 1992), GRO J0422+32 (Shrader et al., 1994), GRO J1655-40 (Hynes et al., 1998), XTE J1859+226 (Hynes et al., 2002).

In practice, I estimated the extinction coefficient by fitting a reddened power law to the observed far-UV continuum. Hynes et al. (2002) showed that a simple absorbed power-law provides similar results to a more complex irradiated disk model, especially given the systematic uncertainties affecting the shape of the reddening law, i.e. R_V. To estimate the statistical uncertainty, I generated a posterior distribution with Markov Chain Monte-Carlo (MCMC) chains. I used the *emcee*[1] implementation of Foreman-Mackey et al. (2013) of Goodman & Weare (2010) to sample the space parameter using chains with 100 walkers per free parameter, 5000 steps and non-informative priors. Spectral lines were masked to avoid bias in the fitting procedure. For the average Milky-Way value of $R_V = 3.1$, I obtained $E(B-V) = 0.324 \pm 0.012\,(stat) \pm 0.025\,(sys)$. The systematic uncertainty associated with varying R_V by $\simeq \pm 1$ around $R_V = 3.1$ is $\Delta E(B-V) \simeq 0.02$. However, as can be inferred from figure 5.1, there are additional systematics associated with the deviations from the assumed power-law shape and the choice of fitting windows. Furthermore, the detailed shape of the 2175 Å interstellar absorption feature can vary between sight lines. Hence I adopt a more conservative systematic error of 0.025.

5.2.2 Companion star

5.2.2.1 Spectral type and luminosity

The progenitor of the X-ray nova is clearly detected in archival images of at least two surveys: PanSTARRS DR1 and VISTA VSH DR4 (J band). Figure 5.2 shows the z-band panSTARRS DR1 image. The field is quite crowded, with a nearby source at $\sim$1 arcsec west to the transient; this may slightly contaminate the quiescent photometric measurements, especially at longer wavelengths.

Despite the possible presence of an accretion disc, the emission in the optical and NIR of quiescent systems is expected to be dominated by the companion star. I have therefore used the 6 available photometric bands, covering the optical and NIR (griyz and J), to estimate the spectral type of the star. The observed SED peaks in the r band, suggesting a relatively warm donor (Figure 5.3).

The SED was fitted by using Phoenix spectral atlas grid (Allard, 2016) implemented in PYSYNPHOT[2]. The model spectra were reddened and synthetic photometry was carried out for each band, using the relevant transmission curves obtained from SVO filter service [3] (see Figure 5.3). The parameter space was sampled using MCMC. The best-fit donor temperature is $T_{2,eff} = 6095^{106}_{-93}$ K, but the surface gravity is not constrained by this purely photometric data set. The metallicity preferred by the fit is skewed to high

[1] https://emcee.readthedocs.io/en/stable/
[2] https://pysynphot.readthedocs.io/en/latest/
[3] http://svo2.cab.inta-csic.es/theory/fps/

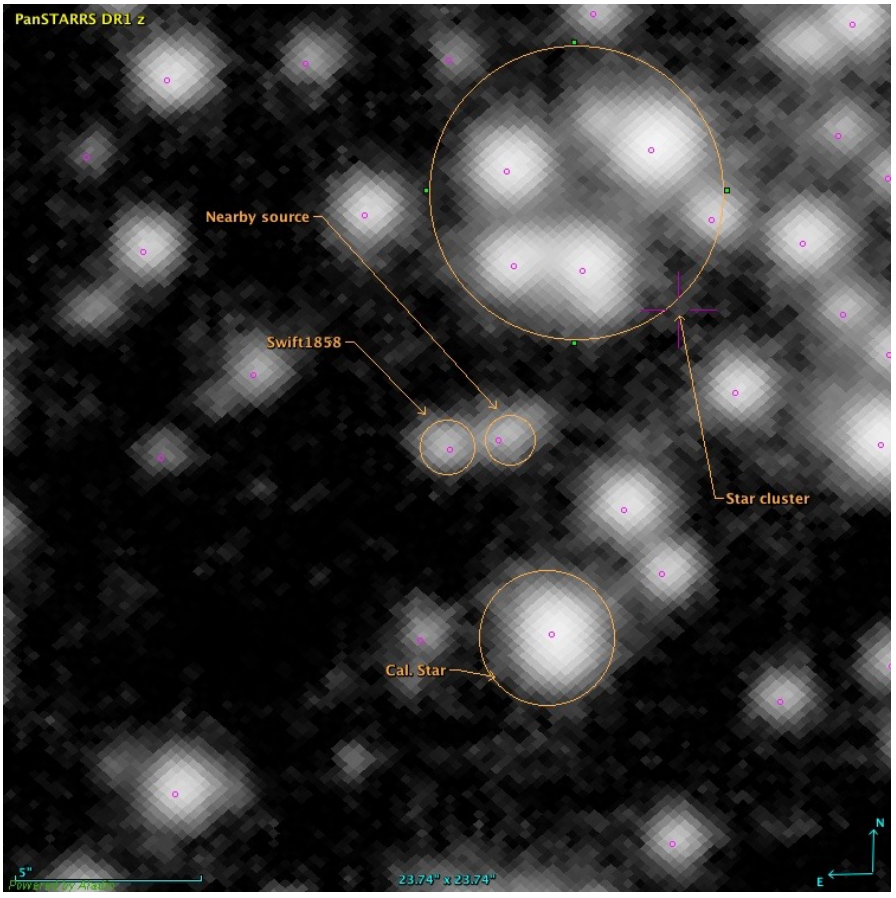

FIGURE 5.2: Field around *Swift J1858.6−0814* as seen in the archival images of PanSTARRS DR1 in the z band. The quiescent counterpart of the XRB is clearly detected in this survey. A nearby source with centroid at $\sim$ 1 arcsec apart is also indicated. The blue dots are the centroid of sources identified by GAIA.

values, with [Fe/H] $\geq$ 0 at 84% confidence. So, based on archival quiescent photometry, the companion star of J1858 likely belongs to the *G*0 spectral class.

To determine the luminosity of the companion star, I use the distance estimates reported by Buisson et al. (2020a). They used time-resolved X-ray spectroscopy to model the evolution of the Type I X-ray bursts in this system. When the bursts are triggered, the luminosity at the surface of the star reaches the Eddington limit. At this point, radiation pressure lifts the material from the surface. The luminosity is expected to remain (approximately) constant at L_{Edd} during this expansion phase and the subsequent contraction of the atmosphere. Therefore, the modelling of these bursts can be used to estimate the distance to the source (van Paradijs, 1978; Kuulkers et al., 2003).

In their table 1, Buisson et al. (2020a) report distances considering different system geometries and abundances. Here, I consider the most conservative estimate (effectively a lower limit), $d = 9.8 \pm 0.4$ kpc, as well as the most likely value, $d = 12.8 \pm 0.7$ kpc. At these distances, neglecting the contribution of the accretion disc in the archival images,

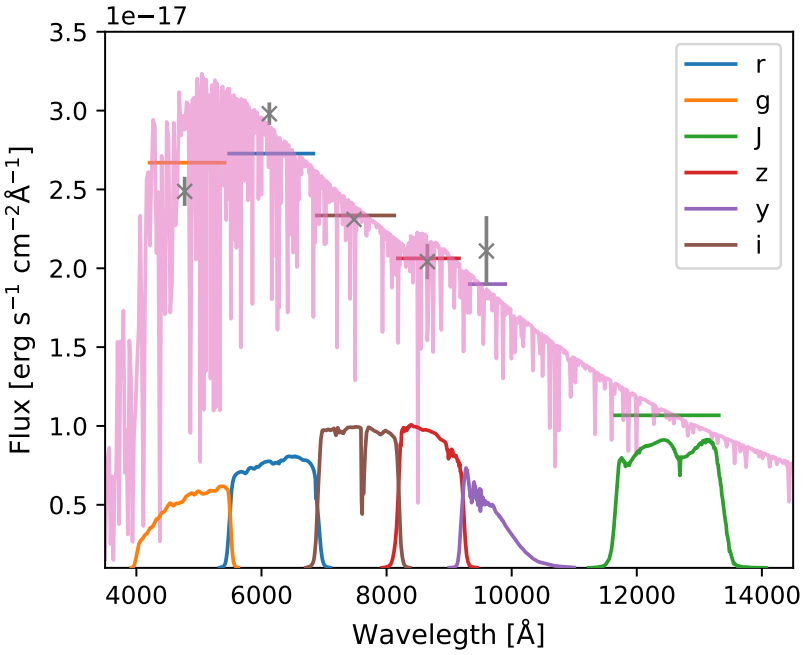

FIGURE 5.3: Quiescent SED of *Swift J1858.6−0814* in different bands (crosses). Stellar model of a *G*0 star is shown with the magenta line. Pass bands of the filters in arbitrary units are also shown (smooth solid lines), the corresponding model flux within a given band is shown with an horizontal line of the same colour.

the implied luminosities of the companion star are $L_2 \gtrsim 4.7 L_\odot$ and $L_2 \simeq 7.3 L_\odot$, with an implied stellar radius of $R_2 \gtrsim 1.8 \pm 0.2 R_\odot$ and $R_2 = 2.6 \pm 0.1 R_\odot$, respectively.

In Figure 5.4, the corresponding position in the Hertzsprung–Russell diagram (HRD) of the J1858's quiescent counterpart is shown, overlaid on top of a set of evolutionary tracks of isolated stars with masses ranging from 1 to $1.5 M_\odot$ computed with MESA[4] (Paxton et al., 2011). This figure clearly suggests that the donor is apparently a fairly massive, $M_2 \gtrsim 1.2 M_\odot$, slightly evolved, sub-giant, i.e. a star that has ended its life on the main sequence.

5.2.2.2 Evidence for CNO processing

The far-UV range covered by HST/COS contains significant spectral lines intrinsically related to the CNO processing in stars. Despite the significant knowledge about the configuration of this particular object; the densities and ionising spectrum from the UV line emitting region(s) are required to have an accurate analysis of abundances. Contrary to stars, these are not well known in accreting binary systems. However, the relative strength of UV emission lines can serve as a proxy to determine the presence

[4]http://mesa.sourceforge.net

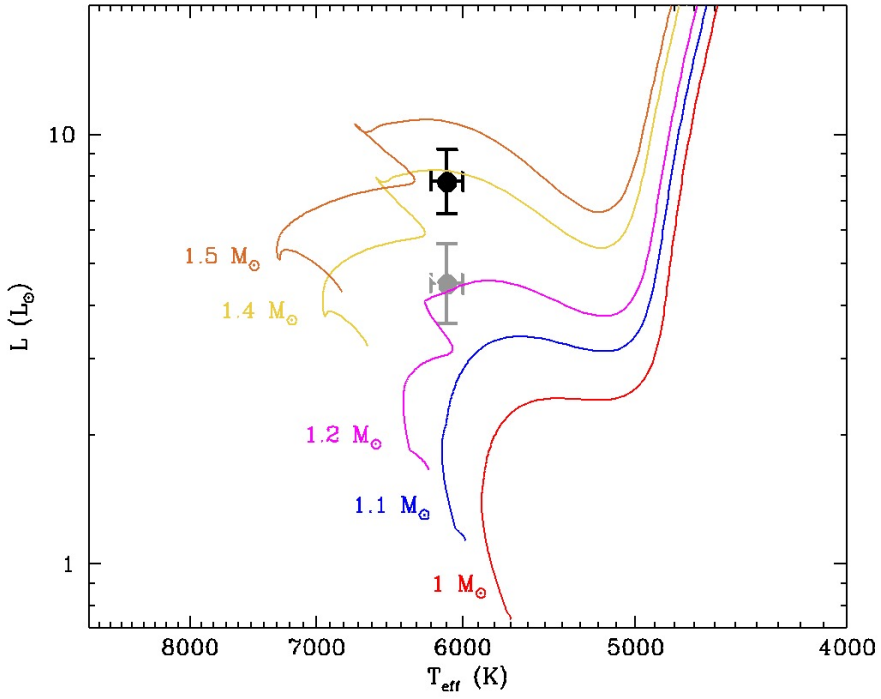

FIGURE 5.4: Hertzsprung–Russell diagram of the quiescent counterpart of the X-ray nova *Swift J1858.6−0814* assuming distances at $d = 9.8$ kpc in grey and $d = 12.8$ kpc in black. The evolutionary tracks for isolated stars represented with solid lines suggest a fairly massive evolved donor star.

of CNO-processed material from the atmosphere of the companion star (e.g. Haswell et al., 2002; Gänsicke et al., 2003; Froning et al., 2011, 2014).

The UV line ratios in the far-UV spectrum of J1858 are presented in Figure 5.5, along with those of other LMXBs and CVs. Most of the CVs in this figure harbour a (roughly) main-sequence donor star, and mass-transfer is driven by AML (black dots). However, the few systems with anomalous abundances (blue dots) are thought to represent systems that came into contact with an initial mass ratio $q \geq 1$, resulting in a short phase of unstable thermal time-scale mass transfer (TTSMT), during which they may be detectable as super-soft X-ray binaries. During this process of violent mass transfer, the donor lose its envelope rapidly leading to an exposed CNO-processed convective core, in cases with a less massive donor it can rather end in mixture with the solar abundances from the envelope and the CNO-processed core (Schenker & King, 2002). Consequently, in their stage as "normal" CVs, these systems exhibit "anomalies" in their spectra (blue dots in Figure 5.5 Schenker & King, 2002). The famous object *AE Aqr* (grey circles) is the most extreme of these "anomalous" CVs. It is an intermediate polar and magnetic propeller system that is believed to have recently emerged from its super-soft X-ray binary phase (Schenker et al., 2002).

In *Swift J1858.6−0814* , N V is by far the most prominent emission line in the far-UV spectrum, followed by He II. By contrast, C IV is mainly in absorption. Si IV and

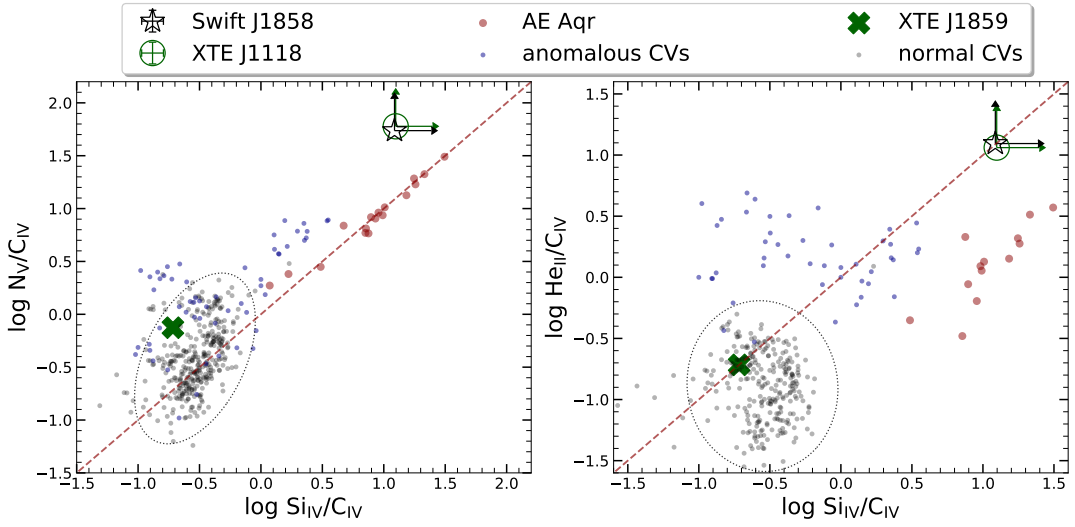

FIGURE 5.5: Far ultraviolet line flux ratios for CVs (dots) and LMXBs from Gänsicke et al. (2003) and Haswell et al. (2002) respectively. While most CVs accrete from near solar-abundances (grey dots encircled within the dotted lines), a set of WD accreting systems display anomalous line ratios (blue dots) indicating a CNO enhanced donor star. *XTE J1118* and *AE Aqr* display the most extreme line ratios, these are thought to be consequence of relatively high initial secondary masses, $M_{2,i} \gtrsim 1.5$. *Swift J1858.6−0814* (black star) has almost the same ratios than *XTE J1118*.

O v also appear to be present, although the detection of the latter is not statistically significant.

These line ratios are similar to *XTE J11118+480*, a system believed to host a $\sim 6M_{\odot}$ BH that is accreting CNO-processed material from its companion star. The CNO cycle can convert most of the ^{12}C into ^{14}N when it achieves equilibrium. However, to achieve the temperature required in the stellar interior to drive shell-burning CNO, the mass of such star must be $\gtrsim 1.5M_{\odot}$ (Clayton, 1983). This is broadly in line with the constraints on the donor obtained in the previous section.

5.2.3 Spectral energy distribution, intrinsic luminosity and mass accretion rate

In order to estimate the luminosity of the system, I constructed its time-averaged spectral energy distribution (Figure 5.7). It is important to note that the apparent deviations of the radio data points from a simple power law could be due to variability. The radio observations were not simultaneous, and the level of variability seen in the observations is of the same order as the scatter in the SED.

I found that the NIR photometry, optical and FUV spectroscopy were well aligned relative to each other, without any need for additional cross-calibration. However, the NUV spectroscopy was significantly fainter. The NUV was the last exposure obtained

with HST during this campaign, covering approximately the last 50 min of the 4h window. During this period, which occurred right after the brightest hard X-ray flare (a factor of 3 stronger than any other flare) seen during the campaign by *NuSTAR*, the trailed optical spectra (presented in Figure 3.7) exhibited the longest (the last $\sim$ 2ks) and deepest period of the Balmer jump absorption (increasing during this period up to $\gtrsim$ 20% from the continuum level at 3550Å, compared with the $\lesssim$ 10% exhibited during the rest of the observation) . For the purpose of SED construction, I therefore assumed that the NUV spectroscopy was affected by (grey) absorption and multiplied it by a factor of 5 to bring it in line with the far-UV and optical measurements. In order to avoid similar problems at X-ray wavelengths, I used overlapping *NuSTAR* and *NICER* exposures to construct the high energy end of the SED.

The resulting broad-band SED was fitted with the OPTXRPLIR accretion disc model, over the entire IR to X-ray range (Shidatsu et al., 2016). This model includes a hard X-ray emitting corona and an irradiated accretion disc. The fraction of the coronal emission that is intercepted by the disc depends on the geometry of the disc (its size and aspect ratio, H/R), while the fraction of the intercepted light that is then thermalised and re-emitted depends on the albedo. This model has been applied successfully to various LMXB transients (Kimura & Done, 2019; Oda et al., 2019; Tetarenko et al., 2020b). It has also been use as an input SED in radiation-hydrodynamic simulations (Higginbottom et al., 2020).

I carried out the SED fits in ISIS version 1.6.2-43 (Houck & Denicola, 2000). The extinction computed previously was used, and an extra column density component acting only in the x-ray was allowed to account for obscuration of the inner regions. The inclination was constrained to be $i > 70^o$ (required by the presence of eclipses in the light curve Buisson et al., 2021), and the distance was constrained as discussed in the previous section. A blackbody representing the donor, with the effective temperature determined previously, was also included in the fit.

I find that this model fails to simultaneously reproduce both the X-ray and the optical/UV regions (see Figure 5.6). The fundamental issue is that, for reasonable disc parameters (size, aspect ratio and albedo), the X-ray luminosity required to produce the observed optical/UV flux is close to the Eddington limit. Yet the X-ray luminosity inferred directly from the SED is "only" $L_X \simeq 0.1 L_{edd}$.

As already noted in Section 5.1, the strong variability of *Swift J1858.6−0814* in the hard state is reminiscent of some BH-LMXBs (e.g. V404 Cygni), where it is thought to be a signature of accretion taking place at (super-)Eddington rates (e.g. Motta et al., 2017a,b). This similarity thus strengthens the argument that the intrinsic luminosity may be close to L_{Edd}. If this is correct, the observed X-ray emission must either be highly anisotropic and/or suppressed by some form of absorption/obscuration.

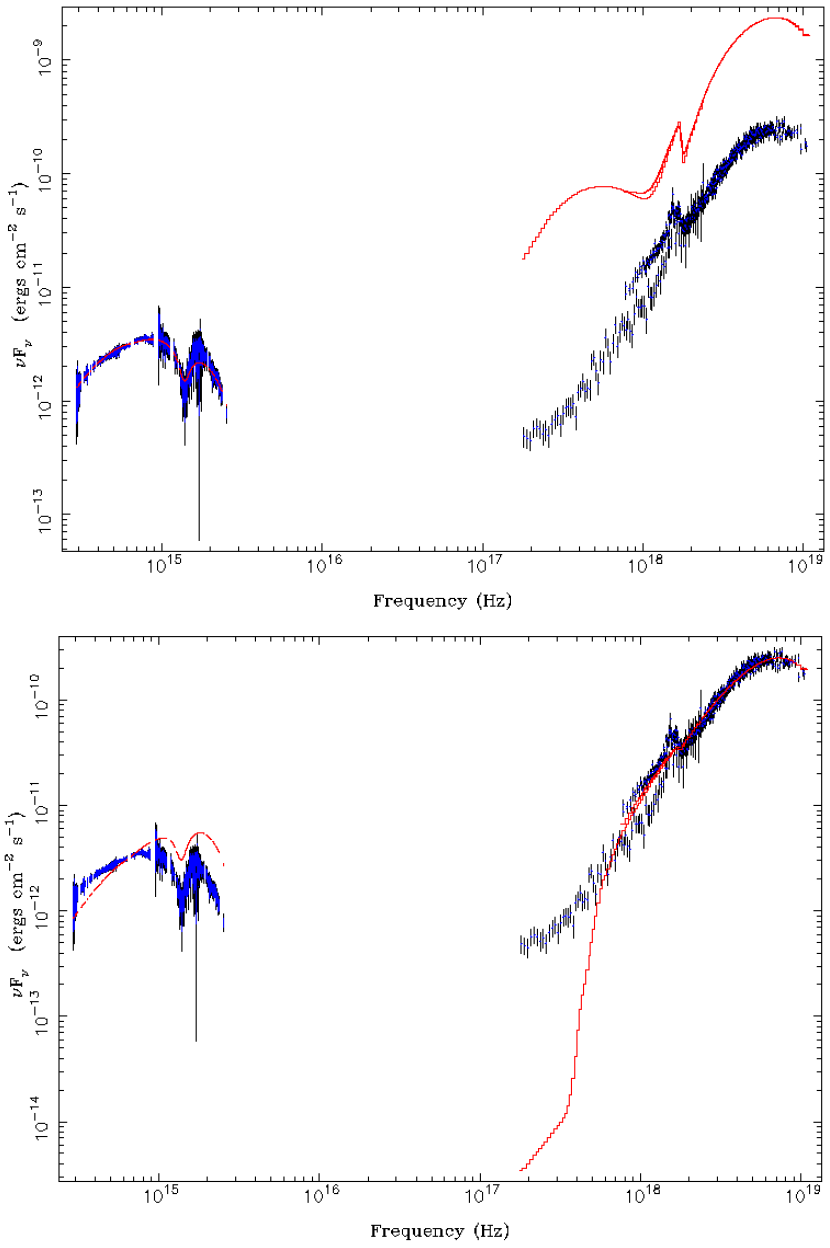

FIGURE 5.6: Example of SED fits for *Swift J1858.6−0814* . All the optical, UV and X-ray lines have been masked for the fit. The data is displayed with blue crosses and has not been corrected for absorption, instead the absorption is applied to the model (red line). **Top:** in this example the model is fitted to the optical/UV region using reasonable parameters for the X-ray component (e.g. Kimura & Done, 2019; Hare et al., 2020; Tetarenko et al., 2020b). **Bottom:** attempt to fit the entire SED

5.2.3.1 Luminosity constraints from the inferred EUV emission

In order to gain further insight, I can use the He II line to obtain a rough lower limit on the unobservable EUV luminosity (e.g. Patterson & Raymond, 1985; Marsh et al., 1994; Hynes et al., 1998; Dubus et al., 2001). For this, I have to assume that the He II λ1640 and λ4686 lines are produced as part of the recombination cascade of He II ions that were photoionised by EUV photons in the 55-280 eV range. The He II line ratio,

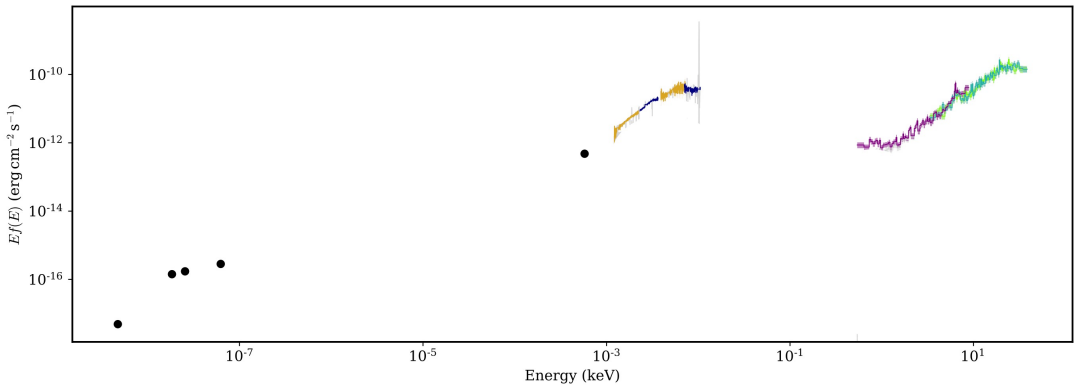

FIGURE 5.7: Spectral energy distribution of *Swift J1858.6−0814* . All the data are taken during the same time window with exception of both ends of the radio bands.

$F_{\lambda 1640}/F_{\lambda 4686} \sim 4$, is roughly in agreement with the value of $\simeq 7$ expected for case B of recombination (Seaton, 1978). In this case, a fraction of $\epsilon \simeq 0.2$ of recombinations produce He II λ4686 photons (Hummer & Storey, 1987). Following Dubus et al. (2001), I now assume that the fraction of photoionising photons that end up causing photoionisation is $\alpha \sim 0.03$. I then have

$$\epsilon\alpha\frac{F_{EUV}}{E_{EUV}} = \frac{F_{\lambda 4686}}{E_{\lambda 4686}}, \tag{5.1}$$

where E is the energy. Based on the average He II (λ4686) line flux, $F_{\lambda 4686} \simeq 1.5 \times 10^{-14}$ergs s^{-1} cm^{-2}, I therefore estimate that the unobserved EUV flux is on the order of a few $\times 10^{-9}$erg s^{-1} cm^{-2}. This is a very crude estimate, since the line exhibits variability by about a factor of two, and I have not accounted for anisotropic emission or other geometrical effects (such as the accretion disc occulting some of the emitting region). Nevertheless, it provides us with valuable information.

Our order-of-magnitude estimate of the EUV flux turns out to be comparable to the flux observed in the far-UV region, but $\simeq 10x$ higher than the flux observed in the soft X-ray regime (see Figure 5.7). The strength of the He II lines therefore also favours a scenario in which the source is accreting at near- or super-Eddington rates.

5.3 Discussion

As noted previously, *Swift J1858.6−0814* has relatively well-constrained system parameters, which makes it an ideal laboratory for many aspects of LMXB physics. All the evidence presented in Section 5.2.2 points to a fairly massive companion star. In particular, its position on the HRD suggests a slightly evolved sub-giant star with $M_2 \simeq 1.4\ M_\odot$ emerging from the main sequence with a stellar radius of $\sim 2R_\odot$, (in line with the

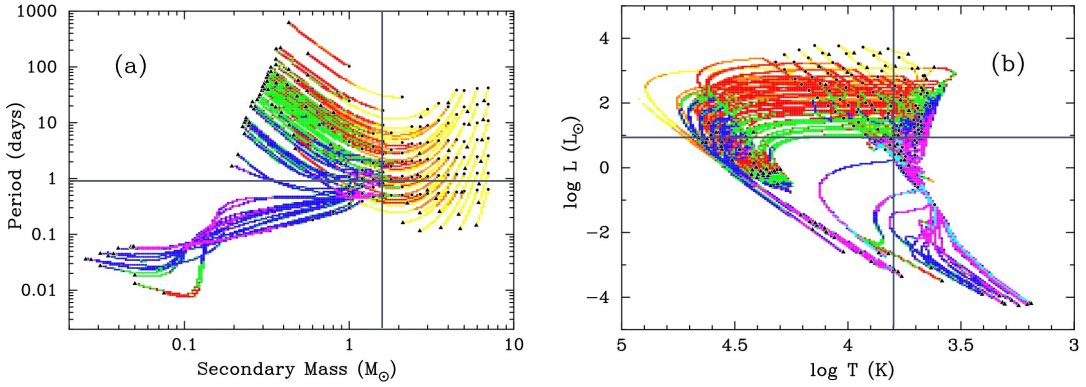

FIGURE 5.8: Evolutionary tracks for 100 binary sequences in the P_{orb} vs M_2 and L_2 vs $T_{eff,2}$ planes. Initial secondary masses ranging from $0.6M_\odot$ to $7M_\odot$ and initial binary periods from 4 hr to 100 d. The colour of the tracks indicate how much time the systems spend in a given rectangular pixel (from short to long: yellow, orange, red, green, blue, magenta, cyan). The seven colours are distributed evenly in $\log t$ between the minimum and maximum time displayed are 100 yr and 9.5 Gyr. Circles and triangles mark the starting and final points in the sequences, respectively. The estimated parameters for *Swift J1858.6−0814* are indicated with solid lines in both plots. Adapted from Podsiadlowski et al. (2002)

period-density relation given its orbital period). The evidence for CNO-processing revealed by the UV spectral line ratios also favours a donor with $M_2 \gtrsim 1.5M_\odot$.

The donor properties and orbital period place *Swift J1858.6−0814* in an interesting part of the binary evolution parameter space. This is illustrated in Figure 5.8, which shows a set of low- and intermediate-mass X-ray binary evolution tracks in both the P_{orb} vs M_2 and L_2 vs $T_{eff,2}$ planes (Podsiadlowski et al., 2002).

Several interesting features are immediately worth noting. First, the orbital period of $P_{orb} \simeq 21$ hrs places *Swift J1858.6−0814* near the so-called "bifurcation period" that separates binaries evolving towards either longer or shorter orbital periods. Second, *Swift J1858.6−0814* falls in a region of parameter space where (some) of the evolutionary sequence spend a lot of time (magenta and cyan points) – i.e. a region where systems *should* be detected. Third, there are two distinct types of tracks passing through the location of *Swift J1858.6−0814* , corresponding to two different evolutionary scenarios. They are distinguished most easily by the direction of their period evolution relative to the bifurcation period.

These two possible evolutionary scenarios are dictated by the initial mass ratio at which the binary came into contact with its Roche lobe. In the first scenario, the donor is initially more massive than the accretor. If the Roche lobe radius is less than the thermal equilibrium radius of the secondary, the star can no longer stay in thermal equilibrium and mass transfer will proceed on a TTSMT until the system reach $q \lesssim 1$. In this process the donor will lose rapidly the low density envelope and the convective core will

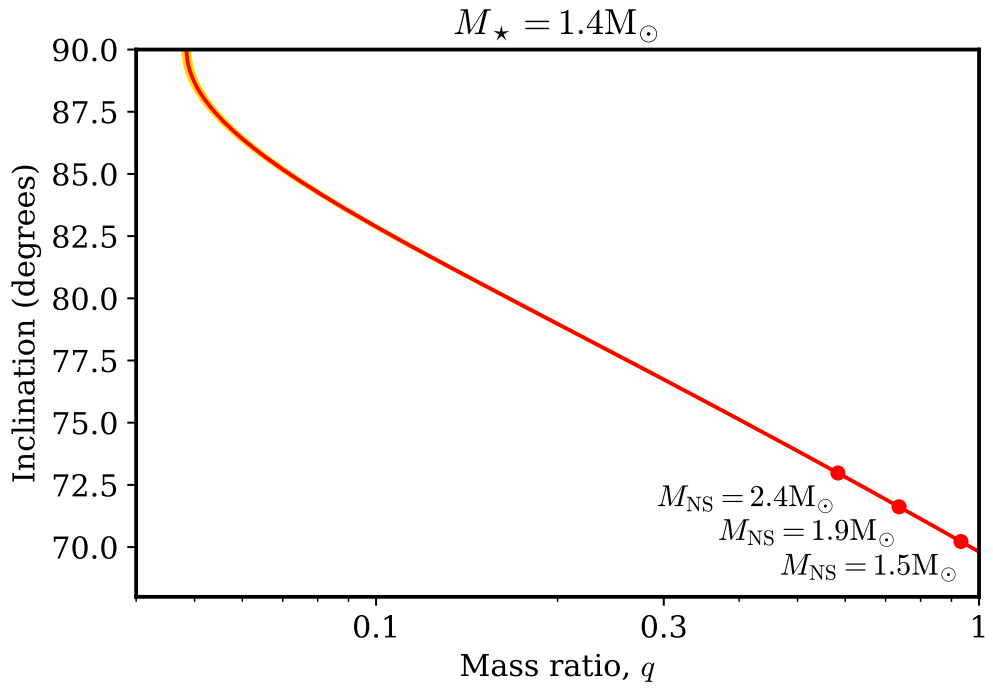

FIGURE 5.9: Inclination of the system as a function of the mass ratio. Allowed values given the orbital period of the system ($P_{orb} \sim 21h$; Buisson et al., 2021), are shown with the red line uncertainty is indicated with the shaded yellow region. Red dots indicate the values for different neutron star masses (M_{NS}) for a companion star with $M_* = 1.4M_\odot$

be exposed. After the TTSMT the system will evolve towards longer orbital periods ending its evolution as a detached system.

In the second scenario, AML brings the system into contact a system with initial mass ratio $q \lesssim 1$. In this track is similar to the classical evolution as of CVs, i.e. the AML drives the system towards shorter orbital periods.

The presence of CNO-processed material favours the first scenario. However, there is no strong evidences of Hydrogen depletion in the accreted material, e.g. the Type I X-ray bursts are not Helium rich (Buisson et al., 2020a). Hence the mass ratio was not extreme and significant fraction of the original envelope is mixed with the CNO-processed convective core (Schenker & King, 2002), and the companion star was likely only mildly evolved (Podsiadlowski et al., 2002). The orbital period, radius of the star and the presence of CNO-processed material are very similar to the binary sequence where the secondary has an initial mass of $2.1M_\odot$ and fills its Roche lobe on the main sequence (when $X_c = 0.489$; Figure 10 in Podsiadlowski et al., 2002). We conclude *Swift J1858.6−0814* came into contact with a $\gtrsim 2.1$ secondary star suffering a TTSMT which led to the present observational appearance and the system will evolve toward longer orbital period.

Independently of the evolutionary path leading to the current state of J1858, the constraints on the companion star mass allow us to set further limits on the inclination of the system. The presence of eclipses (Buisson et al., 2021) already indicates a high inclination. Assuming a circular orbit, the Roche geometry for the given eclipse width estimated by Buisson et al. (2021) allows to cast the mass ratio as a function of the inclination, $q(i)$ (see Figure 5.9; Joss & Rappaport, 1984; Eggleton, 1983).

Neutron stars have been observed to have masses up to $\lesssim 2.4 M_\odot$ (e.g. Page & Reddy, 2006). I therefore take $1.4 M_\odot < M_1 < 2.4 M_\odot$ as a reasonable range for the mass of the primary and adopt the range of allowed M_2 values derived in the previous section. The inclination implied by the observed eclipse width for this range of component masses is $70 \lesssim i \lesssim 74$. This relatively moderate inclination (for an eclipsing system) is consistent with the presence of blueshifted absorption lines in the spectrum, given that very high inclination are expected to produce pure emission profiles (if the wind has a nearly spherical geometry; Mauche & Raymond, 1987). Observing the radial velocity modulation with time resolved spectroscopy would constrain the mass of the neutron star.

5.3.1 Is *Swift J1858.6−0814* really a super-Eddington source?

I showed in Section 5.2.3 that a standard disc reprocessing model cannot simultaneously explain the observed X-ray and optical/UV flux levels. The observed X-ray luminosity is $\sim 10\% L_{edd}$, but, for a typical reprocessing efficiency, the optical/UV luminosities require the luminosity of the irradiating source to be $\gtrsim L_{Edd}$.

It is important to understand that this conclusion does not depend on the details of the model. In fact, it is immediately apparent directly from the SED (Figure 5.7). This shows that we are detecting almost the same power in the optical and X-ray bands. If the optical light is dominated by reprocessed X-ray emission, the radiation geometries are not extreme, and we have an unobscured view of both X-ray and optical emission region, this immediately implies that the accretion disc must reprocess about half of the X-ray luminosity. This is highly improbable.

The simplest explanation is that we do not have an unobscured view of the X-ray emitting region. This is quite plausible. First, the strong outflows we have observed in this system may obstruct our line of sight towards the inner disc and corona, at least to some extent. Second, if the mass accretion rate is high enough, radiation pressure may puff up the inner disc (e.g. Motta et al., 2017b). Given the high inclination of the system, this, too, may obscure our view of the central engine. In any case, the unusually low X-ray to optical ratio, as well as the extreme flaring displayed by the system (Motta et al., 2017a; Kimura et al., 2016), suggest that the intrinsic luminosity is at or above the Eddington limit.

Chapter 6

Summary and Future Work

The overarching goal of the projects described in this thesis is shed multi-wavelength light on the accretion flows in, the outflows from and the evolution of accreting compact binaries. In this Chapter, I will summarise the main results and outline promising/planned directions for future work.

In Chapter 2, I presented the first comprehensive multi-wavelength study of the recently identified nova-like star (NL) *V341 Ara*. This included the detection of both negative super-humps and the super-orbital modulation of a tilted accretion disc that ultimately causes them. The eventual fading episodes in this source could be consequence of the disc instability model acting in a tilted disc, so that outbursts are confined to the outer disc, while the inner region of the disc remain in a fully ionised state. This suggests that *V341 Ara* might be the first NL counterpart of the so-called IW And DN stars.

In this chapter I also constrained the wind mass-loss rate of the system from the spatially resolved [OIII] emission produced by its bow-shock. Moreover, I suggested a possible association between V341 Ara and a "guest star" mentioned in Chinese historical records in AD1240. If this marks the date of the system's nova eruption, *V341 Ara* would be the oldest recovered nova of its class and an excellent laboratory for testing nova theory.

In Chapter 3, I presented an overview of a major multi-wavelength campaign, which I initiated and still lead, aimed to study the recently discovered LMXB *Swift J1858.6−0814* . This campaign covered the entire electromagnetic spectrum, from radio to X-ray including NIR, optical and ultraviolet. To achieve this, I involved some of the state-of-art observatories/instruments such as HST, VLT/X-Shooter and Hawk-I, GTC, Gemini-S, NuSTAR, NICER, VLA and MeerKAT. The gathered data include all the techniques commonly used to study these binaries, such as time resolved spectroscopy and high time resolution multi-band photometry. One of the key ingredients of the campaign

was the coordination of many of these observatories to obtain strictly simultaneous observations. The collected data reveals a extreme flaring activity across all bands, likely due to reprocessing of the X-ray emission in the outer disc. The LMXB was exhibiting mysterious NIR flares, a with apparently transient wind signatures.

Chapter 4 was focused on the detection and implications of accretion disc winds in the ultraviolet spectrum we obtained during the campaign. The discovery of ultraviolet signatures in a transient LMXB opens up a new observational window for the study of these outflows. They also show that significant part of the outflow must exist in a "warm", moderately ionised phase. This suggests, for example, that the X-ray (highly ionised/hot) and optical (weakly ionised/cool) wind signatures that have previously been seen do not necessarily have to be associated with completely different outflows (e.g. a magnetically driven wind from the inner disc and a thermally-driven wind from the outer disc). I also showed that the UV wind signatures in *Swift J1858.6−0814* are associated with the steady light from the system, rather than with the flares. Thus the outflow does not appear to be driven by whatever mechanism is responsible for the flares. On the other hand, it also shows how wind signatures can be masked by flaring emission, even if the outflow is present all the time. This is crucial for the correct interpretation of all wind signatures.

Finally, in Chapter 5, I discussed the intrinsic luminosity and evolutionary stage of *Swift J1858.6−0814* . More specifically, by using archival data, I inferred the spectral type of the companion star. This, combined with the $q(i)$ determined by Buisson et al. (2021) was used to further constrain the inclination of the system. I also used the far-UV spectroscopy to estimate the line ratios in order to infer if the system went through an episode of CNO-processing, this was used to discuss the secular evolution of the system. Finally, the broad-band SED was used to discuss the intrinsic luminosity of the *Swift J1858.6−0814* .

6.1 Future work

6.1.1 Calibrating disc wind models against observations

The most common method to determine the mass and energy budget of CV accretion disk winds is by modelling the wind-formed UV resonance lines (e.g. Knigge et al., 1995, 1997; Long & Knigge, 2002). However, this is based on parameterised kinematic models that depend on many free parameters, and it requires computationally expensive radiative transfer simulations.

As illustrated in Section 2.3.6.2, wind-driven bow-shocks can provide independent estimates of these quantities. Systems that exhibit such bow-shocks – like *V341 Ara*, *BZ*

Cam and *V1838 Aql* – are therefore crucial for testing and calibrating the estimates provided by spectral models.

In *V341 Ara*, specifically, the bow-shock suggests a kinetic wind luminosity of $L_w \simeq 10^{32}$ erg s^{-1} and yields limits on the mass-loss rate ($\dot{M}_w \lesssim 10^{-10}$ M$_\odot$ yr^{-1}) and terminal velocity ($v_w \gtrsim 1800$ km s^{-1}). These values of kinetic wind luminosity and wind mass-loss rate are similar to the ones obtained by Hollis et al. (1992) for *BZ Cam*. The obvious next step in this regard is to obtain UV spectroscopy of *V341 Ara*, so these constraints of both sources can be tested against spectral models of the wind-formed UV resonance lines.

6.1.2 Multi-wavelength observations of LMXBs

In the context of LMXBs, the next open question is whether the disc winds that are typically observed in X-rays during the soft state also produce signatures in other bands. And, more generally, how do these outflows evolve over the full course of an outburst, across all of the different spectral states observed in transient LMXBs.

In this context, Sánchez-Sierras & Muñoz-Darias (2020) recently reported what seems to be a blue shifted absorption signature superposed on the meta-stable lines of the Hydrogen Paschen series during the soft state of the BH-LMXB *MAXI 1820*. However, no X-ray wind signatures have been reported up to date on this source.

In order to make progress in this area, I have a program ready to be triggered with the aim of covering the two distinct spectral states of an erupting LMXB with simultaneous observations in HST, XMM and NICER along with observations from GTC and/or X-Shooter with collaborators from other institutions. This campaign will be complemented with radio monitoring by MeerKAT, AMI, ATCA and VLA. One of the key goals of this campaign is to observe how the various accretion flows and outflowing components react to the two distinct physical configurations. Finally, I started to prepare a similar program which aims to catch the state transition in real time, aiming to study these components when a binary system is transitioning from one physical configuration to another. But this is difficult to achieve, because spectral state transitions can be very fast and hard to predict. Thus coordinating different instruments to observe such a transition simultaneously is very challenging.

Finally, my collaborators and I are trying to study persistent NS-LMXBs within a range of orbital periods and luminosities, with the aim to identify whether or not short-period systems (where thermally driven winds cannot take place) exhibit outflow signature or not. This will allow us to determine whether there is a need to invoke magnetically driven winds. Additionally, this campaign will allow us to study the evolution of these objects and populate Figure 5.5.

Bibliography

Abbott, B. P., Abbott, R., Abbott, T. D., et al. 2016, Phys. Rev. Lett., 116, 061102

—. 2017, Phys. Rev. Lett., 119, 161101

Abbott, D. C. 1982, ApJ, 263, 723

Allard, F. 2016, in SF2A-2016: Proceedings of the Annual meeting of the French Society of Astronomy and Astrophysics, ed. C. Reylé, J. Richard, L. Cambrésy, M. Deleuil, E. Pécontal, L. Tresse, & I. Vauglin, 223–227

Allen, J. L., Schulz, N. S., Homan, J., et al. 2018, ApJ, 861, 26

Alston, W. N., Markeviciute, J., Kara, E., Fabian, A. C., & Middleton, M. 2014, MNRAS, 445, L16

Aranzana, E., Scaringi, S., Körding, E., Dhillon, V. S., & Coppejans, D. L. 2018, MNRAS, 481, 2140

Armitage, P. J. 2011, ARA&A, 49, 195

Arzamasskiy, L., & Rafikov, R. R. 2018, ApJ, 854, 84

Ashman, K. M., Bird, C. M., & Zepf, S. E. 1994, AJ, 108, 2348

Baglio, M. C., Russell, D. M., Pirbhoy, S., et al. 2018, The Astronomer's Telegram, 12180, 1

Balbus, S. A., & Hawley, J. F. 1991, ApJ, 376, 214

Balsara, D. S., Fisker, J. L., Godon, P., & Sion, E. M. 2009, ApJ, 702, 1536

Baptista, R., Silveira, C., Steiner, J. E., & Horne, K. 2000, MNRAS, 314, 713

Barrett, P., O'Donoghue, D., & Warner, B. 1988, MNRAS, 233, 759

Bayless, A. J., Robinson, E. L., Hynes, R. I., Ashcraft, T. A., & Cornell, M. E. 2010, ApJ, 709, 251

Begelman, M. C., McKee, C. F., & Shields, G. A. 1983, Begelman, 271, 70

Belloni, T., Psaltis, D., & van der Klis, M. 2002, ApJ, 572, 392

Belloni, T. M. 2010, States and Transitions in Black Hole Binaries, ed. T. Belloni, Vol. 794, 53

Berdnikov, L. N., & Szabados, L. 1998, Acta Astron., 48, 763

Bertin, E. 2011, in Astronomical Society of the Pacific Conference Series, Vol. 442, Astronomical Data Analysis Software and Systems XX, ed. I. N. Evans, A. Accomazzi, D. J. Mink, & A. H. Rots, 435

Bertin, E., & Arnouts, S. 1996, A&AS, 117, 393

Beuermann, K., Stasiewski, U., & Schwope, A. D. 1992, A&A, 256, 433

Beuermann, K., & Thomas, H. C. 1990, A&A, 230, 326

Blandford, R. D., & Payne, D. G. 1982, MNRAS, 199, 883

Boehm-Vitense, E. 1989, Introduction to Stellar Astrophysics. Vol.1: Basic stellar observations and data; Vol.2: Stellar atmospheres

Bond, H. E., & Miszalski, B. 2018, PASP, 130, 094201

Bovy, J. 2015, ApJS, 216, 29

Bright, J. S., Fender, R. P., Motta, S. E., et al. 2020, Nature Astronomy, 4, 697

Buisson, D. J. K., Altamirano, D., Bult, P., et al. 2020a, MNRAS, 499, 793

Buisson, D. J. K., Altamirano, D., Díaz Trigo, M., et al. 2020b, MNRAS, 498, 68

Buisson, D. J. K., Altamirano, D., Armas Padilla, M., et al. 2021, MNRAS, 503, 5600

Burrows, D. N., Hill, J. E., Nousek, J. A., et al. 2005, Space Sci. Rev., 120, 165

Cantrell, A. G., & Bailyn, C. D. 2007, ApJ, 670, 727

Cardelli, J. A., Clayton, G. C., & Mathis, J. S. 1989, ApJ, 345, 245

Carilli, C. L., Perley, R. A., & Harris, D. E. 1994, MNRAS, 270, 173

Casares, J., Cornelisse, R., Steeghs, D., et al. 2006, MNRAS, 373, 1235

Casares, J., & Jonker, P. G. 2014, Space Sci. Rev., 183, 223

Casares, J., Muñoz-Darias, T., Mata Sánchez, D., et al. 2019, MNRAS, 488, 1356

Castor, J. I., Abbott, D. C., & Klein, R. I. 1975, ApJ, 195, 157

Castor, J. L. 1974, MNRAS, 169, 279

Cepa, J., Aguiar, M., Escalera, V. G., et al. 2000, in Society of Photo-Optical Instrumentation Engineers (SPIE) Conference Series, Vol. 4008, Optical and IR Telescope Instrumentation and Detectors, ed. M. Iye & A. F. Moorwood, 623–631

Chabrier, G. 2003, PASP, 115, 763

Chambers, K. C., Magnier, E. A., Metcalfe, N., et al. 2016, arXiv e-prints, arXiv:1612.05560

Charles, P., Matthews, J. H., Buckley, D. A. H., et al. 2019, MNRAS, 489, L47

Chaty, S., Charles, P. A., Martí, J., et al. 2003, MNRAS, 343, 169

Cheng, F. H., Horne, K., Panagia, N., et al. 1992, ApJ, 397, 664

Clark, D. H., & Stephenson, F. R. 1976, QJRAS, 17, 290

Clayton, D. D. 1983, Principles of stellar evolution and nucleosynthesis (UCP)

Cohen, J. G., & Rosenthal, A. J. 1983, ApJ, 268, 689

Coleman, M. S. B., Kotko, I., Blaes, O., Lasota, J. P., & Hirose, S. 2016, MNRAS, 462, 3710

Coppejans, D. L., & Knigge, C. 2020, New A Rev., 89, 101540

Coppejans, D. L., Körding, E. G., Miller-Jones, J. C. A., et al. 2015, MNRAS, 451, 3801

Corbel, S., Fender, R. P., Tzioumis, A. K., et al. 2000, A&A, 359, 251

Cordova, F. A., & Mason, K. O. 1982, ApJ, 260, 716

Coriat, M., Fender, R. P., & Dubus, G. 2012, MNRAS, 424, 1991

Cornelisse, R., Heise, J., Kuulkers, E., Verbunt, F., & in't Zand, J. J. M. 2000, A&A, 357, L21

Crause, L. A., Sharples, R. M., Bramall, D. G., et al. 2014, Society of Photo-Optical Instrumentation Engineers (SPIE) Conference Series, Vol. 9147, Performance of the Southern African Large Telescope (SALT) High Resolution Spectrograph (HRS), 91476T

Crause, L. A., Carter, D., Daniels, A., et al. 2016, Society of Photo-Optical Instrumentation Engineers (SPIE) Conference Series, Vol. 9908, SpUpNIC (Spectrograph Upgrade: Newly Improved Cassegrain) on the South African Astronomical Observatory's 74-inch telescope, 990827

Cumming, A., & Bildsten, L. 2001, ApJ, 559, L127

Cutri, R. M., & et al. 2014, VizieR Online Data Catalog, II/328

Dallilar, Y., Eikenberry, S. S., Garner, A., et al. 2017, Science, 358, 1299

Damineli, A. 1996, ApJ, 460, L49

Darnley, M. J., Hounsell, R., O'Brien, T. J., et al. 2019, Nature, 565, 460

del Palacio, S., Bosch-Ramon, V., Müller, A. L., & Romero, G. E. 2018, A&A, 617, A13

Dhillon, V. S. 1990, PhD thesis, U. of Sussex

Dhillon, V. S., Smith, D. A., & Marsh, T. R. 2013, MNRAS, 428, 3559

Dhillon, V. S., Marsh, T. R., Stevenson, M. J., et al. 2007, MNRAS, 378, 825

Díaz Trigo, M., & Boirin, L. 2016, Astronomische Nachrichten, 337, 368

Done, C. 2010, arXiv e-prints, arXiv:1008.2287

Done, C., Gierliński, M., & Kubota, A. 2007, A&ARev, 15, 1

Done, C., Tomaru, R., & Takahashi, T. 2018a, MNRAS, 473, 838

—. 2018b, MNRAS, 473, 838

Dopita, M., Hart, J., McGregor, P., et al. 2007, Ap&SS, 310, 255

Dopita, M. A. 1977, ApJS, 33, 437

Downes, R. A., Duerbeck, H. W., & Delahodde, C. E. 2001, Journal of Astronomical Data, 7, 6

Drew, J. E. 1987, MNRAS, 224, 595

Dubus, G., Done, C., Tetarenko, B. E., & Hameury, J.-M. 2019, A&A, 632, A40

Dubus, G., Hameury, J. M., & Lasota, J. P. 2001, A&A, 373, 251

Dubus, G., Lasota, J.-P., Hameury, J.-M., & Charles, P. 1999, MNRAS, 303, 139

Dubus, G., Otulakowska-Hypka, M., & Lasota, J.-P. 2018, A&A, 617, A26

Duerbeck, H. W. 2003, Astronomical Society of the Pacific Conference Series, Vol. 292, Long-term evolution of nova shell and postnova luminosities, and the problem of nova recurrence times, ed. C. Sterken, 323

Duquennoy, A., & Mayor, M. 1991, A&A, 500, 337

Eastman, J., Siverd, R., & Gaudi, B. S. 2010, PASP, 122, 935

Eggleton, P. P. 1983, ApJ, 268, 368

El-Badry, K., Rix, H.-W., & Heintz, T. M. 2021, MNRAS, 506, 2269

El-Badry, K., Ting, Y.-S., Rix, H.-W., et al. 2018, MNRAS, 476, 528

El Mellah, I., Sundqvist, J. O., & Keppens, R. 2018, MNRAS, 475, 3240

Eracleous, M., & Horne, K. 1996, ApJ, 471, 427

Erben, T., Schirmer, M., Dietrich, J. P., et al. 2005, Astronomische Nachrichten, 326, 432

ESA, ed. 1997, ESA Special Publication, Vol. 1200, The HIPPARCOS and TYCHO catalogues. Astrometric and photometric star catalogues derived from the ESA HIPPARCOS Space Astrometry Mission, ed. ESA

Esin, A. A., Lasota, J. P., & Hynes, R. I. 2000, A&A, 354, 987

Esin, A. A., McClintock, J. E., & Narayan, R. 1997, ApJ, 489, 865

Fender, R., & Muñoz-Darias, T. 2016, The Balance of Power: Accretion and Feedback in Stellar Mass Black Holes, ed. F. Haardt, V. Gorini, U. Moschella, A. Treves, & M. Colpi, Vol. 905, 65

Fender, R., Wu, K., Johnston, H., et al. 2004a, Nature, 427, 222

Fender, R., Woudt, P. A., Armstrong, R., et al. 2017, arXiv e-prints, arXiv:1711.04132

Fender, R. P. 2001, MNRAS, 322, 31

Fender, R. P., Belloni, T. M., & Gallo, E. 2004b, MNRAS, 355, 1105

Fernández-Ontiveros, J. A., & Muñoz-Darias, T. 2021, MNRAS, 504, 5726

Figueira, J., José, J., García-Berro, E., et al. 2018, A&A, 613, A8

Fitzpatrick, E. L. 1999, PASP, 111, 63

Fitzpatrick, E. L., & Massa, D. 1990, ApJS, 72, 163

Flannery, B. P. 1975, MNRAS, 170, 325

Flewelling, H. A., Magnier, E. A., Chambers, K. C., et al. 2020, ApJS, 251, 7

Foreman-Mackey, D., Hogg, D. W., Lang, D., & Goodman, J. 2013, PASP, 125, 306

Frank, J., King, A., & Raine, D. J. 2002, Accretion Power in Astrophysics: Third Edition (CUP)

Freudling, W., Romaniello, M., Bramich, D. M., et al. 2013, A&A, 559, A96

Frew, D. J. 2008, PhD thesis, Department of Physics, Macquarie University, NSW 2109, Australia

Friend, D. B., & Abbott, D. C. 1986, ApJ, 311, 701

Froning, C. S., Maccarone, T. J., France, K., et al. 2014, ApJ, 780, 48

Froning, C. S., Cantrell, A. G., Maccarone, T. J., et al. 2011, ApJ, 743, 26

Fuhrmann, K., Chini, R., Kaderhandt, L., & Chen, Z. 2017, ApJ, 836, 139

Gaia Collaboration, Brown, A. G. A., Vallenari, A., et al. 2018, A&A, 616, A1

Gallo, E., Fender, R., Kaiser, C., et al. 2005, Nature, 436, 819

Gandhi, P., Bachetti, M., Dhillon, V. S., et al. 2017, Nature Astronomy, 1, 859

Ganguly, S., & Proga, D. 2020, ApJ, 890, 54

Gänsicke, B. T., Szkody, P., de Martino, D., et al. 2003, ApJ, 594, 443

Gaustad, J. E., McCullough, P. R., Rosing, W., & Van Buren, D. 2001, PASP, 113, 1326

Gayley, K. G. 1995, ApJ, 454, 410

Gendreau, K. C., Arzoumanian, Z., Adkins, P. W., et al. 2016, in Society of Photo-Optical Instrumentation Engineers (SPIE) Conference Series, Vol. 9905, Space Telescopes and Instrumentation 2016: Ultraviolet to Gamma Ray, ed. J.-W. A. den Herder, T. Takahashi, & M. Bautz, 99051H

Ghosh, P., & Lamb, F. K. 1979, ApJ, 234, 296

Gilmore, G., & Reid, N. 1983, MNRAS, 202, 1025

González Martínez-País, I., Shahbaz, T., & Casares Velázquez, J. 2014, Accretion Processes in Astrophysics, ed. CUP

Goodman, J., & Weare, J. 2010, Communications in Applied Mathematics and Computational Science, 5, 65

Göttgens, F., Weilbacher, P. M., Roth, M. M., et al. 2019, A&A, 626, A69

Green, D. A., & Stephenson, F. R. 2003, Historical Supernovae, ed. K. Weiler, Vol. 598, 7–19

Green, J. C., Froning, C. S., Osterman, S., et al. 2012, ApJ, 744, 60

Greenstein, J. L., & Oke, J. B. 1982, ApJ, 258, 209

Greiner, J., Bornemann, W., Clemens, C., et al. 2008, PASP, 120, 405

Grindlay, J., Gursky, H., Schnopper, H., et al. 1976, ApJ, 205, L127

Guerrero, M. A., Sabin, L., Tovmassian, G., et al. 2018, ApJ, 857, 80

Gull, T. R., & Sofia, S. 1979, ApJ, 230, 782

Hameury, J. M. 2020, Advances in Space Research, 66, 1004

Hameury, J. M., Lasota, J. P., Knigge, C., & Körding, E. G. 2017, A&A, 600, A95

Hare, J., Tomsick, J. A., Buisson, D. J. K., et al. 2020, ApJ, 890, 57

Harrison, F. A., Craig, W. W., Christensen, F. E., et al. 2013, ApJ, 770, 103

Harvey, D., Skillman, D. R., Patterson, J., & Ringwald, F. A. 1995, PASP, 107, 551

Haswell, C. A., Hynes, R. I., King, A. R., & Schenker, K. 2002, MNRAS, 332, 928

Hazard, C., Mackey, M. B., & Shimmins, A. J. 1963, Nature, 197, 1037

Heap, S. R., Boggess, A., Holm, A., et al. 1978, Nature, 275, 385

Hellier, C. 2001, Cataclysmic Variable Stars (Springer)

Henden, A. A., Templeton, M., Terrell, D., et al. 2016, VizieR Online Data Catalog, II/336

Hernandez Santisteban, J. V. 2016, PhD thesis, U. of Southampton

Hernández Santisteban, J. V., Knigge, C., Littlefair, S. P., et al. 2016, Nature, 533, 366

Hernández Santisteban, J. V., Echevarría, J., Zharikov, S., et al. 2019a, MNRAS, 486, 2631

—. 2019b, MNRAS, 486, 2631

Hertfelder, M., Kley, W., Suleimanov, V., & Werner, K. 2013, A&A, 560, A56

Hewitt, D. M., Pretorius, M. L., Woudt, P. A., et al. 2020, MNRAS, 496, 2542

Heywood, I. 2020, oxkat: Semi-automated imaging of MeerKAT observations, ascl:2009.003

Hickish, J., Razavi-Ghods, N., Perrott, Y. C., et al. 2018, MNRAS, 475, 5677

Higginbottom, N., Knigge, C., Sim, S. A., et al. 2020, MNRAS, 492, 5271

Higginbottom, N., & Proga, D. 2015, ApJ, 807, 107

Hirose, S., Blaes, O., Krolik, J. H., Coleman, M. S. B., & Sano, T. 2014, ApJ, 787, 1

Hjellming, M. S. 1989, PhD thesis, Illinois Univ. at Urbana-Champaign, Savoy.

Hoffman, J. A., Marshall, H. L., & Lewin, W. H. G. 1978, Nature, 271, 630

Hoffmann, S. M., Vogt, N., & Protte, P. 2020, Astronomische Nachrichten, 341, 79

Hoffmeister, C. 1956, Veroeffentlichungen der Sternwarte Sonneberg, 3, 1

Holberg, J. B., & Bergeron, P. 2006, AJ, 132, 1221

Hollis, J. M., Oliversen, R. J., Wagner, R. M., & Feibelman, W. A. 1992, ApJ, 393, 217

Homer, L., Anderson, S. F., Wachter, S., & Margon, B. 2002, AJ, 124, 3348

Horne, K. 1985, MNRAS, 213, 129

Horne, K., & Marsh, T. R. 1986, MNRAS, 218, 761

Houck, J. C., & Denicola, L. A. 2000, in Astronomical Society of the Pacific Conference Series, Vol. 216, Astronomical Data Analysis Software and Systems IX, ed. N. Manset, C. Veillet, & D. Crabtree, 591

Howarth, I. D., & Prinja, R. K. 1989, ApJS, 69, 527

Hubeny, I., & Long, K. S. 2021, MNRAS, 503, 5534

Hummer, D. G., & Storey, P. J. 1987, MNRAS, 224, 801

Hynes, R. I. 2010, arXiv e-prints, arXiv:1010.5770

Hynes, R. I., Haswell, C. A., Chaty, S., Shrader, C. R., & Cui, W. 2002, MNRAS, 331, 169

Hynes, R. I., Haswell, C. A., Shrader, C. R., et al. 1998, MNRAS, 300, 64

Iben, Icko, J. 1991, ApJS, 76, 55

Ioannou, Z., van Zyl, L., Naylor, T., et al. 2003, A&A, 399, 211

Ivanova, N., Justham, S., Chen, X., et al. 2013, A&ARev, 21, 59

Jenkins, J. M., Twicken, J. D., McCauliff, S., et al. 2016, Society of Photo-Optical Instrumentation Engineers (SPIE) Conference Series, Vol. 9913, The TESS science processing operations center, 99133E

Jonas, J. L. 2009, IEEE Proceedings, 97, 1522

José, J., Shore, S. N., & Casanova, J. 2020, A&A, 634, A5

Joss, P. C., & Rappaport, S. A. 1984, ARA&A, 22, 537

Ju, W., Stone, J. M., & Zhu, Z. 2016, ApJ, 823, 81

Kafka, S., & Honeycutt, R. K. 2004, AJ, 128, 2420

Kahabka, P., & van den Heuvel, E. P. J. 1997, ARA&A, 35, 69

Kato, M., Hachisu, I., & Saio, H. 2017, in The Golden Age of Cataclysmic Variables and Related Objects IV, 56

Kato, M., Saio, H., Hachisu, I., & Nomoto, K. 2014, ApJ, 793, 136

Kato, T. 2019, PASJ, 71, 20

Kimura, M., & Done, C. 2019, MNRAS, 482, 626

Kimura, M., Osaki, Y., Kato, T., & Mineshige, S. 2020, PASJ, 72, 22

Kimura, M., Isogai, K., Kato, T., et al. 2016, Nature, 529, 54

King, A. R. 1988, QJRAS, 29, 1

King, A. R., & Ritter, H. 1998, MNRAS, 293, L42

Kiraga, M. 2012, Acta Astron., 62, 67

Kluźniak, W., & Rappaport, S. 2007, ApJ, 671, 1990

Knigge, C. 1995, PhD thesis, U. of Oxford

—. 1999, MNRAS, 309, 409

—. 2006, MNRAS, 373, 484

Knigge, C., Baraffe, I., & Patterson, J. 2011, ApJS, 194, 28

Knigge, C., Dieball, A., Maíz Apellániz, J., et al. 2008a, ApJ, 683, 1006

Knigge, C., Long, K. S., Blair, W. P., & Wade, R. A. 1997, ApJ, 476, 291

Knigge, C., Scaringi, S., Goad, M. R., & Cottis, C. E. 2008b, MNRAS, 386, 1426

Knigge, C., Woods, J. A., & Drew, J. E. 1995, MNRAS, 273, 225

Kobulnicky, H. A., Chick, W. T., & Povich, M. S. 2018, ApJ, 856, 74

Kochanek, C. S., Shappee, B. J., Stanek, K. Z., et al. 2017, PASP, 129, 104502

Kopal, Z. 1978, Dynamics of close binary systems (ASSL)

Körding, E., Rupen, M., Knigge, C., et al. 2008, Science, 320, 1318

Kosenkov, I. A., & Veledina, A. 2018, MNRAS, 478, 4710

Kraft, R. P. 1967, ApJ, 150, 551

Kroupa, P. 2001, MNRAS, 322, 231

Krühler, T., Küpcü Yoldaş, A., Greiner, J., et al. 2008, ApJ, 685, 376

Kuin, N. P. M., Landsman, W., Breeveld, A. A., et al. 2015, MNRAS, 449, 2514

Kuin, P. 2014, UVOTPY: Swift UVOT grism data reduction, ascl:1410.004

Kuulkers, E., den Hartog, P. R., in't Zand, J. J. M., et al. 2003, A&A, 399, 663

Lamers, H. J. G. L. M., & Cassinelli, J. P. 1999, Introduction to Stellar Winds (CUP)

Landau, L. D., & Lifshitz, E. M. ????, The classical theory of fields (Pergamon)

Lasota, J.-P. 2001, New A Rev., 45, 449

—. 2016, Astrophysics and Space Science Library, Vol. 440, Black Hole Accretion Discs, ed. C. Bambi, 1

Lasota, J. P., Abramowicz, M. A., Chen, X., et al. 1996, ApJ, 462, 142

Leavitt, H. S., & Pickering, E. C. 1907, Harvard College Observatory Circular, 130, 1

Ledden, J. E., Aller, H. D., & Dent, W. A. 1976, Nature, 260, 752

Leonard, P. J. T. 1989, AJ, 98, 217

Lewin, W. H. G., van Paradijs, J., & Taam, R. E. 1993, Space Sci. Rev., 62, 223

Lin, Y. F., Yu, P. C., Huang, J. C., et al. 2016, VizieR Online Data Catalog, J/A+A/600/A28

Lomb, N. R. 1976, Ap&SS, 39, 447

Long, K. S., & Knigge, C. 2002, ApJ, 579, 725

Longair, M. S. 2011, High Energy Astrophysics (CUP)

Lubow, S. H., & Shu, F. H. 1975, ApJ, 198, 383

Lucy, L. B., & Solomon, P. M. 1970, ApJ, 159, 879

Ludlam, R. M., Miller, J. M., Arzoumanian, Z., et al. 2018, The Astronomer's Telegram, 12158, 1

Luketic, S., Proga, D., Kallman, T. R., Raymond, J. C., & Miller, J. M. 2010, ApJ, 719, 515

Luri, X., Brown, A. G. A., Sarro, L. M., et al. 2018, A&A, 616, A9

Malzac, J. 2014, MNRAS, 443, 299

Marcel, G., Ferreira, J., Petrucci, P. O., et al. 2022, A&A, 659, A194

Markoff, S., Nowak, M. A., & Wilms, J. 2005, ApJ, 635, 1203

Marsh, T. R., & Horne, K. 1988, MNRAS, 235, 269

Marsh, T. R., Nelemans, G., & Steeghs, D. 2004, MNRAS, 350, 113

Marsh, T. R., Robinson, E. L., & Wood, J. H. 1994, MNRAS, 266, 137

Mata Sánchez, D., Muñoz-Darias, T., Casares, J., et al. 2018, MNRAS, 481, 2646

Matthews, J. H., Knigge, C., Long, K. S., Sim, S. A., & Higginbottom, N. 2015, MNRAS, 450, 3331

Mauche, C. W. 2004a, in Revista Mexicana de Astronomia y Astrofisica Conference Series, Vol. 20, Revista Mexicana de Astronomia y Astrofisica Conference Series, ed. G. Tovmassian & E. Sion, 174

Mauche, C. W. 2004b, ApJ, 610, 422

Mauche, C. W. 2004c, in American Institute of Physics Conference Series, Vol. 714, X-ray Timing 2003: Rossi and Beyond, ed. P. Kaaret, F. K. Lamb, & J. H. Swank, 315–322

Mauche, C. W., & Raymond, J. C. 1987, ApJ, 323, 690

McHardy, I. M., Koerding, E., Knigge, C., Uttley, P., & Fender, R. P. 2006, Nature, 444, 730

McMahon, R., G., Banerji, et al. 2019, VizieR Online Data Catalog, II/359

McMullin, J. P., Waters, B., Schiebel, D., Young, W., & Golap, K. 2007, Astronomical Society of the Pacific Conference Series, Vol. 376, CASA Architecture and Applications, ed. R. A. Shaw, F. Hill, & D. J. Bell, 127

Meyer, D. M. A., van Marle, A. J., Kuiper, R., & Kley, W. 2016, MNRAS, 459, 1146

Meyer, F., & Meyer-Hofmeister, E. 1994, A&A, 288, 175

Mihalas, D. M. 1978, Stellar atmospheres. (W.H. Freeman)

Mikołajewska, J. 2007, Baltic Astronomy, 16, 1

Miller, J. M., Raymond, J., Fabian, A. C., et al. 2012, ApJ, 759, L6

Miller-Jones, J. C. A., Tetarenko, A. J., Sivakoff, G. R., et al. 2019, Nature, 569, 374

Mirabel, I. F., & Rodríguez, L. F. 1999, ARA&A, 37, 409

Miszalski, B., Woudt, P. A., Littlefair, S. P., et al. 2016, MNRAS, 456, 633

Montgomery, M. M. 2009, ApJ, 705, 603

Motta, S. E., Kajava, J. J. E., Sánchez-Fernández, C., Giustini, M., & Kuulkers, E. 2017a, MNRAS, 468, 981

Motta, S. E., Kajava, J. J. E., Sánchez-Fernández, C., et al. 2017b, MNRAS, 471, 1797

Muñoz-Darias, T., Casares, J., & Martínez-Pais, I. G. 2005, ApJ, 635, 502

Muñoz-Darias, T., Torres, M. A. P., & Garcia, M. R. 2018, MNRAS, 479, 3987

Muñoz-Darias, T., Casares, J., Mata Sánchez, D., et al. 2016, Nature, 534, 75

Muñoz-Darias, T., Jiménez-Ibarra, F., Panizo-Espinar, G., et al. 2019, ApJ, 879, L4

Muñoz-Darias, T., Armas Padilla, M., Jiménez-Ibarra, F., et al. 2020, ApJ, 893, L19

Mukai, K. 2017, PASP, 129, 062001

Mukai, K., & Patterson, J. 2004, in Revista Mexicana de Astronomia y Astrofisica Conference Series, Vol. 20, Revista Mexicana de Astronomia y Astrofisica Conference Series, ed. G. Tovmassian & E. Sion, 244

Murray, N., & Chiang, J. 1996, Nature, 382, 789

Narayan, R., & Heyl, J. S. 2003, ApJ, 599, 419

Narayan, R., & McClintock, J. E. 2008, New A Rev., 51, 733

Neilsen, J., Homan, J., Steiner, J. F., et al. 2020, ApJ, 902, 152

Neilsen, J., & Lee, J. C. 2009, Nature, 458, 481

Oda, S., Shidatsu, M., Nakahira, S., et al. 2019, PASJ, 71, 108

O'Donoghue, D., & Charles, P. A. 1996, MNRAS, 282, 191

Offringa, A. R. 2010, AOFlagger: RFI Software, ascl:1010.017

Offringa, A. R., McKinley, B., Hurley-Walker, N., et al. 2014, MNRAS, 444, 606

Osaki, Y. 1971, PASJ, 23, 485

—. 2005, Proceedings of the Japan Academy, Series B, 81, 291

Owocki, S. P., Castor, J. I., & Rybicki, G. B. 1988, ApJ, 335, 914

Paczyński, B. 1971, ARA&A, 9, 183

Paczynski, B. 1976, in Structure and Evolution of Close Binary Systems, ed. P. Eggleton, S. Mitton, & J. Whelan, Vol. 73 (IAUS), 75

Page, D., & Reddy, S. 2006, Annual Review of Nuclear and Particle Science, 56, 327

Page, M. J., Kuin, N. P. M., Breeveld, A. A., et al. 2013, MNRAS, 436, 1684

Paice, J. A., Gandhi, P., Dhillon, V. S., et al. 2018, The Astronomer's Telegram, 12197, 1

Pala, A. F., Gänsicke, B. T., Breedt, E., et al. 2020, MNRAS, 494, 3799

Parker, E. N. 1955, ApJ, 121, 491

Patterson, J. ????, in Disk Instabilities in Close Binary Systems, ed. S. Mineshige & J. C. Wheeler (UAP), 61

Patterson, J. 1998, PASP, 110, 1132

Patterson, J., Patino, R., Thorstensen, J. R., et al. 1996, AJ, 111, 2422

Patterson, J., & Raymond, J. C. 1985, ApJ, 292, 550

Patterson, J., Kemp, J., Harvey, D. A., et al. 2005, PASP, 117, 1204

Patterson, J., Uthas, H., Kemp, J., et al. 2013, MNRAS, 434, 1902

Paxton, B., Bildsten, L., Dotter, A., et al. 2011, ApJS, 192, 3

Pelletier, G., & Pudritz, R. E. 1992, ApJ, 394, 117

Pepper, J., Kuhn, R. B., Siverd, R., James, D., & Stassun, K. 2012, PASP, 124, 230

Pepper, J., Stassun, K. G., & Gaudi, B. S. 2018, KELT: The Kilodegree Extremely Little Telescope, a Survey for Exoplanets Transiting Bright, Hot Stars, 128

Pepper, J., Pogge, R. W., DePoy, D. L., et al. 2007, PASP, 119, 923

Pereyra, N. A., Kallman, T. R., & Blondin, J. M. 1997, ApJ, 477, 368

Perrott, Y. C., Scaife, A. M. M., Green, D. A., et al. 2013, MNRAS, 429, 3330

Pirard, J.-F., Kissler-Patig, M., Moorwood, A., et al. 2004, in Society of Photo-Optical Instrumentation Engineers (SPIE) Conference Series, Vol. 5492, Ground-based Instrumentation for Astronomy, ed. A. F. M. Moorwood & M. Iye, 1763

Podsiadlowski, P., Rappaport, S., & Pfahl, E. D. 2002, ApJ, 565, 1107

Politano, M. 1996, ApJ, 465, 338

Ponti, G., Fender, R. P., Begelman, M. C., et al. 2012, MNRAS, 422, L11

Pounds, K. A., Lobban, A., Reeves, J. N., Vaughan, S., & Costa, M. 2016, MNRAS, 459, 4389

Pratt, G. W., Mukai, K., Hassall, B. J. M., Naylor, T., & Wood, J. H. 2004, MNRAS, 348, L49

Pretorius, M. L., Knigge, C., O'Donoghue, D., et al. 2007, MNRAS, 382, 1279

Pringle, J. E. 1981, ARA&A, 19, 137

Pringle, J. E., & Rees, M. J. 1972, A&A, 21, 1

Prinja, R. K., Ringwald, F. A., Wade, R. A., & Knigge, C. 2000, MNRAS, 312, 316

Proga, D. 2003, ApJ, 585, 406

Proga, D., & Kallman, T. R. 2002, ApJ, 565, 455

Proga, D., Stone, J. M., & Drew, J. E. 1998, MNRAS, 295, 595

Raghavan, D., McAlister, H. A., Henry, T. J., et al. 2010, ApJS, 190, 1

Raiteri, C. M., Villata, M., Acosta-Pulido, J. A., et al. 2017, Nature, 552, 374

Rajwade, K., Kennedy, M., Breton, R., et al. 2018, The Astronomer's Telegram, 12186, 1

Rappaport, S., Verbunt, F., & Joss, P. C. 1983, ApJ, 275, 713

Reynolds, M. T., Miller, J. M., Ludlam, R. M., & Tetarenko, B. E. 2018, The Astronomer's Telegram, 12220, 1

Ricker, G. R., Winn, J. N., Vanderspek, R., et al. 2015, Journal of Astronomical Telescopes, Instruments, and Systems, 1, 014003

Ringwald, F. A., & Naylor, T. 1998, AJ, 115, 286

Ritter, H. 1976, MNRAS, 175, 279

Ritter, H., Politano, M., Livio, M., & Webbink, R. F. 1991, ApJ, 376, 177

Rodríguez-Gil, P., Gänsicke, B. T., Hagen, H. J., et al. 2007, MNRAS, 377, 1747

Romanova, M. M., Ustyugova, G. V., Koldoba, A. V., Chechetkin, V. M., & Lovelace, R. V. E. 1997, ApJ, 482, 708

Roming, P. W. A., Kennedy, T. E., Mason, K. O., et al. 2005, Space Sci. Rev., 120, 95

Russell, D. M., Fender, R. P., & Jonker, P. G. 2007, MNRAS, 379, 1108

Russell, T. D., Miller-Jones, J. C. A., Sivakoff, G. R., et al. 2016, MNRAS, 460, 3720

Sahman, D. I., Dhillon, V. S., Knigge, C., & Marsh, T. R. 2015, MNRAS, 451, 2863

Sahman, D. I., Dhillon, V. S., Littlefair, S. P., & Hallinan, G. 2018, MNRAS, 477, 4483

Samus, N. N., Pastukhova, E. N., & Durlevich, O. V. 2007, Peremennye Zvezdy, 27, 6

Sánchez-Sierras, J., & Muñoz-Darias, T. 2020, A&A, 640, L3

Sandage, A. R. 1953, AJ, 58, 61

Santamaría, E., Guerrero, M. A., Ramos-Larios, G., et al. 2019, MNRAS, 483, 3773

Scargle, J. D. 1982, ApJ, 263, 835

Scaringi, S., Maccarone, T. J., Kording, E., et al. 2015, Science Advances, 1, e1500686

Scepi, N., Dubus, G., & Lesur, G. 2019, A&A, 626, A116

Scepi, N., Lesur, G., Dubus, G., & Flock, M. 2017, in SF2A-2017: Proceedings of the Annual meeting of the French Society of Astronomy and Astrophysics, ed. C. Reylé, P. Di Matteo, F. Herpin, E. Lagadec, A. Lançon, Z. Meliani, & F. Royer, Di

Schenker, K., & King, A. R. 2002, in Astronomical Society of the Pacific Conference Series, Vol. 261, The Physics of Cataclysmic Variables and Related Objects, ed. B. T. Gänsicke, K. Beuermann, & K. Reinsch, 242

Schenker, K., King, A. R., Kolb, U., Wynn, G. A., & Zhang, Z. 2002, MNRAS, 337, 1105

Schirmer, M. 2013, ApJS, 209, 21

Schlafly, E. F., & Finkbeiner, D. P. 2011, ApJ, 737, 103

Schmidtobreick, L., Rodríguez-Gil, P., & Gänsicke, B. T. 2012, Mem. Soc. Astron. Italiana, 83, 610

Schmidtobreick, L., Shara, M., Tappert, C., Bayo, A., & Ederoclite, A. 2015, MNRAS, 449, 2215

Schreiber, M. R., Zorotovic, M., & Wijnen, T. P. G. 2016, MNRAS, 455, L16

Schwartz, P. R., Waak, J. A., & Smith, H. A. 1983, ApJ, 267, L109

Seaton, M. J. 1978, MNRAS, 185, 5P

Sedov, L. I. 1959, Similarity and Dimensional Methods in Mechanics (NYAP)

Shakura, N. I., & Sunyaev, R. A. 1973, A&A, 500, 33

Shara, M. M., Drissen, L., Martin, T., Alarie, A., & Stephenson, F. R. 2017, MNRAS, 465, 739

Shara, M. M., Mizusawa, T., Wehinger, P., et al. 2012, ApJ, 758, 121

Shara, M. M., Martin, C. D., Seibert, M., et al. 2007, Nature, 446, 159

Shidatsu, M., Done, C., & Ueda, Y. 2016, ApJ, 823, 159

Shields, G. A., McKee, C. F., Lin, D. N. C., & Begelman, M. C. 1986, ApJ, 306, 90

Shrader, C. R., Wagner, R. M., Hjellming, R. M., Han, X. H., & Starrfield, S. G. 1994, ApJ, 434, 698

Shu, F. H. 1982, The Physical Universe (USB)

Simonsen, M. 2011, Journal of the American Association of Variable Star Observers (JAAVSO), 39, 66

Sion, E. M. 1995, ApJ, 438, 876

—. 1999, PASP, 111, 532

Skrutskie, M. F., Cutri, R. M., Stiening, R., et al. 2006, AJ, 131, 1163

Smak, J. 1971, Acta Astron., 21, 15

—. 1981, Acta Astron., 31, 395

Sokoloski, J. L. 2003, JAAVSO, 31, 89

Spencer, R. E. 1979, Nature, 282, 483

Spruit, H. C. 1996, in NATO Advanced Study Institute (ASI) Series C, Vol. 477, Evolutionary Processes in Binary Stars, ed. R. A. M. J. Wijers, M. B. Davies, & C. A. Tout, 249

Steele, I. A., Bates, S. D., Gibson, N., et al. 2008, in Society of Photo-Optical Instrumentation Engineers (SPIE) Conference Series, Vol. 7014, Ground-based and Airborne Instrumentation for Astronomy II, ed. I. S. McLean & M. M. Casali, 70146J

Stephenson, F. R. 1971, Astrophys. Lett., 9, 81

—. 1976, QJRAS, 17, 121

Stephenson, F. R., & Green, D. A. 2009, Journal for the History of Astronomy, 40, 31

Strohmayer, T. E., & Brown, E. F. 2002, ApJ, 566, 1045

Szkody, P., Albright, M., Linnell, A. P., et al. 2013, PASP, 125, 1421

Tasse, C., Hugo, B., Mirmont, M., et al. 2018, A&A, 611, A87

Taylor, G. 1950, Proceedings of the Royal Society of London Series A, 201, 159

Tetarenko, A. J., Freeman, P., Rosolowsky, E. W., Miller-Jones, J. C. A., & Sivakoff, G. R. 2018a, MNRAS, 475, 448

Tetarenko, A. J., Rosolowsky, E. W., Miller-Jones, J. C. A., & Sivakoff, G. R. 2020a, MNRAS, 497, 3504

Tetarenko, A. J., Sivakoff, G. R., Miller-Jones, J. C. A., et al. 2017, MNRAS, 469, 3141

Tetarenko, B. E., Dubus, G., Lasota, J. P., Heinke, C. O., & Sivakoff, G. R. 2018b, MNRAS, 480, 2

Tetarenko, B. E., Dubus, G., Marcel, G., Done, C., & Clavel, M. 2020b, MNRAS, 495, 3666

Tetarenko, B. E., Lasota, J. P., Heinke, C. O., Dubus, G., & Sivakoff, G. R. 2018c, Nature, 554, 69

Thorstensen, J. R., Ringwald, F. A., Wade, R. A., Schmidt, G. D., & Norsworthy, J. E. 1991, AJ, 102, 272

Tokovinin, A., Fischer, D. A., Bonati, M., et al. 2013, PASP, 125, 1336

Townsley, D. M., & Bildsten, L. 2004, ApJ, 600, 390

Tse-Tsung, H. 1957, AZh, 34, 159

Uttley, P., & McHardy, I. M. 2001, MNRAS, 323, L26

van Buren, D., & McCray, R. 1988, ApJ, 329, L93

van den Eijnden, J., Degenaar, N., Russell, T. D., et al. 2020, MNRAS, 496, 4127

van Dokkum, P. G. 2001, PASP, 113, 1420

van Paradijs, J. 1978, Nature, 274, 650

—. 1983, A&A, 125, L16

—. 1996, ApJ, 464, L139

van Paradijs, J., & McClintock, J. E. 1994, A&A, 290, 133

VanderPlas, J. T. 2018, ApJS, 236, 16

Vasilopoulos, G., Bailyn, C., & Milburn, J. 2018, The Astronomer's Telegram, 12164, 1

Verbunt, F., & Zwaan, C. 1981, A&A, 100, L7

Vernet, J., Dekker, H., D'Odorico, S., et al. 2011, A&A, 536, A105

Vogt, N., Hoffmann, S. M., & Tappert, C. 2019, Astronomische Nachrichten, 340, 752

Wade, R. A., & Hubeny, I. 1998, ApJ, 509, 350

Walton, D. J., Miller, J. M., Harrison, F. A., et al. 2013, ApJ, 773, L9

Wang, B., & Han, Z. 2012, New A Rev., 56, 122

Wang, Y. M. 1987, A&A, 183, 257

Wareing, C. J., Zijlstra, A. A., & O'Brien, T. J. 2007, MNRAS, 382, 1233

Warner, B. 1995, Cataclysmic variable stars (Camb. Astrophys. Ser.)

Waters, T., Proga, D., & Dannen, R. 2021, ApJ, 914, 62

Weaver, R., McCray, R., Castor, J., Shapiro, P., & Moore, R. 1977, ApJ, 218, 377

Whitehurst, R. 1988, MNRAS, 232, 35

Whitehurst, R., & King, A. 1991, MNRAS, 249, 25

Wijnands, R., Degenaar, N., & Page, D. 2017, Journal of Astrophysics and Astronomy, 38, 49

Williams, R. E. 1994, ApJ, 426, 279

Wolf, C., Onken, C. A., Luvaul, L. C., et al. 2018, PASA, 35, e010

Wolf, W. M., Bildsten, L., Brooks, J., & Paxton, B. 2013, ApJ, 777, 136

Wood, J., Horne, K., Berriman, G., et al. 1986, MNRAS, 219, 629

Wood, M. A., & Burke, C. J. 2007, ApJ, 661, 1042

Wood, M. A., Thomas, D. M., & Simpson, J. C. 2009, MNRAS, 398, 2110

Woodgate, B. E., Kimble, R. A., Bowers, C. W., et al. 1998, PASP, 110, 1183

Woods, D. T., Klein, R. I., Castor, J. I., McKee, C. F., & Bell, J. B. 1996, ApJ, 461, 767

Wright, N. J., & Drake, J. J. 2016, Nature, 535, 526

Yang, H.-J., Park, M.-G., Cho, S.-H., & Park, C. 2005, A&A, 435, 207

Yaron, O., Prialnik, D., Shara, M. M., & Kovetz, A. 2005, ApJ, 623, 398

Zechmeister, M., & Kürster, M. 2009, A&A, 496, 577

Zhu, H., Tian, W., Li, A., & Zhang, M. 2017, MNRAS, 471, 3494

Zorotovic, M., Schreiber, M. R., & Gänsicke, B. T. 2011, A&A, 536, A42

Zwart, J. T. L., Barker, R. W., Biddulph, P., et al. 2008, MNRAS, 391, 1545